Delft University of Technology

Master Thesis Space
AE5810

How Much Ice Could an Icy Io Have Lost Through Tidal Heating?

Author:
Sean Finck
Student number 1323474

Supervisors:
dr. Wouter van der Wal
dr. Marc Rovira Navarro

May 31, 2022

Contents

List of Figures

Executive Summary

The four Galilean satellites are Io, Europa, Ganymede and Callisto. They are thought to have formed from Jupiter's protosatellite disk at roughly the same time [Canup and Ward, 2009]. One of the differences between these satellites is that the average density decreases with distance from Jupiter which is due to the corresponding increase in ice mass fraction. The estimated ice mass fractions are 0, 8, 45 and 56 % for Io, Europa, Ganymede and Callisto respectively. Since their formation Io, Europa and Ganymede have entered a 4-2-1 resonance which is called the Laplace resonance. It is estimated that this resonance has been present since their formation [Peale and Lee, 2002]. Because of this Io's orbit has remained eccentric which in turn causes Io to experience tidal dissipation. Tidal heating has the possibility to melt part of an icy Io's ice shell and form a subsurface ocean [de Kleer et al., 2019]. Moons with subsurface oceans are very interesting to the scientific community because they are prime candidates for the existence of extraterrestrial life [Spencer et al., 2009]. By investigating the ice loss of such moons one can learn much about them and their evolution. There are several possible reasons why Io is the only Galilean satellite without ice. This work will assume that Io once was icy but that it lost its ice through geysers. This leads us to the main research question: How much ice could an icy Io have lost through tidal heating?

In order to answer the main research question a model of an icy Io was built. In this model the interior structure of icy Io is assumed to be fully differentiated from the start and consists of a rocky part with a H_2O-layer on top. The rocky part is identical to the present day Io and is held constant except for the mantle temperature, melt fraction, viscosity and shear modulus. The internal structure of the H_2O-layer is also able to change throughout the simulation. A stagnant lid regime is assumed for the ice shell. Within this regime the ice shell consists of a conductive lid and a convective sublayer if convection is the dominant mode of heat transport. If the dominant mode of heat transport is conduction then the ice shell is reduced to a single conductive layer. If the total thickness of the ice shell is less than the thickness of the H_2O-layer then the remaining part is a subsurface ocean. The assumption of an equilibrium state for icy Io is the first key assumption of this work. Starting from an initial estimate of the ice shell thickness an iterative process is used to determine an interior structure that provides an equal heat flow through each sublayer, as required by the condition of equilibrium. Mantle properties such as its temperature and viscosity are calculated such that the silicate mantle has the same heat flow as the icy shell resulting in a temporary solution for the interior structure.

The source of tidal dissipation is the periodic deformation that Io experiences due to gradients within Jupiter's gravitational field. The amount of tidal dissipation that occurs depends on the eccentricity e, the mean motion n, the radius of the moon R and the interior structure through the imaginary part of the tidal Love number k_2. In this work the eccentricity is kept constant but the mean motion will vary due to the tidal migration of Io. The magnitude of the tidal dissipation is calculated using the propagator matrix method by Jara-Orué and Vermeersen [2011] and Sabadini et al. [2016] and the method created by Beuthe [2013] which uses weight functions to determine the dissipated power in a differentiated moon. The end result is the total amount of dissipated heat within icy Io. As required by the equilibrium conditions the heat flow from the dissipated heat must be equal to the heat flow through each layer of the temporary solution. If they are not equal a new temporary solution is sought by using a new value of the initial estimate for the thickness of the ice shell. This is the second iterative process and it will run until an interior structure is found where the heat flow through each layer is equal to the heat flow due to tidal dissipation. This is then called the equilibrium solution.

The ice loss mechanism considered in this work is geysers. The second key assumption of this work is that the geyser activity on Enceladus is a typical example for icy moons and can therefore be copied and

upscaled to icy Io. This assumption is made because Enceladus is the only body in the Solar System that has geysers which have been studied extensively. Therefore copying and upscaling its geyser system could serve as a good initial model of the geyser system of icy Io. The geysers of the model of icy Io are based on the model by Schmidt et al. [2008] who proposed that the geysers of Enceladus are fed through cracks within its ice shell that run from the surface to its subsurface ocean. This ocean then acts as the reservoir for the erupted material. Water vapor molecules and icy grains are accelerated as they rise through these cracks and erupt at the surface. Three conditions for the existence of geysers are applied in this work. The first is that there exists an ice shell, the second that there exists a subsurface ocean underneath the ice shell and the third that cracks run from the surface through the ice shell to the subsurface ocean. The third condition depends on the magnitude of the surface stress. At a number of points, the surface stress is calculated and if larger than the failure threshold of 100 kPa crack instigation is assumed to be present at the corresponding points. For each of these points it is determined if the surface stress is large enough to propagate the crack downwards through the ice shell. If the crack depth is larger than the thickness of the ice shell it is assumed that geyser activity is possible at that point. The fraction of points where geyser activity is possible is called the eruptive area. Surface stresses on both Enceladus and icy Io are similar in magnitude indicating that icy Io will also have a fractured ice shell, further advocating for the applicability of Enceladus-like geysers activity to icy Io. The eruption rate of icy Io can then be directly upscaled from the eruption rate per unit area of Enceladus' South Polar Terrain. The escape rate is determined by applying a velocity distribution to the erupted material and integrating to determine how much material is erupted at velocities larger than the escape velocity. The escaped material is considered lost while the rest falls back to the surface.

In order to answer the main research question three different cases were created. With the maximum case all parameters were set as high as possible to determine what the maximum amount of ice loss could be. The two average cases used parameters values that were averages of literature estimates in order to obtain more realistic results. The difference between the high-end and low-end average cases is the applied velocity distribution of the erupted particles. A simulation of the thermal-orbital evolution of each case was performed. Per time step the escaped material is removed from the H_2O-layer after which the whole process restarts. This continues until all water has been removed, geyser activity is halted before the H_2O-layer has been depleted or an equilibrium solution is no longer found.

The results of these simulations show that the maximum case is able to remove a H_2O-layer with a thickness of 210 km, which is larger than that of present-day Europa which is estimated to be about 144 km [Hussmann and Spohn, 2004]. The high- and low-end average cases were able to remove H_2O-layer with a thickness of about 52 and 13 km respectively. One of the main findings of the simulations is that the thickness of the ice shell depends primarily on the semi-major axis and the corresponding magnitude of tidal dissipation. The three cases started the simulation at relatively similar positions resulting in similar ice shell thicknesses, even though the outer radii were quite different. Due to the different migration rates of each case their semi-major axes started to differ during their evolution. It was clear that at these points in time, when their instantaneous positions were no longer similar, that their ice shell thicknesses also started to differ. Another main finding is that the eruptive area declined with distance from Jupiter but the rate of decrease was accelerated once the eruptive area dropped below 80%. This was not noticed in the low-end average case as in that case the eruptive area never dropped below this value. What is striking is that this threshold of 80% was reached when the maximum case and the high-end average cases had roughly the same semi-major axis indicating that the distance from Jupiter is again the main driver behind the ice loss rate through geysers. Adding these conclusions together it is quite possible that geysers as an ice loss mechanism or at least the presence of geysers is limited to a certain distance from the host planet. The minimum distance is the Roche limit for that particular satellite and host planet and the maximum distance is that at which the surface stresses fall below the failure threshold of 100 kPa. Of course the results are based on the assumptions that were made during this work. Therefore some changes are recommended to improve on these results. By making these improvements it will be possible to give a better answer to the research question(s) and to test some of the findings which are presented in this work. The simplest way to improve the results is to decrease the length of the time-step. Further improvements can be made by including a change in eccentricity and possibly also the influence of Europa on the thermal-orbital evolution of icy Io. Lastly one can improve the results by also considering other possible ice loss mechanisms acting in tandem with geysers. This however requires a substantial addition

to the model presented in this work.

Chapter 1

Introduction

Io, Europa, Ganymede and Callisto are four of Jupiter's regular satellites. Here the term regular refers to their origin. It is believed that these satellites formed in Jupiter's protosatellite disk at approximately the same time and have several similarities, namely similar masses, low eccentricity and that they are approximately coplanar [Canup and Ward, 2009]. When comparing the Galilean satellites it can be seen that the density of the moons becomes lower as their distance from Jupiter increases. This so-called density gradient is a direct result of the increasing ice mass fraction with increasing distance (see Table 2.1). The ice mass fractions are 0, 8, 45 and 56 % for Io, Europa, Ganymede and Callisto respectively [Canup and Ward, 2009]. Because of the different ice mass fractions each moon has a different interior structure. Io consists of a rocky core and silicate mantle while Europa and Ganymede have an added H_2O-layer overlying their silicate mantles [Schubert et al., 2004]. Europa's H_2O-layer is about 141 km thick and consists of an ice-I shell and a subsurface ocean [Hussmann and Spohn, 2004] whereas Ganymede's is about 914 km thick and consists of an outer ice-I shell with a subsurface ocean below and a second, high-pressure ice shell underneath the ocean [Bland et al., 2009]. Note that the thicknesses of the H_2O-layers mentioned above and the thicknesses of the other interior layers such as the core and mantle are possibly different depending on the referenced literature. Please see Section 2.2 for more information. Figure 2.1 shows a schematic version of the interior structure of Europa and Ganymede's H_2O-layers. Io, Europa and Ganymede are considered fully differentiated, meaning that they consist of distinctive, separate layers. It is thought that Callisto on the other hand is not yet fully differentiated and as such does not have distinctive layers [Schubert et al., 2004]. Io is the only Galilean moon without any ice which can be due to two reasons: either Io never had any ice or the ice that Io had was lost over the course of its lifetime. Studies have been done that support both scenarios, such as that of Canup and Ward [2002] for the scenario where Io never contained any ice and that of Bierson and Nimmo [2020] for the scenario where Io once contained ice but subsequently lost it over its lifetime. In this work the assumption will be made that Io initially contained some ice and that this was lost due to some sort of ice loss mechanism. Tidal heating on icy moons is able to melt part of their ice to form subsurface oceans [Beuthe, 2013]. Io experiences an enormous amount of tidal heating through its interaction with Jupiter's gravitational field [Fischer and Spohn, 1990], [de Kleer et al., 2019]. It is therefore possible that, if Io once contained ice, it would have a subsurface ocean maintained through this tidal heating. Icy moons with subsurface oceans are of particular interest to the scientific community as they are good candidates for the presence of extraterrestrial life [Spencer et al., 2009]. Investigating ice loss on icy moons could give some insight in to the longevity of subsurface oceans of such moons and their evolution.

Starting from the assumption of an icy Io it follows that its ice could have been lost through some sort of ice loss mechanism. Possible ice loss mechanisms may be grouped by the time at which they could have affected icy Io, either during or after formation. The first possible mechanism that could have occurred during formation is imperfect accretion between two planetesimals. With imperfect accretion some mass may be lost through physical erosion, where some fragments are broken off through impact and lost to the accreting moon or through vapor erosion, where ice is vaporized during impact and also lost. As an ice loss mechanism imperfect accretion is most efficient for fully differentiated bodies as all of their ice is located in an exterior shell. Dwyer et al. [2013] investigated imperfect accretion and concluded that even if the initial ice mass fractions of the Galilean satellites was radially dependent, with Io having

the least amount of initial mass, physical and vapor erosion could not result in the ice mass fractions of the Galilean satellites as observed today. A second possible ice loss mechanism during formation is hydrodynamic escape. Hydrodynamic escape occurs around smaller bodies with a low gravitational acceleration [Bierson and Nimmo, 2020] and an atmosphere. Differences between the background pressure and the surface pressure cause vertical winds to exist within the atmosphere. These winds accelerate molecules as they move upwards from the surface and could reach a points where molecules move fast enough to escape. Using a gas-starved circumplanetary disk as proposed by Canup and Ward [2002] hydrodynamic escape could cause enough ice loss to obtain the observed gradient density if formation timescales are sufficiently long (more than $3{\cdot}10^5$ years) [Bierson and Nimmo, 2020]. Two caveats of the study by Bierson and Nimmo [2020] is that they assume that the conditions of the disk in which the satellites form are static and that they do not include satellite migration. Both these assumptions have an impact on the local conditions and will thus also have an impact on the rate of hydrodynamic escape. A third possible ice loss mechanism is ice loss through high-velocity impacts which occurred after formation. Such impacts could remove ice from a moon through vapor or physical erosion as described above. Nimmo and Korycansky [2012] investigated the possibility of the Late Heavy Bombardment being the reason as to why Io is no longer icy. Their results show that Io's lack of ice could be caused by such a mechanism. However the same simulation also removed all of Mima's and Miranda's ice whereas their present ice mass fractions are 82% and 77% respectively [Hussmann et al., 2010]. These contradictory results shed some doubt on the validity of high-velocity impacts such as the LHB causing Io's ice loss.

Because of the mentioned caveats to the three methods described above this work will consider another ice loss mechanism as the cause for Io's lack of ice: tidal heating. Icy moons with sufficient tidally generated heat are able to sustain a subsurface global ocean for extended periods of time. Above such an ocean would lie an icy shell which could fracture due to eccentricity driven tidal stresses leading to the possible presence of geysers. Just like the geysers of Enceladus they could be able to remove ice from Io. As indicated by the work of Canup and Ward [2009] and Dwyer et al. [2013] tidal heating provides a lot of energy with which ice can be removed. The previously mentioned works approach this problem from an energy point of view and only mention the efficiency of a possible ice loss mechanism. They do not discuss actual ice loss mechanisms or how these mechanisms are able to remove ice. Bierson and Steinbrügge [2021] improved on those works by looking at several possible ice loss mechanisms and how efficiently they would be able to remove ice from a moon. The authors started from the premise of an icy Io which had an ice mass fraction of 34%. They determined that the latent heat of vaporization for that amount of ice and the energy required to bring it to Jupiter's Hill sphere is about $1{\cdot}10^{30}$ J. Assuming that the current tidal heating rate for Io has been constant over the last 4.5 Gyr the amount of energy available for ice loss is about $3{\cdot}10^{31}$ J. Dividing the required energy by the available energy gives an indication of how efficient the ice loss mechanism should be, about 3%. Using these simple assumptions the authors then looked in to several ice loss mechanisms and determined if they would have been efficient enough to remove the ice. They conclude that direct mass loss through geysers or Jeans escape from a geyser-sustained atmosphere would not have been efficient enough to remove all of the ice.

One caveat of their work of Bierson and Steinbrügge [2021] is that they assume a constant tidal heating rate whereas it has been shown by thermal-orbital evolution models such as that of Hussmann and Spohn [2004] that the eccentricity and tidal heating rate vary over Io's lifetime. A second caveat is of their work is that the authors only considered an icy Io with a high ice mass fraction. The reason for this being that this would result in the same average density for each of the Galilean satellites. According to Ronnet et al. [2017] it is possible that the Galilean satellites formed within regions in which solids had a different ice mass fraction depending on the distance from Jupiter. Regions closer to Jupiter contained solids with much lower ice mass fractions than regions that were further away. A result of this would be that Io, being the close to Jupiter, would have been primarily formed from dehydrated solids making it difficult to obtain such a high ice mass fraction as proposed by Bierson and Steinbrügge [2021]. The third caveat is that the authors only consider slow-moving icy grains when determining the mass loss rate through geysers whereas most of the erupted material will be in the form of vapor molecules which erupt at much higher velocities and are thus more likely to escape from icy Io.

The main research question in this work is the following:

How much ice could an icy Io have lost through tidal heating?

This aim of this work is to answer the above mentioned research question by creating a detailed model of an icy Io and its ice loss through geysers. This will be done by combining different elements. By doing this those caveats of the work by Bierson and Steinbrügge [2021] that are mentioned above can be addressed. In order to do this several sub-questions have been determined and are listed in the following paragraphs.

(1) What would the interior structure of an icy Io look like at the end of its formation? The geysers of this work are modeled after the work of Schmidt et al. [2008] in which the authors models the geysers of Enceladus. In that model the geysers require a liquid reservoir therefore it is important to know if an icy Io would have a liquid reservoir and if this is local or global in the form of a subsurface ocean. A first comparison will be made with the other Galilean satellites, especially Europa and Ganymede as they both have a H_2O-layer with a subsurface ocean. The differences and similarities between the H_2O-layers of Europa and Ganymede might offer some insight in to the possible structure of an icy Io's H_2O-layer. If an ocean is present would icy Io's H_2O-layer then be more similar to Europa's or to Ganymede's or perhaps a different structure altogether? The second improvement will be obtained by tackling the second caveat. Lower ice mass fractions than the 34% that was assumed by Bierson and Steinbrügge [2021] are entirely possible due to the type-I migration that the Galilean satellites experienced during their formation [Canup and Ward, 2002]. If Io started to accrete outside of the snowline, where temperatures were low enough to allow for the presence of ice [Lunine, 2006], it would explain the presence of ice on Io. During formation type-I migration caused the accreting Galilean satellites to migrate inwards. If Io crossed the snow line relatively early in its formation further accretion of ice would have stopped, resulting in a low ice mass fraction. A different explanation could be that Io accreted more ice but that some of this ice was already removed due to processes which occurred during accretion such as imperfect accretion [Dwyer et al., 2013] or hydrodynamic escape [Bierson and Nimmo, 2020]. Both the type-I satellite migration and ice loss mechanisms during formation could account for a low ice mass fraction on Io at the end of its formation. Because Bierson and Steinbrügge [2021] assumed such a large ice mass fraction more energy is required to remove this ice. This in turn demanded an ice loss mechanism with an improbably high efficiency. A lower initial ice mass fraction would allow for the possibility of ice loss mechanisms with a lower efficiency.

(2) How much tidal dissipation would occur in an icy Io over time? This can be calculated with the following Equation[Segatz et al., 1988].

$$\dot{E} = -\frac{21}{2}\frac{R^5 n^5 e^2}{G} Im\left(k_2\right) \tag{1.1}$$

From this Equation it is clear that there exists a link between the amount of tidal dissipation $\dot{E}$ on the one hand and the interior structure (through the imaginary part of the Love number k_2) and the orbital parameters (through e and n) on the other hand. The amount of tidal heating is proportional to the fifth power of the mean motion n. Since its formation Io has migrated outwards significantly [Lainey et al., 2009] indicating that tidal heating must have been higher in the past. Therefore a constant tidal heating rate as assumed by Bierson and Steinbrügge [2021] will result in an underestimation of the amount of ice that could be lost. Additionally the tidal heating is also affected by the internal structure of the satellite through the imaginary part of the Love number k_2. This work will incorporate the tidal migration and the ongoing change of an icy Io's interior by continuously removing any ice that is lost through its geyser activity. By doing this a more accurate estimate of the mass loss can be obtained. What will not be included is the change in eccentricity e as this would be beyond the scope of this work.

(3) How can an icy moon lose water through tidal heating? As mentioned above this work will only consider ice loss through geyser activity driven by tidal heating. The key question regarding ice loss is how much geyser activity there is and how much erupted mass is able to escape from icy Io. To answer this questions a closer look will be taken at the geyser activity of Enceladus as that has been studied extensively. The applicability of Enceladus' geysers to an icy Io will be assessed and then parameterized and upscaled to icy Io.

By answering the above sub-questions a detailed model of an icy Io and its ice loss through geysers can be created. In this work two major assumptions are made: The first assumption is that icy Io is

in an equilibrium state, meaning that it experiences little change in semi-major-axis, tidal dissipation and internal structure amongst others. This assumption is made because models Io's and Europa's thermal-orbital evolution show that Io has been in such an equilibrium state for large periods of its history [Hussmann and Spohn, 2004]. Furthermore it offers an elegant way of determining the interior structure of icy Io's H_2O-layer. The second major assumption is that icy Io's geysers are similar to those of Enceladus and can thus be modeled after them. This assumption is made because there is no exact physical model of geyser activity on an icy moon but the geyser activity on Enceladus has been studied extensively. Simulations of the orbital evolution of three different cases will be performed in this work: a maximum case, a high-end average case and a low-end average case. With the maximum case maximum values will be chosen for each simulated variable in order to determine how much ice could have been removed if all the relevant parameters were favorable for ice loss. For the two average cases the chosen values for each parameter will be averaged in order to obtain more probable results. The difference between the two average cases is that with the high-end average case the erupted material will have a Lorentzian velocity distribution and with the low-end average case they will have an exponential distribution.

This work is divided in two parts with three chapters each. The first part will describe the whole model, starting with the interior structure in Chapter 2. The source and magnitude of the tidal dissipation are discussed in Chapter 3 together with the tidal migration and the interior structure of icy Io that complies with the assumed equilibrium state of icy Io. Chapter 4 first investigates the different ice loss mechanisms in more detail. Next conditions under which geysers may exist are established. Afterwards the geysers of Enceladus are investigated and parameterized. Finally the escape rate for an icy Io is discussed. The second part of this work describes the simulations and discusses the results of those simulations. Chapter 5 starts off by describing the workflow of the code that was written for the simulations. Next some simulation-specific design choices and the influence of some key parameters on the accuracy and computational time are discussed. The chapter ends with an overview of the different simulated variables and a summary of the three cases. The results and a discussion of them can be found in Chapter 6. Here also a critical reflection on the approach and assumptions of this work is performed. Lastly Chapter 7 lists the conclusions of this work and some recommendations for future research.

Part I

Interior Structure, Tidal Heating and Geysers of an Icy Io

Chapter 2

Interior Structure of an Icy Io

2.1 Introduction

Present-day Io is a fully differentiated rocky moon with no ice [Schubert et al., 2004]. The starting assumption of this work is that after formation Io did contain some ice but lost it all through some ice loss mechanism. This chapter will investigate what the interior structure of an icy Io could look like. As noted in Chapter 1, the Galilean satellites are thought to have been formed simultaneously from Jupiter's protosatellite disk resulting in them having several similarities [Canup and Ward, 2009]. This chapter will therefore start of by looking at the different Galilean satellites, their similarities and their differences. Both Europa and Ganymede have a H_2O-layer on top of their silicate mantles but the interior structure of each H_2O-layer is very different. Depending on the amount of water on icy Io the interior structure of its H_2O-layer might be similar to that of Europa or it might be more similar to that of Ganymede. The applicability of each case to an icy Io will be addressed as well. The general structure of the Galilean satellites is given in Section 2.2 and a more detailed investigation of the possible interior structure of icy Io's H_2O-layer is performed in Section 2.3. Several topics include the different possible sub-layers, how thick they are and what the corresponding temperature profile across the H_2O-layer is. Next in Section 2.4 a closer look will be taken at the silicate mantle of an icy Io, more specifically the different mantle properties will be investigated and how they can be determined. This chapter will conclude with a complete overview of the interior structure of an icy Io and can be found in Section 2.5. The complete interior structure, including the properties of each sub-layer, are required in order to calculate the amount of tidal heating which is discussed in detail in Chapter 3.

2.2 Present-day Structure of the Galilean Satellites

Three of the four Galilean satellites are thought to be fully differentiated, meaning that they have individually separate layers. For Io this means a metallic core and a silicate mantle and for Europa and Ganymede the same metal core and silicate mantle are present but they also have an overlying H_2O-layer [Schubert et al., 2004]. In contrast Callisto is thought not to be differentiated. It has no metallic core and rock and ice are mixed throughout its interior [Schubert et al., 2004]. Estimates of the internal structure of the Galilean satellites is based primarily on gravitational data. The average density of each satellite can be determined from relatively far-away flybys and is shown in Table 2.1 together with some other general parameters of each Galilean satellite. The satellites are listed according to distance from Jupiter with Io being the closest and Callisto the furthest. From Table 2.1 the density gradient can be clearly seen with a decrease in average density with increasing distance from Jupiter. This goes hand in hand with the increase in ice mass fraction with increasing distance from Jupiter.

Gravitational data from flybys at distance does not provide an exact interior structure [Schubert et al., 2004]. In order to obtain more constraints on the interior structure more close flybys are required. With closer flybys it is possible to estimate the moment of inertia of a satellite which, together with the radius and average density, offers the possibility to determine several possible interior structures which satisfy these three parameters. As an example Schubert et al. [2004] suggest that Ganymede's may have a Fe

Table 2.1: Properties of the Galilean satellites [De Pater and Lissauer, 2015] and [Canup and Ward, 2009]

Satellite	Inclination [deg]	Eccentricity	Mass [$\cdot 10^{20}$ kg]	Radius [km]	Average Density [kg m^{-3}]	Ice mass fraction [%]
Io	0.04	0.0041	893.3	1821	3530	-
Europa	0.470	0.0101	479.7	1565	3020	8
Ganymede	0.195	0.0015	1482	2634	1940	45
Callisto	0.28	0.007	1076	2403	1850	56

core (with a density of 8000 kg m^{-3}) or a Fe-FeS core (with a density of 5150 kg m^{-3}). Thus depending on the composition of the core its radius will differ in order to have the proper moment of inertia. Because of this the authors indicate that the core radius of Ganymede may lie between 650 and 900 km depending on the chosen core composition. Therefore slightly different interior structures can be found throughout the literature. Bland et al. [2009] for example use a model of Ganymede with a core radius of 700 km and a density of 6500 kg m^{-3}, which lies between the limits set by Schubert et al. [2004].

Even though different interior structures are possible a striking similarity between the three interior Galilean satellites Io, Europa and Ganymede can be found by comparing their rocky parts. The rocky part of each satellite consists of the core and silicate mantle. Table 2.2 shows that the radii of the cores and silicate mantles, masses and average densities of the rocky parts are quite similar for the three interior Galilean satellites. As Europa, Ganymede and icy Io are fully differentiated (which is assumed here for the case of an icy Io) their H_2O-layers lie directly over their rocky parts. Therefore when considering the possible structure of icy Io's H_2O-layer it can be directly compared to those of Europa and Ganymede.

Table 2.2: Properties of the rocky parts of the three interior Galilean satellites [Hussmann and Spohn, 2004], [Bland et al., 2009] and [Schubert et al., 2004]

Satellite	Core radius [km]	Silicate mantle radius [km]	Thickness of H_2O-layer [km]	Mass [$\cdot 10^{20}$kg]	Average density [kg m^{-3}]
Io	650 - 950	1821	/	893.3	3530
Europa	203 - 704	1395 - 1485	80 - 170	440.2	3662
Ganymede	650 - 900	1731	900	749.4	3515

2.3 Interior Structure of the H_2O-layer

In this chapter the interior structure of icy Io's H_2O-layer will be discussed. First the different possibilities will be discussed in Section 2.3.1 with the Galilean satellites Europa and Ganymede as examples. For the icy shell of a moon often a stagnant lid regime is applied. Such a regime defines the sub-layers and dominant modes of heat transport within an icy shell and is discussed in Section 2.3.2. Next the temperature profile within a H_2O-layer is given in Section 2.3.3 and lastly the methodology used in this work to determine the actual internal structure of the H_2O-layer can be found in Section 2.3.4.

2.3.1 Possible Interior Structures

As mentioned above it is possible to compare the H_2O-layer of icy Io to that of Europa and Ganymede. The thicknesses of their H_2O-layers are 140 km [Hussmann and Spohn, 2004] and 914 km [Bland et al., 2009] respectively. Depending on the amount of water that is present on an icy Io it is possibly that the structure of its H_2O-layer could be similar to that of Europa. In the work of Hussmann and Spohn [2004] this layer consists of a subsurface water ocean and a spherical ice-I shell. An alternative possible

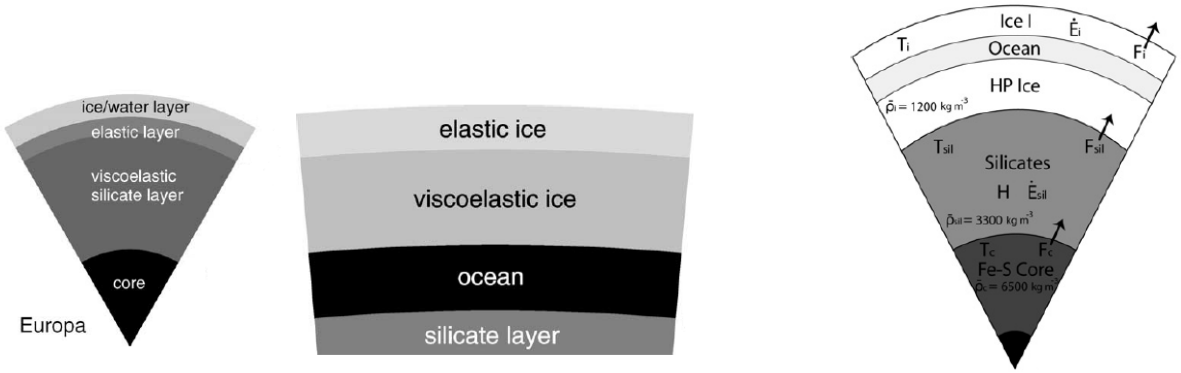

(a) Interior of Europa [Hussmann and Spohn, 2004]

(b) Interior of Ganymede [Bland et al., 2009]

Figure 2.1: Possible interior structures of Europa's and Ganymede's H_2O-layers. As their rocky parts are relatively similar the structure of their respective H_2O-layers will depend mostly on the amount of water they contain. Thin H_2O-layers will be more similar to that of Europa (a) and thicker H_2O-layer will be more similar to that of Ganymede (b).

structure could be similar to that of Ganymede as given by Bland et al. [2009]. The authors propose an ice-I spherical shell at the surface and a subsurface ocean beneath it, similar to the model of Europa mentioned above. In addition there is a second spherical ice shell beneath the ocean which consists of high pressure ices. Both models can be seen in Figures 2.1a and 2.1b respectively.

Whether only type-I ice or other high pressure ices are also present depends on the local temperature and pressure as can be seen in the phase diagram for different types of ice which is shown in Figure 2.2. Bland et al. [2009] determined the internal structure of Ganymede's H_2O-layer which can also be seen in Figure 2.2. The temperature profiles of the two different cases show at what depth the H_2O-layer transforms from ice-I shell to liquid water and then from liquid water to high-pressure ice. The focus here will be on the dotted line as that case results in high-pressure ices existing at higher depths. This will narrow the range of cases where only type-I ice is present. It is clear that the outermost ice-I shell is relatively thin at about 25 km. The pressure and temperature of the ocean increase with increasing depth until high-pressure ice is found just before a depth of 600 km. In their work the authors assumed a H_2O-layer of pure water while in reality it would be somewhat saline. This however does not influence their results significantly [Bland et al., 2009] and the same assumption will be made here. The effect of an increase in salinity is that it will lower the melting temperature requiring less heating to maintain a subsurface ocean [Spohn and Schubert, 2003]. The question now is how applicable the results given in Figure 2.2 are to an icy Io? Equation A.14 shows that the pressure at any given point depends on the local gravitational acceleration, the density of the overlying material and the depth. Similarly to Bland et al. [2009], this work also assumes a H_2O-layer that consists of pure ice thus the density of the overlying material will be equal. The gravitational acceleration at a certain point depends on the sphere that lies below. The rocky part of an icy Io has a mass of $893.3 \cdot 10^{20}$ kg and a radius of 1821 km while the mass and radius of the rocky part of Ganymede are about $750 \cdot 10^{20}$ kg and 1720 km respectively (see Table 2.2). The mass and radii of the rocky components are thus quite similar which causes the gravitational acceleration at the ocean-mantle boundaries to be similar as well, 1.7974 m s^{-2} for icy Io and 1.6920 m s^{-2} for Ganymede. Therefore one can conclude that the results found by Bland et al. [2009] can be applied to the case of an icy Io. In that case it would require an H_2O-layer of at least 600 km for the presence of high pressure ices. Such an H_2O-layer is about 45 wt% of a rocky Io, which is much higher than the cases that are considered in this work (see Table 5.1), indicating that only type-I ice will be present within the three simulated cases.

As the thickness of the individual sub-layers of the H_2O-layers is as yet unknown and that the density will increase with increasing pressure it is difficult to determine the exact density profile within of

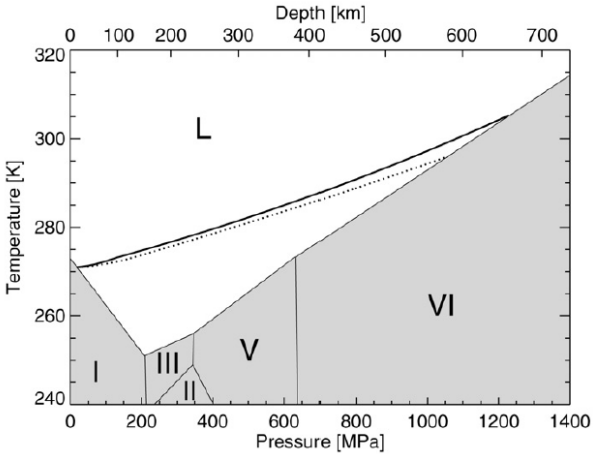

Figure 2.2: Phase diagram for water and ice together with the depth of Ganymede's H_2O-layer [Bland et al., 2009]. The solid and dotted lines represent two different possible temperature profiles with the difference between them being how the thermal expansivity varies with pressure. The presence of high-pressure ices depends on the temperature and pressure which in turn depend on the depth. For the case of Ganymede specifically high-pressure ices will only be present below a depth of 600 km.

Table 2.3: Parameters for several types of ice [Sohl et al., 2002].

Ice type	Density [kg m^{-3}]
Ice I	937
Ice III	1166
Ice V	1267
Ice VI	1360
Water	1000

H_2O-layer. Table 2.3 shows that the difference in density between the types of ice can be up to 45%, which is quite large. For simplicity's sake most studies use a constant density over the whole layer. Bierson and Steinbrügge [2021], Spohn and Schubert [2003], Tobie et al. [2005] and Hussmann and Spohn [2004] use a value of 1000 kg m^{-3} for their models of Europa whereas Schubert et al. [2004] and Sohl et al. [2002] use a value of 1050 kg m^{-3}. Sohl et al. [2002] note that they used the higher value to account for possible higher density ice phases at the bottom of the ice shell. Figure 2.3 shows the thickness of the H_2O-layer for different densities. For this example the mass of the H_2O-layer was set at 10 wt% of Io's present-day mass. As can be seen the difference between the case where the entire H_2O layer consists of ice-I and the case where a value of 1050 kg m^{-3} is used is about 20 km. This shows that the choice of density (between the suggested values) may have a large impact on further calculations. Here a constant density of 1000 kg m^{-3} is chosen. This is higher than the value for ice I as to compensate for the (expected) presence of a subsurface ocean and the increase in density with pressure (and thus depth). Figure 6.2 depicts the evolution of the H_2O-layers for each case during the simulations. It shows that the H_2O-layer consists mostly of water until the very end of the simulation, indicating that adopting the density of water for the whole H_2O-layer was an acceptable choice.

In conclusion the general internal structure of icy Io is similar to that of Europa and Ganymede. Similar in the sense that all three have relatively similar rocky parts (core and silicate mantle) with a H_2O-layer added on top. The main difference between Europa and Ganymede is the thickness of this layer, with that of Europa being about 140 km [Hussmann and Spohn, 2004] and that of Ganymede about 914 km [Bland et al., 2009]. This results in a different internal structure where the H_2O-layer of Europa consisting of a subsurface ocean with a type-I ice shell on top and that of Ganymede consisting of a high-pressure icy shell, a subsurface ocean on top of that and a second icy shell, this time consisting of type-I ice, on top of the ocean. For an icy Io the H_2O-layer would need to have a mass of at least 45 wt%, which would result in a thickness of 600 km, in order to contain high-pressure ices. As the three

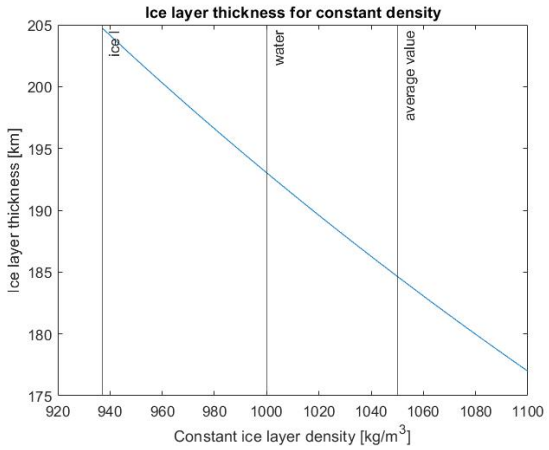

Figure 2.3: The thickness of a H_2O-layer with a fixed amount of water depends on its density. Assuming a constant density across the entire H_2O-layer equal to that of ice-I results in a 20 km thicker H_2O-layer than using an average value of 1050 kg m^{-3} as used by Sohl et al. [2002].

simulated cases have much smaller H_2O-layers than that (see Table 5.1) the internal structure of icy Io's H_2O-layer is expected to be quite similar to that of Europa.

2.3.2 Stagnant Lid Regime

This section will describe what is called the stagnant lid regime. This is an internal regime which is often used when modeling the thermal-orbital evolution of a satellite (see for example Steinke et al. [2020] and Rovira-Navarro et al. [2021]). A stagnant lid regime can be present in both silicate mantles as in icy shells [Hussmann and Spohn, 2004]. Within this regime one can differentiate between two viscoelastic layers: a low viscosity, well-mixed sub-layer and a cold, high-viscosity lid on top of the sub-layer. Within the sub-layer the main method of heat transport is convection whereas that in the elastic lid is conduction. Therefore these two layers are often referred to as the convective and conductive layer respectively. A schematic representation of the stagnant lid regime can be seen in Figure 2.7.

Grasset and Parmentier [1998] performed numerical studies on the convection in a volumetrically heated layer of which the viscosity is strongly temperature-dependent. The authors considered the layer to be a fluid layer with an infinite Prandtl number, which is applicable to the solid state convection of icy and rocky layers within satellites [Spohn and Schubert, 2003]. According to Grasset and Parmentier [1998] the onset of convection, and thus the presence of a stagnant lid regime, depends on the value of the Rayleigh number for the layer in question. The Rayleigh number is a dimensionless parameter which gives the ratio of two different timescales: the growth timescale for convective plumes and the timescale of thermal diffusion [Barr and Pappalardo, 2005]. In other words, it indicates how stable (or unstable) a layer is against convection. The Rayleigh number is calculated by Equation 2.1, where α = 1.6E-4 K^{-1} is the thermal expansion coefficient for ice, ρ = 1000 kg m^{-3} is the assumed density of ice, κ = 1.4E-6 m^2 s^{-1} is the thermal diffusivity of ice [Hussmann et al., 2002], D_{conv} is the thickness of the convective layer, $\eta\left(T_{int}\right)$ is the average viscosity of the convective sublayer and T_m and T_{top} are the melting temperature at the bottom of the ice shell and the temperature at the top of the convective layer respectively. A comparison between the sublayer thickness at which convection begins found in literature and that calculated in this work can be found in Appendix E.1.

$$Ra = \frac{\alpha\rho g\left(T_m - T_{top}\right) D_{conv}^3}{\kappa\eta\left(T_{int}\right)} \tag{2.1}$$

If the Rayleigh number of a layer is larger than the critical Rayleigh number then convection will be the dominant mode of heat transfer and the stagnant lid regime is applicable to that layer. If on the other hand the value of the Rayleigh number for that layer is less than the critical value the dominant heat transport mode is conduction and the stagnant lid regime will not be present. The value of the critical

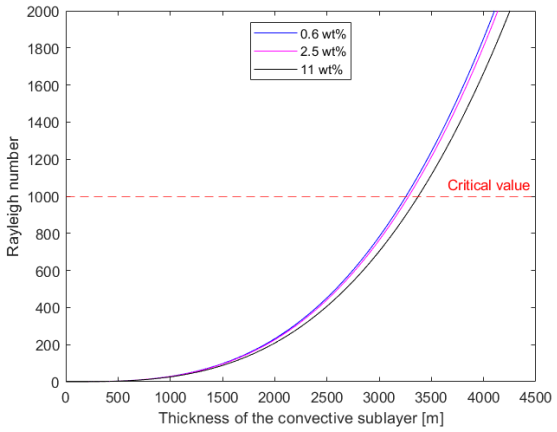

Figure 2.4: Rayleigh number as a function of convective sub-layer thickness. The different colors refer to the three different simulated cases. The critical Rayleigh number is set at 1000. Above this value convection sets in as the dominant mode of heat transport across the icy shell. For each case this is for an ice shell thickness between 3000 and 3500 m.

Rayleigh number is on the order of 10^3 [Hussmann et al., 2002]. Figure 2.4 show the Rayleigh number as a function of the thickness of the convective sublayer. The results for the three simulated cases are shown. The three cases are described in detail in Section 5.4. Figure 2.4 shows that the icy shell only starts convecting if the convective sublayer is at least 3000 m thick. If less than this value the assumption of a stagnant lid regime with a conductive lid and convective sublayer is not correct. In that case the icy shell is reduced to a single conductive layer. Note that Equation 2.1 includes the thickness of the convective sublayer D_{conv}, indicating that the presence of a convective layer is assumed even before the Rayleigh number is calculated and compared to the critical value. Only after this comparison it will be clear if the original assumption of a convective sublayer is correct or not. Section 2.3.4 gives a more detailed explanation the method by which the presence of a convective sublayer is determined.

The change in viscosity across a silicate mantle or ice layer can be large. Within a stagnant lid regime, however, the change in viscosity within the convective sub-layer is only a factor of 10. A greater change in viscosity occurs in the conductive lid [Grasset and Parmentier, 1998]. This was determined for a volumetrically heated layer but studies on convection within bottom heated layers report similar values [Grasset and Parmentier, 1998], suggesting this is applicable to both volumetrically as bottom heated layers. It must be noted that this is only the case for fluid layers with a strongly temperature-dependent viscosity. As the icy shell has a strong temperature-dependent viscosity [Tobie et al., 2003] this fixed change in viscosity across the convective layer is useful in determining the temperature profile of the icy shell, which is discussed below in Section 2.3.3.

Heat Transfer Through Latent Heat

Within the stagnant lid regime heat is transported through the ice shell via either conduction, convection or a combination of both. But if geysers are present part of the tidally generated heat will be transported to the surface through latent heat of the rising vapor molecules in the geysers. The amount of heat that is transported through this mechanism can be calculated with the following equation,

$$Q_{latent} = \dot{m}_{Io} \cdot L \tag{2.2}$$

where Q_{latent} is the amount of heat transported in the form of latent heat, $\dot{m}_{Io}$ is the mass eruption rate of Io and L is the latent heat of vaporization and is equal to $2.8{\cdot}10^6$ J kg^{-1} [Spencer et al., 2009]. The corresponding amount of latent heat that is transported through the icy shell for an example case can be seen in Table 2.4, together with the total amount of tidally generated heat. In this example the production rate of Io $\dot{m}_{Io}$ was equal to 122.8 $\cdot 10^3$ kg/s, which is the production rate of the low-end average case towards the end of the simulation. From Table 2.4 it is clear that including the amount of latent heat

does not significantly change the thickness of the ice layer and the total amount of tidal heating. The amount of latent heat is less than 0.4% of the total tidally generated heat and was the highest fraction over all cases at any time during their lifetime. The convergence criterion between heat transfer through the icy shell and the total amount of tidal heat is set at a difference of less than 1%. Because the inclusion of heat transfer through latent heat is less than this requirement it will not be included in the model.

Table 2.4: The effect of including heat transport through the latent heat of the rising vapor molecules on the resulting equilibrium thickness of the ice shell.

Case	Latent heat [w]	Tidal heat [W]	Ice shell thickness [m]
Latent heat not included	0	9.7630 E13	232.1854
Latent heat included	3.4390 E11	9.7836 E13	232.4642

2.3.3 Temperature Profile of the Icy Shell

The temperature profile of the icy shell indicates how the temperature changes across the shell and can be seen on the right of Figure 2.7. The four important temperatures are the melting temperature at the bottom of the icy shell T_m, the average internal temperature of the convective sublayer T_{int}, the temperature at the boundary between the stagnant lid and the convective sublayer T_{top} and the surface temperature T_s. These four temperatures are discussed below.

At the base of the ice shell the temperature is equal to the melting temperature T_m of the ice at that depth [Hussmann and Spohn, 2004]. The melting temperature is pressure dependent and can be calculated using Equation 2.3 [Hussmann and Spohn, 2004]. Note that the pressure in Equation 2.3 is depth dependent and given in MPa and that it is valid for pure ice only. As this work assumes a H_2O-layer of pure ice it is acceptable to use this equation.

$$T_m(P_r) = 273.15 \left(1 - \frac{P(r)}{395.2}\right)^{1/9} \tag{2.3}$$

The calculated melting temperature with increasing depth is shown in Figure 2.5a and can be compared to the results from Hussmann et al. [2002] which are shown in Figure 2.5b. There is a very slight difference in melting temperature as the thickness of the ice layer becomes very large. This might be because here a constant gravitational acceleration with depth was assumed while Hussmann et al. [2002] might not have used a constant value. For an icy Io with a H_2O-layer of 140 km the gravitational acceleration at the surface is about 1.6575 m s^{-2} while that at the ocean-mantle boundary is about 1.797 m s^{-2}. The difference between using the surface gravitational acceleration and that at the ocean-mantle boundary results in a difference in melting temperature of only 3K. In reality the gravitational acceleration will change between these values with increasing depth but the above result suggests that the difference in using a constant or changing value is negligible, especially considering the thickness of the icy shell remains less than 350 m for every simulated case (see Section 6.2) and Figure 6.2c). The authors do not mention if they used a constant value or not. Nevertheless based on the similarities the calculated melting temperature can be taken as correct and used as the base from which the complete temperature profile is determined.

The average internal temperature of the convective sublayer T_{int} is almost constant across the whole layer. In this case the convective sublayer is heated primarily from below meaning that the internal temperature is approximately the average of the melting temperature T_m and the temperature at the top of the convective sublayer T_{top} [Hussmann et al., 2002] as given below.

$$T_{int} \approx 0.5\,(T_m + T_{top}) \tag{2.4}$$

In order to determine the temperature T_{top} at the boundary between the convective sublayer and the conductive lid one can use the temperature dependent viscosity $\eta\,(T)$ of the sublayer as given by the following parameterization [Hussmann et al., 2002].

$$\eta\,(T) = \eta_0 exp\left[l\left(\frac{T_m}{T} - 1\right)\right] \tag{2.5}$$

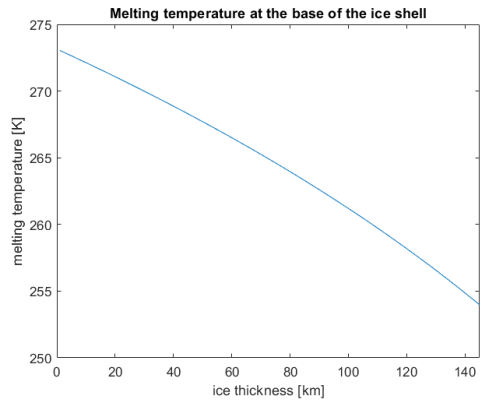

(a) Calculated melting temperature with depth

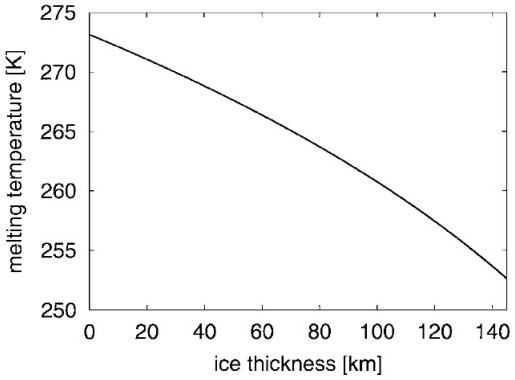

(b) Melting temperature with depth [Hussmann et al., 2002]

Figure 2.5: The melting temperature at the bottom of the ice shell is shown here for several different ice shell thicknesses. **Left** shows the calculated values and **right** shows the values calculated by Hussmann et al. [2002]. Both figures are quite similar, any differences are discussed in text.

In Equation 2.5 η_0 is the reference or melting-point viscosity and varies between 10^{13} and 10^{16} Pa s, depending on the source (see for example Hussmann et al. [2002], Tobie et al. [2003] and Rhoden et al. [2020]). Here the value of 5E13 Pa·s is chosen and this is assumed constant at the base of the icy shell [Hussmann and Spohn, 2004]. The parameter l is dimensionless and lies between 18 and 35, depending on amongst others the type of material [Kirk and Stevenson, 1987]. It is related to the activation energy for creep. Here a value of 27 will be used in analogy with Hussmann and Spohn [2004]. T and T_m are the temperature and melting temperature respectively. Note that the melting temperature at the corresponding depth must be used in Equation 2.5. Thus at the top of the convective sublayer the melting temperature at a depth of D_{stag} must be used. As mentioned before within a stagnant lid regime the viscosity is ten times larger at the top of the convective sublayer than at the bottom [Hussmann et al., 2002]. Combining this with Equation 2.5 the temperature at the top of the convective sublayer can be determined with the following Equation [Hussmann and Spohn, 2004].

$$T_{top} = \frac{T_m\left(D_{stag}\right)}{\frac{\ln 10}{l} + 1} \tag{2.6}$$

Lastly the value of the surface temperature T_s is dependent on the latitude and can be calculated by Equation 2.7 where σ is the Stefan Boltzmann constant and equal to $5.7{\cdot}10^{-8}\mathrm{Wm}^{-2}\mathrm{K}^{-1}$, θ is the latitude and F is the solar flux at Jupiter's orbit and equal to 50.46 Wm^{-2} and A is the albedo of ice and is equal to 0.5 [Tobie et al., 2003].

$$T_s = \left[\frac{(1-A)}{\sigma} F \frac{cos(\theta)}{\pi}\right]^{1/4} \tag{2.7}$$

The surface temperature for each latitude is shown in Figure 2.6 and is seen to vary between 110 K at the equator and 60K at the poles. Even though the surface temperature is latitude dependent often a constant value is used. For the Galilean satellites the used value is often set at 100 K (see Hussmann and Spohn [2004] for a rocky Io, Tobie et al. [2003]for Europa and Bland et al. [2009] for Ganymede) and the same approach will be adopted here.

In conclusion the temperature profile of the icy shell can be determined completely using Equations 2.3, 2.4 and 2.6 together with the surface temperature which is set at 100 K [Hussmann et al., 2002]. Note that if no convection occurs the temperature profile is much simpler. In that case the temperature at the bottom of the stagnant lid is equal to the melting temperature. Across the lid the temperature then decreases steadily as the radius increases until it reaches the surface temperature at the top of the stagnant lid.

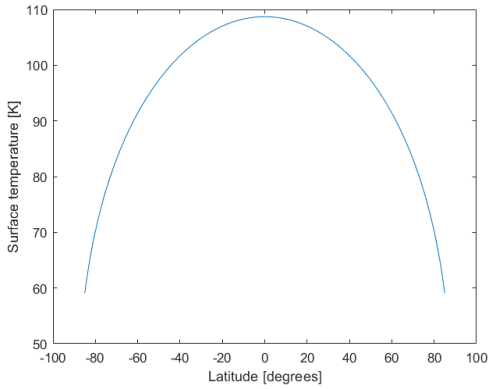

Figure 2.6: Latitude-dependent surface temperature of Io. For simplicity the surface temperature is kept constant at 100K.

2.3.4 Relative Sublayer Thickness

This section will discuss how the thickness of each sublayer within the icy shell is calculated. The method that was used to determine the interior structure of the H_2O-layer is the one that was used by Hussmann et al. [2002] and will be explained here. The main assumption of this method is that the moon is in an equilibrium state meaning that the internal temperature does not fluctuate much [Hussmann and Spohn, 2004]. In such a state the heat flow through the icy shell will be equal to the tidal dissipation within the whole moon. In this case any tidal dissipation in the icy shell must be zero as a nonzero dissipation would cause the heat flow in to the icy shell to be different than the heat flow out of the icy shell. In reality there is some tidal dissipation within the icy shell but it is negligible compared to the heat dissipation within the silicate mantle thus it may be ignored. Considering the maximum case at the end of the simulation, when the ice shell is thickest, the tidal heating within the silicate layer is 8 orders of magnitude larger than the tidal heating within the ice shell. Another heat source that is ignored here is radiogenic heating from the decay of radioactive isotopes. This is further discussed in Section 3.2.1. This equilibrium assumption then dictates that the heat flow through every layer is equal to each other. A schematic representation is given by the red arrows in Figure 2.7. In mathematical form this equilibrium condition is given by

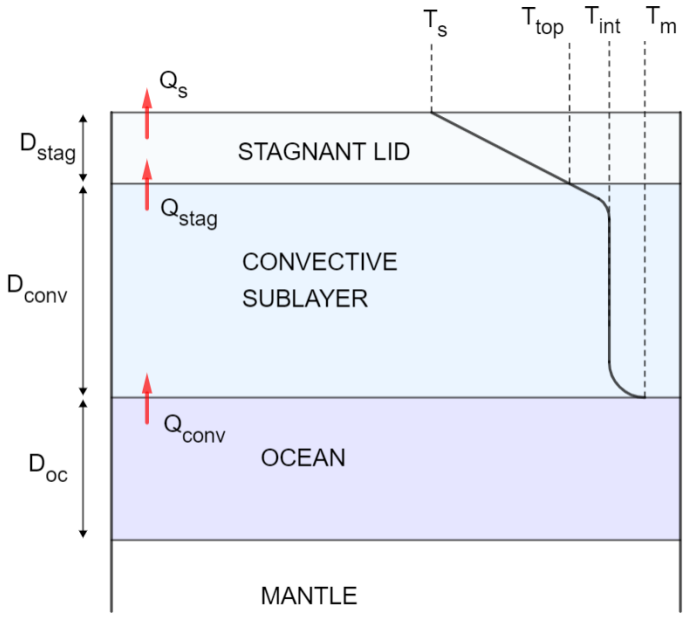

Figure 2.7: Schematic overview of the H_2O-layer and its thermal profile

Equation 2.8. In this equation Q_{stag} is the heat flow going in to the stagnant lid, Q_{conv} is that going in to the convective sublayer, Q_s is the heat flow out of the surface and Q_{tidal} is the tidally generated heat.

$$Q_{stag} = Q_{conv} = Q_s = Q_{tidal} \tag{2.8}$$

Note that Figure 2.7 and Equation 2.8 are for a convecting icy layer. If convection does not occur then the convective sublayer will not be present and Q_{conv} must be removed.

There are two starting conditions in these calculations. The first is that the icy shell is convecting meaning that it consists of a convective sublayer and an overlying stagnant lid. Under this condition the equilibrium solution is calculated and afterwards its validity is checked by calculating the Rayleigh number and comparing it to the critical value. The second starting conditions is that the total thickness of the icy shell is equal to an initial estimate D_{ice}. The value of this initial estimate is a user-defined input at the start of a simulation (see Section 5.2 for more information). The thickness of the individual layers of the icy shell can thus be calculated using the two following conditions.

1) Equal heat flow through the layers, $Q_{stag} = Q_{conv}$

2) The total thickness is equal to the initial estimate, $D_{ice} = D_{stag} + D_{conv}$

The heat flows coming out of the convective layer and the stagnant lid are given by Equations 2.9 and 2.10 respectively [Hussmann et al., 2002].

$$Q_{conv} = \frac{k_{conv} \cdot (T_m - T_{top})}{D_{conv}} \cdot \left(\frac{Ra}{Ra_c}\right)^{\beta} \cdot 4\pi \left(R - D_{stag}\right)^2 \tag{2.9}$$

$$Q_{stag} = \frac{k_{stag} \cdot (T_{top} - T_s)}{D_{stag}} \cdot 4\pi R^2 \tag{2.10}$$

The thickness of the layers are D_{conv} and D_{stag} and the thermal conductivities are k_{conv} and k_{stag}. In Equation 2.9 Ra is the Rayleigh number and Ra_c is the critical number while β a dimensionless parameters. The thermal conductivities are temperature dependent and can be calculated using Equation 2.11 [Hussmann et al., 2002]. The thermal conductivity for the convective sublayer is based on T_{int} and that of the stagnant lid is based on the average of the surface temperature and T_{top}.

$$k(T) = 567/T \tag{2.11}$$

Now a solution can be calculated that satisfies the two conditions mentioned above which from hereon is called the temporary solution. This is done using a Newton root finding algorithm which works as follows (for a detailed calculation see Appendix A.1). It starts with an initial estimate for the thickness of the convective sublayer x_0. Then using the function f and its derivative f' the new value x_1 is calculated which is closer to the root than the initial guess x_0. This process is repeated until x_n and x_{n+1} are sufficiently close to each other. This process is given in Equation 2.12.

$$x_{n+1} = x_n - \frac{f(x_n)}{f'(x_n)} \tag{2.12}$$

This method only works if the initial guess is close enough to the solution. It is difficult to state how close as this depends on the specific problem at hand. If one is interested in the root in a specific interval, a poor initial guess might converge to a different root. Other possible outcome is that the method might keep cycling without reaching convergence or it might diverge to infinity. If one knows in which interval the solution lies one can keep the initial guess to a value within this interval, if not one could graph the function (if at all possible) and use this to obtain an initial estimate. In this work a sensitivity test is done on the choice of the initial guess. The sensitivity to the initial guess, change in initial guess and the convergence criterion are discussed in Section C.2. The convergence criterion is set at 1% difference as there was no difference in end result for a convergence criterion between 10% and 0.01%. Therefore in order to save on computational time it was set at 1% as less iterations are required to reach convergence. If no convergence is obtained the initial guess is too far from the actual root. In that case the initial guess

is increased and the process repeated. Here the initial guess is set at 1 m and is increased by 100 if no convergence is obtained. Once the temporary solution is obtained the assumption that the icy shell is convecting must be revisited.

Depending on the value of the Rayleigh number two possibilities exist. The first possibility is that the Rayleigh number is larger than the critical value meaning that the icy shell is convecting. In that case the obtained temporary solution is kept. The second possibility entails that the Rayleigh number is lower than the critical value which means that the icy shell is purely conductive. In that case there will be no convective sublayer and only a stagnant lid. The thickness of this lid is then simply equal to the initial estimate of the thickness of the total ice layer D_{ice}. In that case the heat flow through the stagnant lid is calculated straight from Equation 2.10 but the temperature at the bottom of the stagnant lid T_{top} must be replaced by the melting temperature T_m.

2.4 Interior of the Silicate Mantle

The properties of rocky Io will remain constant except for the viscosity, shear modulus, temperature and corresponding melt fraction of the silicate mantle. Because no separate asthenosphere is included in the model the viscosity and shear modulus of the silicate mantle are parameterized to mimic the effect of the partially molten mantle. The equilibrium assumption requires that the heat flow out of the mantle is equal to the heat flow in to the stagnant lid (see Equation 2.13). These heat flows are also equal to the heat flow in to the convective sublayer but because this layer will not always be present the heat flow in to the stagnant layer is used here.

$$Q_{mantle} = Q_{stag} \tag{2.13}$$

The objective is then to determine what mantle properties will result in a heat flow such that the condition described in Equation 2.13 is met. How to calculate the value of these four parameters is discussed in Section 2.4.1 and the methodology describing how to obtain a mantle with properties that will satisfy the condition given in Equation 2.13 is given in Section 2.4.2.

2.4.1 Mantle Properties

Mantle Heat Flow

Instead of using the total heat flow it is also possible to use the heat flow per unit area. The heat flow coming out of the mantle depends on the thermal conductivity of the mantle k_m, the temperature difference between the top and the bottom of the mantle ΔT, the thickness of the mantle d_m and the Nusselt number Nu as follows [Shoji and Kurita, 2014].

$$q_m = k_m \frac{\Delta T}{d_m} Nu \tag{2.14}$$

The Nusselt number is given by [Shoji and Kurita, 2014],

$$Nu \approx 0.5\theta^{-4/3} Ra^{1/3} \tag{2.15}$$

where θ is the Frank-Kamenetskii parameter, which is given by Equation 2.16 [Shoji and Kurita, 2014], and Ra is the Rayleigh parameter, which is given by Equation 2.1 (note that the temperature difference $T_m - T_{top}$ needs to replaced by the temperature difference ΔT of Equation 2.17).

$$\theta = \Delta T \frac{E}{R T_m^2} \tag{2.16}$$

In the above equation the temperature difference ΔT is equal to that of Equation 2.14, E is the activation energy, set at 300 kJ mol^{-1}, R is the universal gas constant and T_m is the average mantle temperature [Shoji and Kurita, 2014]. Using Equations 2.1, 2.15 and 2.16 the heat flow from the mantle q_m as given in Equation 2.14 can be written as follows,

$$q_m = \frac{k_m}{2} \left(\frac{\rho_m \cdot g_m \cdot \alpha_m}{\kappa_m \cdot \eta_m} \right)^{\frac{1}{3}} \gamma^{-\frac{4}{3}} \tag{2.17}$$

where k_m, ρ_m, α_m, κ_m, η_m and g_m are respectively the thermal conductivity, density, thermal expansivity, thermal diffusivity, viscosity and gravitational acceleration of the mantle. Values for some of these parameters are given in Table 2.5. Furthermore γ is defined as [Shoji and Kurita, 2014]:

$$\gamma = \frac{E}{RT_m^2} \tag{2.18}$$

where E is the activation energy, set at 300 kJ mol^{-1} [Shoji and Kurita, 2014] and R is the universal gas constant. The viscosity of the mantle η_m depends on both the mantle temperature and the mantle melt fraction.

Mantle Melt Fraction

The melt fraction of the mantle is calculated using Equation 2.19 [Shoji and Kurita, 2014].

$$\phi = \frac{T_m - \bar{T}_{sol}}{\bar{T}_{liq} - \bar{T}_{sol}} \tag{2.19}$$

The bars indicate average values for the mantle. Using the same reasoning as Hussmann and Spohn [2004] the average values of the liquidus and solidus temperatures are the averaged values of these temperatures at the top and the bottom of the mantle.

$$\bar{T}_{sol} = 0.5 \cdot [T_{sol}(r_m) + T_{sol}(r_c)] \tag{2.20}$$

$$\bar{T}_{liq} = 0.5 \cdot [T_{liq}(r_m) + T_{liq}(r_c)] \tag{2.21}$$

In equations 2.20 and 2.21 r_m and r_c are the outer radii of the mantle and core respectively. The liquidus and solidus temperatures at a given radius are dependant on the pressure at that point as given by Equations 2.22 and 2.23 respectively [Takahashi, 1990]. Note that the pressures in these equations are in GPa.

$$T_{sol} = 1409.15 + 134.2P - 6.581P^2 + 0.1054P^3 \tag{2.22}$$

$$T_{liq} = 2035 + 57.46P - 3.487P^2 + 0.0769P^3 \tag{2.23}$$

Thus before the melt fraction can be determined the internal pressures are required.

Internal pressures

The internal pressure at the ocean-mantle and core-mantle boundaries depend on the overlying structure. The applicable equations and the corresponding calculations are given in Appendix A.2.

Mantle Viscosity

The value of the mantle viscosity depends on the amount of melt that is present. The melt fraction can either be 0 in which the mantle is completely solid or it can be between 0 and 1 in which case the mantle is partially molten or it can be larger than 1 and the mantle is completely molten. However the effect of liquid dominates in the still partially molten mantle if the melt fraction is larger than the rheological critical melt percentage RCMP [Shoji and Kurita, 2014]. According to Moore [2003] the RCMP lies between 40 and 60%. One can then consider two cases: if the melt fraction lies below the RCMP the viscosity is calculated using Equation 2.24 and if the melt fraction lies above the RCMP it is calculated using Equation 2.25 [Shoji and Kurita, 2014]. The mantle viscosity will be assumed constant for the whole mantle and thus the average mantle temperature T_m is used in these equations.

$$\eta_m = \eta_{m,0} \cdot exp\left(\frac{E}{R}\left[\frac{1}{T_m} - \frac{1}{T_0}\right]\right) \cdot exp\left(-B\phi\right) \tag{2.24}$$

$$\eta_m = 10^{-7} \exp\left(\frac{4 \cdot 10^4}{T_m}\right)(1.35\phi - 0.35)^{-5/2} \tag{2.25}$$

Here $\eta_{m,0} = 1{\cdot}10^{16}$ Pa·s [Rovira-Navarro et al., 2021] is the reference or melting-point viscosity of the mantle at the reference temperature T_0 of 1600 K, $B = 30$ is the dimensionless melt fraction coefficient [Shoji and Kurita, 2014] and ϕ is the melt fraction. Now all required parameters are known in order to calculate the heat flow per unit area out of the mantle with Equation 2.17.

Mantle Shear Modulus

Lastly the shear modulus is calculated, which is not required to determine the equilibrium solution but is necessary to calculate the tidal dissipation. The same two cases as with the mantle viscosity will be considered here. If the melt fraction is above the RCMP the shear modulus is set at 10^{-7} [Moore, 2003] and if the melt fraction is between 0 and the RCMP the shear modulus of the mantle μ_m is given by Equation 2.26, here $\mu_1 = 8.2 \cdot 10^4$ K, $\mu_2 = -40.6$ and $\Delta T_m = T_m - \bar{T}_{sol}$. [Shoji and Kurita, 2014].

$$\mu_m = 10^{\left[\frac{\mu_1}{\Delta T_m + 1600} + \mu_2\right]} \tag{2.26}$$

2.4.2 Methodology

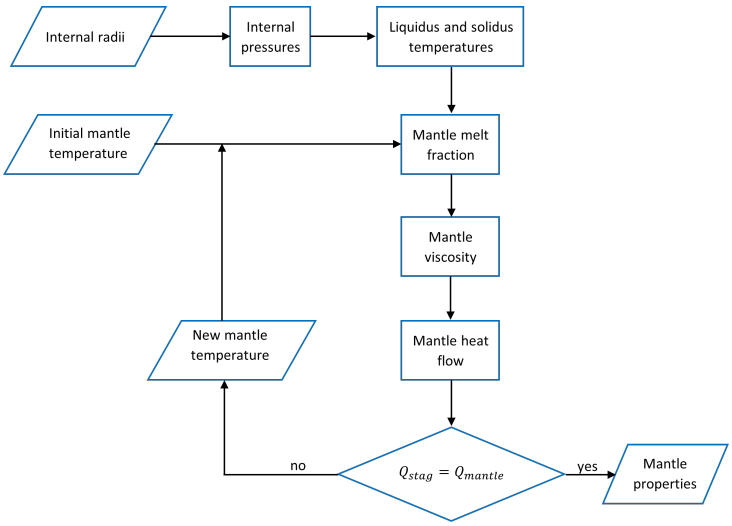

Figure 2.8: Flowchart indicating the process to determine the mantle temperature, melt fraction, viscosity and shear strength. Parallelograms indicate input or output parameters, rectangles indicate calculations and diamonds indicate a choice or comparison.

The method to determine the properties that will satisfy the condition given in Equation 2.13 is explained below and given schematically in Figure 2.8. The required input are the radii of the core and mantle which can be found in Table 2.2. First the pressures at the core-mantle and ocean-mantle boundaries are calculated as they are required for the solidus (see Equation 2.22) and liquidus temperatures (see Equation 2.23) and at these boundaries. The internal pressure is depth dependent and thus also requires the thickness of the H_2O-layer as well. The average solidus and liquidus temperatures of the mantle are calculated using Equations 2.20 and 2.21 respectively. From these the melt fraction can be calculated with Equation 2.19 using an initial estimate for the mantle temperature. The sensitivity to the initial estimate of the mantle temperature and the convergence criterion has been tested. The results of these tests and a discussion about those results can be seen in Appendix C.3. The first results of these tests is that resulting mantle temperature is insensitive to the initial choice for the mantle temperature. The choice is thus made that the initial mantle temperature is set equal to the solidus temperature of the mantle for the particular case at hand. The second result of these tests is that the actual mantle temperature is the same whether the convergence criterion is set at 1, 0.1 or 0.01 %. Thus to save on computational time the convergence criterion is set at 1%. Using the mantle temperature and melt fraction the corresponding mantle viscosity and shear modulus can be determined with Equations 2.24 or 2.25 and 2.26 respectively. Finally this set of parameters then dictates the amount heat flow out of the mantle which is determined through Equations 2.17 and 2.18. If this is not equal to the heat flow in to the stagnant lid then the estimate for the mantle temperature is not correct and needs to be adjusted. This process will be repeated until convergence between the two heat flows has been reached. The corresponding values for the mantle parameters discussed above are then added to the temporary solution.

Table 2.5: Values for several mantle parameters [Shoji and Kurita, 2014]

Symbol	Parameter	Value
k	Thermal conductivity	4 W m^{-1} K^{-1}
κ	Thermal diffusivity	1 E-6 m^2s^{-1}
α	Thermal expansivity	4 E-5 K^{-1}

2.5 Conclusion

This chapter has described the internal structure of an icy Io. While it is dependent on the amount of water that is present in the H_2O-layer the three simulated cases as described in Section 5.5 all contain too little water for the presence of high-pressure ices. Thus the internal structure of icy Io will look similar to that of Europa, which has a metallic core, a silicate mantle and an overlying H_2O-layer [Schubert et al., 2004]. The H_2O-layer will consist of a subsurface ocean and an ice-I shell on top for which a stagnant lid regime is assumed. Within such a regime the icy shell may consist of a convective sublayer and a conductive lid if convection is the dominant mode of heat transport or it may just be a conductive lid if conduction is the dominant mode of heat transport. Which mode is dominant depends on the Rayleigh number with a Rayleigh number higher than the critical value indicating convection as the dominant mode of heat transport and a value lower than the critical value indications conduction of the heat transport. The only parameters of the silicate mantle that are variable within the used approach are the temperature, melt fraction, viscosity and shear modulus. The values of these parameters and the thicknesses of the conductive lid and convective sublayer (if present) are such that the heat flow through the icy shell is equal to the heat flow coming out of the silicate mantle, as required by the assumed equilibrium condition of icy Io's interior. The internal structure that complies with the equilibrium condition is called the temporary solution. The temporary solution is then the corresponding internal structure of the H_2O-layer as given in Section 2.3 and the values of the different variable mantle properties described in Section 2.4. Next the amount of tidal dissipation that occurs based on this temporary solution is calculated. This process, and some background information on tidal dissipation itself, can be found in Chapter 3.

Chapter 3

Tidal Dissipation

3.1 Introduction

This chapter will investigate the phenomenon of tidal dissipation and its role in the thermal-orbital evolution of a satellite. Even though a lot of this chapter is applicable to other moon-planet systems as well here the specific case of Io and Jupiter will be considered. More details on tidal dissipation and its source are given in Section 3.2. Each layer within Io will experience tidal heating but the magnitude of this tidal heating varies significantly across each layer. How to calculate the magnitude of tidal dissipation that a body experiences can be found in Section 3.3 together with the specific methodology that is used in this work. Tidal dissipation effects the orbital migration rate of a satellite and is discussed in Section 3.4. Finally Section 3.5 shows how the tidal dissipation can be compared to the heat flow through the icy shell (see Chapter 2) in order to obtain the equilibrium solution.

3.2 Origin of Tidal Dissipation

Tidal dissipation is a result of gradients in Jupiter's gravitational field. Due to these gradients the gravitational forces Io experiences will be higher at its sub-jovian point (the closest point to Jupiter) and lowest at its anti-jovian point (the point that is furthest away from Jupiter). The difference in these gravitational forces across Io are defined as the tidal forces and will deform Io. Tidal forces on Io are not constant but variable thus Io is constantly deformed during its orbit. Because Io is made up of viscous material it will resist this deformation resulting in some lag between the tidal forces and the deformation which leads to dissipation of energy. The energy required to deform Io is taken from the planet-moon system and is dissipated within Io as heat. The term tidal dissipation refers to the dissipation of this energy within Io. The term tidal heating the refers to the heating of Io's interior due to the dissipated energy. The deformation of Io will result in a tidal bulge [Murray and Dermott, 1999]. A moon's tidal bulge would remain fixed if its orbit has zero eccentricity, if the satellite would have zero obliquity (meaning that its spin axis is perpendicular to its orbital plane) or if the satellite is in synchronous rotation [Jara-Orué and Vermeersen, 2011]. Because this is not the case for Io its tidal bulge will librate resulting in periodic deformation and heating up Io's interior.

3.2.1 Radiogenic Heating

A second source of heating that must be mentioned is called radiogenic heating. The source of this heating is the decay of radioactive isotopes. The four most important isotopes are ^{235}U, ^{238}U, ^{232}Th and ^{40}K [De Pater and Lissauer, 2015]. Radiogenic heating within moons is calculated with Equation 3.1 [Hussmann et al., 2010]. Here m_{sil} is the mass fraction of silicates within a moon, q_i is the specific heat of each isotope, λ is the decay constant, t is the time at formation and t_{pr} is the present time. Note that the subscript i represents the four isotopes.

$$Q_{rad} = m_{sil} \sum_{i=1}^{4} q_i e^{\lambda_i (t - t_{pr})}, \tag{3.1}$$

In moons without significant tidal heating radiogenic heating can be an important heat source [De Pater and Lissauer, 2015]. For Io this is not the case as the tidal heating is orders of magnitude larger than the amount of radiogenic heating [Moore, 2003]. At present the radiogenic heating rate of Io is between 3.08 and $5.14 \cdot 10^{11}$ W and at the time of formation it would have been between 2.50 and $4.15 \cdot 10^{12}$ W [Hussmann et al., 2010]. The range in values stems from the uncertainty of the exact composition of Io's rocky material. The lower estimates mentioned above correspond with a composition similar to LL (low iron, low metal) chondrites and the higher estimates correspond with a composition similar to CI carbonaceous chondrites. These two compositions are the most extreme cases and different compositions will lead to radiogenic heating rates between these two limits. The estimated radiogenic heating rates are significantly less than the tidal heating rates for the simulated cases, which are on the order of 10^{13} W at the end of the simulations (present time) and on the order of 10^{15} W at the start of the simulations (time of formation). Thus the difference is at least two orders of magnitude indicating that radiogenic heating will not have a large impact and may be ignored.

3.3 Calculating the Tidal Dissipation

The amount of tidal dissipation within a moon $\dot{E}$ can be calculated using Equation 1.1 [Segatz et al., 1988], where R is the surface radius of the moon, n is the mean motion of the satellite, e is the eccentricity of the satellite's orbit, G is the gravitational constant and $Im(k_2)$ is the imaginary part of the tidal potential Love number. The tidal potential Love number k describes the response of a moon to a tidal potential and its imaginary part $Im(k_2)$ describes how the interior structure effects the dissipation rate. The value of $Im(k)$ depends on the interior structure and rheology of the moon but also on the forcing frequency of the tidal forces which is the mean motion of the satellite [Hussmann et al., 2002]. Section 3.3.1 shows how to calculate the value of $Im(k_2)$ and Section 3.3.2 describes which methodology is used in this work to calculate that value.

3.3.1 Determining the Tidal Potential Love Number

The magnitude of tidal dissipation within Io can be calculated by Equation 1.1 and is dependent on the surface radius R, mean motion n, eccentricity e and the imaginary part of the Love number $Im(k_2)$. While the values of the first three parameters are easy to obtain that of the Love number k_2 is not. This section will discuss how this can be done using the matrix propagator method described by Jara-Orué and Vermeersen [2011] and Sabadini et al. [2016]. A summary of this method is given below. First a way of representing the deformation of each layer is shown followed by a description of the matrix propagator technique and finally a short description of the required boundary conditions is given.

Tidal Deformation

The objective is to calculate the value of the tidal potential Love number k_2, which describes the response of a moon to the tidal potential ϕ_T. The tidal potential is a way of expressing the tidal forces that affect a moon [Jara-Orué and Vermeersen, 2011]. The different layers within a moon will be deformed by the tidal potential. In order to determine the deformation the equations of motion that describe this deformation can be transformed to the Laplace [Jara-Orué and Vermeersen, 2011] or Fourier [Rovira-Navarro et al., 2021] domains through the correspondence principle as defined by Peltier [1974] [Sabadini et al., 2016]. In doing this the deformation of each layer within a moon is described by new equations of motion: the 6 so-called radial functions $y_1(r)$ to $y_6(r)$. These radial functions depend on the distance r from the core. Continuing from here the dependence on r will no longer be explicitly mentioned for the sake of clarity. The 6 radial functions represent the radial displacement (y_1), the tangential displacement (y_2), the radial stress (y_3), the shear stress (y_4), the gravitational potential (y_5) and the potential stress (y_6). This results in a set of differential equations as given by Equation 3.2. The six radial functions are contained in the vector $\mathbf{Y}$ and the matrix A is defined by the material parameters of the moon and the radial distance [Sabadini et al., 2016].

$$\frac{d\mathbf{Y}}{dr} = A\mathbf{Y} \tag{3.2}$$

Linearly independent solutions of Equation 3.2 must be found for each layer within the moon with appropriate boundary conditions (described below) [Sabadini et al., 2016]. When solving Equation 3.2

mass and linear momentum must be conserved and thus the momentum equation needs to be solved for the whole interior of the moon. Furthermore the tidal potential ϕ_T must satisfy the Poisson equation [Sabadini et al., 2016].

The Propagator Matrix Technique

The solution to Equation 3.2 can be written as follows,

$$\mathbf{y}_i(r,\omega) = \mathbf{Y}_i(r,\omega)\,\mathbf{C}_i \tag{3.3}$$

where ω is the tidal forcing frequency or mean motion, r is the radial distance, Y is a fundamental matrix (see Equation 2.42 of Sabadini et al. [2016]) and $\mathbf{C}$ is a vector consisting of integration constants. The solution at the surface of the moon is obtained by propagating the solution at the core-mantle boundary upwards through each layer and is given by the following equation [Rovira-Navarro et al., 2021],

$$\mathbf{y}(R,\omega) = \left(\prod_{i=1}^{N-1} \mathbf{Y}_i(r_i,\omega)\,\mathbf{Y}_i^{-1}(r_{i+1},\omega)\right) I_c C_c \tag{3.4}$$

where I_c is the core-mantle boundary matrix (given by Equation 2.6 of Sabadini et al. [2016]) and C_c is a vector of integration constants which can be obtained from surface boundary conditions [Sabadini et al., 2016]. The surface boundary conditions are that the surface is stress-free and that the potential stress at the surface equals $(2l+1)/R$ where R is the surface radius and l is the spherical degree harmonic [Rovira-Navarro et al., 2021]. The propagator matrix is then given as [Jara-Orué and Vermeersen, 2011]

$$\mathbf{B} = \left(\prod_{i=1}^{N-1} \mathbf{Y}_i(r_i,\omega)\,\mathbf{Y}_i^{-1}(r_{i+1},\omega)\right) I_c \tag{3.5}$$

Finally a value of the tidal potential Love number k_2 can be obtained from the following equation [Rovira-Navarro et al., 2021].

$$k_2 = y_5(R) - 1 \tag{3.6}$$

Boundary Conditions

When propagating the solution at the core-mantle boundary towards the surface different layers will be encountered. Sabadini et al. [2016] call these boundaries chemical boundaries where material is unable to pass from one layer to another. Between these layers discontinuities in material parameters such as density and viscosity may exist. Between viscoelastic layers the solution that is propagated must be continuous. This means that at the top boundary of layer j (at distance r_J) the value of each radial function at the boundary must be equal when approaching the boundary from above (r_j^+) or from below (r_j^-). Mathematically this can be written as follows [Sabadini et al., 2016].

$$\mathbf{y}\left(r_j^+\right) = \mathbf{y}\left(r_j^-\right) \tag{3.7}$$

The above continuities only hold for the boundaries between two viscoelastic layers. Changes must be made if one of the interior layers is a subsurface ocean as an ocean is not able to transfer mechanical properties such as stress. Only the gravitational potential y_5 can be propagated through the ocean [Sabadini et al., 2016]. In those cases the layer above the subsurface ocean is mechanically decoupled from the layer below the subsurface ocean. To propagate the solution at the core-mantle boundary to the surface in such a case the propagation must be done in three different steps [Jara-Orué and Vermeersen, 2011]. First the solution is propagated from the core-mantle boundary through the viscoelastic layers to the base of the ocean by using the viscoelastic propagator matrix as described in Equation 3.5. Within the ocean the solution is propagated by means of a fluid propagator matrix to the top of the ocean. Finally the solution is again propagated using the viscoleastic propagator matrix from the top of the ocean to the surface. The fluid propagator matrix can be derived similarly to the viscoelastic propagator matrix and is given by Equation 9.18 of Sabadini et al. [2016]. In order to couple the radial functions at the boundaries with the ocean appropriate boundary conditions must be set. These boundary conditions are given by Equations 9.19 and 9.21 of Sabadini et al. [2016] for the ice-ocean interface and ocean-mantle interface respectively.

3.3.2 Using Radial Weight Functions

Once the six radial functions have been determined calculating the total dissipation rate by using the matrix propagator method described in Section 3.3.1 is very time-consuming. This is because the solution is calculated for multiple points on the surface requiring a large amount of calculations. If one is only interested in the amount of tidal heating the method developed by Beuthe [2013] is much faster (see Table 3.1 for a comparison between the two methods).

In his paper, Beuthe [2013] simplifies the three-dimensional problem of predicting spatial tidal heating patterns to a one-dimensional one. In this one-dimensional approach radial weight functions are determined in order to calculated the amount of dissipated power. At radius r the dissipated power can be calculated by the following equation [Beuthe, 2013].

$$P_0 = \frac{\omega\,(nR)^4}{2r^2} Im\,(\tilde{\mu})\,H_\mu \Psi_0 \tag{3.8}$$

Here r is the radial distance at which the power is calculated, R is the surface radius, n is the mean motion, ω is the angular velocity and $\tilde{\mu}$ is the complex shear modulus. In the case of synchronous rotation $n = \omega$ and Ψ_0 can be defined as [Beuthe, 2013]:

$$\Psi_0 = \frac{21}{5} e^2 \tag{3.9}$$

Lastly the parameter H_μ is the sum of the weight functions mentioned above:

$$H_\mu = f_A + f_B + f_C \tag{3.10}$$

The weight functions are given by Equations 3.15, 3.12 and 3.13 and are all taken from Beuthe [2013] and are dependent on the radial functions mentioned in Section 3.3.1. It must be noted that different authors use different notations regarding these radial functions. Equations 3.11 to 3.14 use the radial functions as described by the model of Rovira-Navarro et al. [2021] who uses the notation from Sabadini et al. [2016]. Beuthe [2013] used the notation of Takeuchi and Saito [1972] thus the equations given here modified versions of those found inBeuthe [2013].

$$f_A = \frac{4}{3} \left| r y_1' - y_1 + 3 y_2 \right|^2 \tag{3.11}$$

$$f_B = 6 \left| \frac{r y_4}{\tilde{\mu}} \right|^2 \tag{3.12}$$

$$f_C = 24 \left| y_2 \right|^2 \tag{3.13}$$

$$r y_1' = -2 y_1 + 6 y_2 \tag{3.14}$$

With Equation 3.14 Equation 3.11 becomes:

$$f_A = \frac{4}{3} \left| -3 y_1 + 9 y_2 \right|^2 \tag{3.15}$$

The tidal dissipation in a layer ranging from r_1 to r_2 can then be calculated with Equation 3.16.

$$\dot{E} = 4\pi \int_{r_1}^{r_2} P_0 r^2 dr \tag{3.16}$$

Substituting P_0 from Equation 3.8, Ψ_0 from Equation 3.9, using $n = \omega$ and rearranging results in the following equation.

$$\dot{E} = \frac{42}{5} \pi n^5 R^4 e^2 \int_{r_1}^{r_2} Im\,(\tilde{\mu})\,H_\mu dr \tag{3.17}$$

The integral in Equation 3.17 is calculated numerically with Simpson's rule. For a detailed calculation see Appendix A.3.

The goal of using this more efficient method was to save time and a comparison between the two methods can be found in Table 3.1. In this comparison the tidal dissipation, both per layer and in total, was calculated for Io. The tidal dissipation was calculated twice, once with 100 radial points per layer and once with 500 radial points per layer. With the matrix propagation method the six radial functions are determined for each internal layer. This is done for a specific number of vertically spaced points within each sublayer. These points are called the radial points which are mentioned above. As can be seen the time savings are substantial while both methods gave the same results. Verification of the tidal dissipation calculations can be found in Appendix E.3. The main conclusion here is that the model is able to calculate the correct amount of tidal dissipation.

Table 3.1: Time to calculate tidal dissipation within Io

	Length of calculation [s]	
Radial points	Matrix propagator method	Method using weight functions
100	19	0.4
500	332	1

3.4 Tidal Migration

Tidal dissipation not only affects the internal structure of moons but also their orbits. The change in orbital parameters is called orbital migration and when considering orbital migration due to tidal dissipation only it is sometimes referred to as tidal migration. Tidal migration of a moon is not only affected by tidal dissipation within the moon itself but also by tidal dissipation within its host planet. Fortunately it is possible to consider the effect due to tidal dissipation in the planet and the moon separately [Hussmann et al., 2010]. First the effect of tides on the planet will be discussed in Section 3.4.1 and then the effect of tides on the moon will be discussed in Section 3.4.2. The combined result of both of these is discussed in Section 3.4.3. Lastly the initial semi-major axis and Jovian Quality factor for an icy Io and how to determine them are discussed in Section 3.4.4.

3.4.1 The Effect of Tidal Dissipation Within Jupiter

The tidal bulge that arises on Jupiter is not perfectly aligned with the planet-satellite axis. The corresponding tidal torque leads to an exchange in angular momentum between Jupiter and Io. In the case of Jupiter and Io this will cause Jupiter's spin rate to decrease while Io's semi-major axis is increased. Furthermore this will also cause a change in eccentricity of Io's orbit. In this work however a constant eccentricity is adopted so this effect will not be included. The rate of change of Io's semi-major axis due to tidal dissipation within Jupiter is given by Equation 3.18 [Hussmann et al., 2010]. Note that this equation is valid for the case where the inclination and eccentricity are low and the satellite is not in any resonance. Io, however, is in resonance with Europa and Ganymede but the effects of this resonance are not included in this work. This limitation allows for the use the following equation.

$$\frac{da}{dt} = 3\left(\frac{k_2}{Q}\right)_J \frac{m_s}{m_p}\left(\frac{R_p}{a}\right)^5 na \tag{3.18}$$

In Equation 3.18 a is the semi-major axis, m_s is the mass and n is the mean motion which are all related to Io. The radius R_p, mass m_p and the fraction k_2/Q are all related to Jupiter. The present-day value of k_2 for Jupiter is equal to 0.379 [Gavrilov and Zharkov, 1977]. The Jovian quality factor Q_J indicates how much energy and angular momentum is transferred in to the orbital system of the Galilean satellites. Estimations range between 10^4 and 10^6 [Hussmann and Spohn, 2004] whereby lower values indicate more energy being transferred to the Galilean satellites because of higher tidal torques and higher values indicates less energy being transferred. Lainey et al. [2009] determined the present-day value of Q_J to be $3.56 \pm 0.66 \cdot 10^4$ based on astrometric observations. A lower limit of the Jovian quality factor was set at $6 \cdot 10^4$ by [Yoder and Peale, 1981], who based the result on the expansion of the Galilean satellites and assumed that the Laplace resonance of the Galilean satellites is primordial and that their eccentricities are constant. That may explain the difference between the estimates of Yoder and Peale [1981] and Lainey

et al. [2009]. It is thus clear that the determined value depends on which approach was used. Adding to the range of possible values for the Jovian Quality factor is the fact that it is unclear if this value is constant over time [Hussmann et al., 2010]. Ogilvie and Lin [2004] and Wu [2005] note that the value of Q_J depends on the forcing frequency of the tide-inducing body, which is not constant. Wu [2005] finds a time-averaged value for Q_J of 10^7, but this may be as high as 10^9. Fuller et al. [2016] investigated the influence of resonance locking on the value of Q and tidal migration of the moons of Jupiter ans Saturn. The authors found that a constant Q implies that several moons formed billions of years after the planet they are orbiting. According to the authors resonance locking predicts that values for Q_J were initially much higher and decreased over time. Each simulated case will have a different value for the Jovian Quality factor as it is directly linked to the amount of tidal migration icy Io will undergo. This is discussed in detail in Section 3.4.4. By rearranging Equation 3.18 and rewriting the mean angular motion n as in Equation 3.19 and integrating over time the change in semi-major axis over a certain time-step $t_{new} - t_0$ can be calculated. The final result after integration is given by Equation 3.20

$$n = \sqrt{\frac{\mu}{a^3}} \tag{3.19}$$

$$a_{new} = \left[\frac{39}{2}\left(\frac{k_2}{Q}\right)_J \frac{m_s}{m_p} R_p^5 \sqrt{\mu}\,[t_{new} - t_0] + a_0^{13/2}\right]^{2/13} \tag{3.20}$$

3.4.2 The Effect of Tidal Dissipation Within Io

Due to it's eccentric orbit, Io will be continuously deformed by Jupiter's gravitational field. This tidal deformation causes tidal dissipation within Io. The tidal bulge on Io will therefore also be misaligned from the planet-satellite axis. The resulting effect is a decrease of Io's semi-major axis and can be seen in Equation 3.21 [Hussmann et al., 2010]. Note that again this equation is based on the assumption of a small eccentricity and without any resonances. As mentioned above, the effects of the Laplace resonance with Europa and Ganymede are not included in this work, therefore the use of Equation 3.21 is acceptable. Again the effect on the eccentricity of Io's orbit will not be included as it is assumed constant in this work.

$$\frac{da}{dt} = -21\left(\frac{k_2}{Q}\right)_I \frac{m_p}{m_s}\left(\frac{R_s}{a}\right)^5 nae^2 \tag{3.21}$$

In Equation 3.21 a is the semi-major axis, m_s is the mass, n is the mean motion, e is the eccentricity and R_s is the radius. These parameters together with the fraction k_2/Q are all related to Io. Only the mass m_p is related to Jupiter. Lainey et al. [2009] found that a value of 0.015 ± 0.003 for the ratio k_2/Q for Io results in a good agreement with the present-day observed surface heat flow. This result is based on the internal energy dissipation of the present-day rocky Io. Even though this work considers an icy Io, with a H_2O layer above the present-day rocky Io, almost all tidal dissipation occurs in the silicate mantle. Therefore it is assumed that the value obtained by Lainey et al. [2009] is also applicable for this work. Using the same reasoning as in Section 3.4.1 the change in semi-major axis over a certain time-step $t_{new} - t_0$ can be calculated by integrating Equation 3.21 and is given below.

$$a_{new} = \left[-\frac{273}{2}\left(\frac{k_2}{Q}\right)_I \frac{m_p}{m_s} R_s^5 e^2 \sqrt{\mu}\,[t_{new} - t_0] + a_0^{13/2}\right]^{2/13} \tag{3.22}$$

3.4.3 The Combined Migration Rate

As can be seen from Equations 3.20 and 3.21 the effect of tidal dissipation within Jupiter results in an increasing orbit for Io and that of tidal dissipation within Io results in a decreasing orbit. The actual change in semi-major axis will thus be the result of these two opposing movements [Hussmann et al., 2010] and can thus be determined by simple addition of Equations 3.18 and 3.21. The resulting change in semi-major axis over a certain time-step $t_{new} - t_0$ is given by,

$$a_{new} = \left[\left(\frac{39}{2}\left(\frac{k_2}{Q}\right)_J \frac{m_I}{m_J} R_J^5 \sqrt{\mu} - \frac{273}{2}\left(\frac{k_2}{Q}\right)_I \frac{m_J}{m_I} R_I^5 e^2 \sqrt{\mu}\right)(t_{new} - t_0) + a_0^{13/2}\right]^{2/13} \tag{3.23}$$

where the subscripts I and J refer to Io and Jupiter respectively. Even though an icy Io will lose mass over time Equation 3.23 assumes a constant mass and surface radius during each time-step of the simulation. After each time-step the mass and surface radius will be re-calculated and implemented in the next time-step, over which they will remain constant until the next re-calculation. Note that this approach neglects any possible change in eccentricity of Jovian Quality factor.

3.4.4 Initial Semi-major Axis and Jovian Quality Factor

To determine icy Io's initial semi-major axis one can rearrange Equation 3.23 as follows.

$$a_0 = \left[a_{new}^{13/2} - \left(\frac{39}{2} \left(\frac{k_2}{Q} \right)_J \frac{m_I}{m_J} R_J^5 \sqrt{\mu} - \frac{273}{2} \left(\frac{k_2}{Q} \right)_I \frac{m_J}{m_I} R_I^5 e^2 \sqrt{\mu} \right) (t_{new} - t_0) \right]^{2/13} \tag{3.24}$$

Equation 3.24 shows that the change in semi-major axis depends on several parameters including one that has not been discussed yet, namely the time step $t_{new} - t_0$, and two parameters which are relatively unknown: the Jovian quality factor Q_J and Io's initial semi-major axis a_0. The time step in this case is the time between the formation of Io and the present day. The values for these three parameters are discussed below.

It is unknown at what time Io formed exactly. What is known is that Io formed after Jupiter, whose formation ended within about 10^7 years after the formation of the Sun [De Pater and Lissauer, 2015]. The estimated accretion timescales for the Galilean satellites differ depending on the protosatellite disk model that is used. The Solid-Enhanced Minimum Mass (SEMM) model of Mosqueira and Estrada [2003] estimates that Callisto formed within about 10^6 years, Ganymede within about 10^4 years and even less for Europa and Io. The gas-starved accretion disk model by Canup and Ward [2002] estimated accretion times of more than 10^5 years for the Galilean satellites. In this model the formation of the Galilean satellites occurs at the end of Jupiter's formation, when the gas giant is accreting the last of its mass. The results of both models indicate that the formation of Io was over relatively quickly. In the simulations of Hussmann and Spohn [2004] the age of Io was set equal to that of the Solar System. Here the formation of Jupiter will be taken in to account such that the age of Io is set at $4.59 \cdot 10^9$ years.

To determine Io's initial semi-major axis one must look at the different migrations Io has undergone over its lifetime. During formation the Galilean satellites experienced an inward migration [Peale and Canup, 2015]. This type of migration is called type-I migration and is due to the interaction of the forming satellite with the gas of the protosatellite disk and is increased with increasing gas density in the disk. It is thought that several forming satellites were lost to Jupiter and that the present Galilean moons are the last ones that were formed and survived [Canup and Ward, 2009]. Their survival is due to the fact that the gas density of the protosatellite disk lessened as the gas inflow from the disk waned, which caused type-I migration to halt. Since then tidal dissipation has caused Io to migrate outward significantly [Fuller et al., 2016]. The Laplace resonance with Europa and Ganymede originated during this outward migration. Presently Io's migration is thought to be inward due to eccentricity dampening and has been observed through astrometric observations [Lainey et al., 2009]. Even though Io is migrating inward at present, this is not representative of its long-term migration history [Fuller et al., 2016]. As Io has undergone a net outward migration since its formation one can put two limits on the initial semi-major axis. The lower limit is a physical limit and is equal to Io's Roche limit which is defined as the distance at which Io's internal strength is equal to the tidal forces working on Io. If Io would have migrated inwards of the Roche limit it would have been disintegrated due to the magnitude Jupiter's tidal forces. The Roche limit a_R depends on the radius of the host planet R_P and the density of the host planet ρ_p and the orbiting moon ρ_s and is calculated with the following equation [De Pater and Lissauer, 2015].

$$a_R = 1.44 R_p \left(\frac{\rho_p}{\rho_s} \right)^{\frac{1}{3}} \tag{3.25}$$

The upper limit of the initial semi-major axis is a soft limit and is equal to its present-day value. In this scenario there would have not been any net migration. Even though Io has migrated outward since its formation, this covers the scenario where Io would have migrated to a position further than its present-day position and more recently migrated inwards again. This is a possible scenario according to the results of Lainey et al. [2009], which indicate Io is migrating inwards at present. Unfortunately it is not known how

long Io has been migrating inward so it is difficult to put any hard constraints on this scenario.

Using the Jovian quality factor as the free variable one can calculate the range of possible initial semi-major axes that fall within these limits (the Roche limit and the present-day semi-major axis). As mentioned in Section 3.4.1 there is a large uncertainty for the value of Q_J, however multiple studies have proposed different upper and lower limits which gives a range of possible values one can work with. The initial semi-major axis depends on several parameters (see Equation 3.24). The three parameters that are of importance here are the mass of icy Io m_I, the radius of icy Io R_I and the Jovian quality factor Q_J. The mass and radius follow directly from the mass of the H_2O-layer. Considering Q_J as a free parameter the initial semi-major axis for each value of Q_J can be determined. The chosen combination of Q_J and initial semi-major axis is the one that is closest to, but larger than, the corresponding Roche limit. This will ensure that icy Io experiences the largest magnitude of tidal dissipation possible at the time of formation.

Process to Determine the Initial Values

The process of determining the initial semi-major axis, Jovian Quality Factor and initial mass of the H_2O-layer will be explained below. This is done using the following trial-and-error process.

- Step 1: choose an estimate for the initial mass of the H_2O-layer
- Step 2: determine the corresponding values for a_0 and Q_J
- Step 3: calculate the mass loss rate for these conditions
- Step 4: estimate the required time to remove the whole H_2O-layer
- Step 5: repeat until a case is found where the estimated required time is less than the age of the Solar System

When closest to Jupiter the mass loss rate will be highest and continue to diminish over time. Therefore the estimates mentioned above will be underestimates of the actual required time and it is preferable to choose an initial mass of the H_2O-layer that requires a removal time that is significantly less than the age of the icy Io. The solution spaces for the three simulated cases can be seen in Figures 3.1a, 3.1b and 3.1c for the maximum, high-end average and low-end average cases respectively. These results are very close to the estimated present-day value for the Jovian Quality Factor obtained by Lainey et al. [2009], which is $3.56 \pm 0.66 \cdot 10^4$. They are also close to the results obtained by Fuller et al. [2016], who suggest that the value of the Jovian quality factor (from its interaction with Io) lies between $4 \cdot 10^4$ and $2 \cdot 10^5$.

When using the above trial-and-error process to determine the initial values of each simulated case one must make sure that the required removal time is not too close to the age of icy Io. In those cases a specific issue arises, namely that tidal migration could be too fast. The surface stress diminishes with increasing distance from the planet. If tidal migration occurs too fast at a certain point the surface stress will be too low to permit geyser activity on any point on icy Io. If by then not all ice is removed Io will remain icy which is clearly at odds with the present-day situation. An example of this can be seen in Figure 3.3. Figure 3.3a shows the mass of the H_2O-layer. It decreases steadily until about $4 \cdot 10^9$ years when the rate of change diminishes and eventually reaches zero. The graph of the mass is then flattened out, showing the now constant mass. Figure 3.3b shows why this happens. At the time the rate of change becomes zero the eruptive area has been reduced to zero. This could be either due to the surface stress remaining under the threshold for crack instigation or the surface stress being too low for crack propagation resulting in an insufficient crack length.

In this section the total migration rate of Io since its formation has been discussed. Since Io has experienced a net outward migration the Roche limit is taken as the lower limit for the initial semi-major axis and the present-day value is taken as the upper limit. As gravitational forces and thus tidal heating are higher when Io is closer to Jupiter the chosen solution is the one that has an initial semi-major axis as close as possible to the Roche limit. This will give an upper limit to the amount of ice that is possibly lost as the magnitude of tidal dissipation is increases with a decreasing semi-major axis. This minimum

Figure 3.1: The solution space for the three simulated cases.

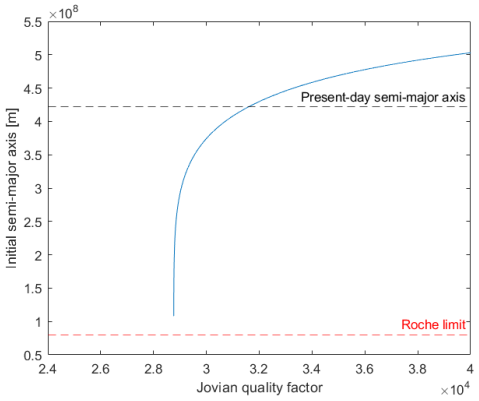

(a) Maximum case

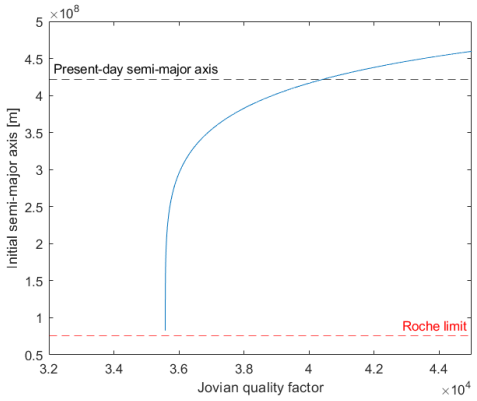

(b) High-end average case

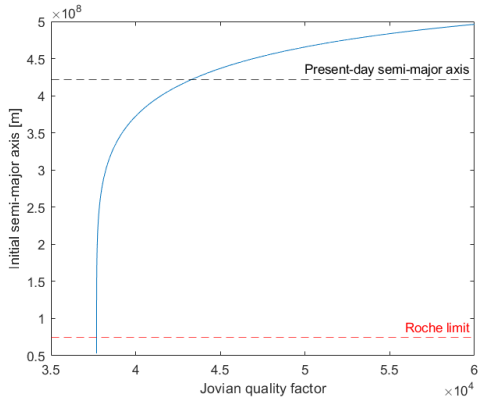

(c) Low-end average case

Figure 3.2: Solution spaces for the tidal migration of the three cases. Using the Jovian quality factor as a free parameter possible initial semi-major axes can be found that will cause the satellite to migrate towards its present-day distance from Jupiter. The Roche limit was set as a hard minimum distance for the initial semi-major axis and the present-day semi-major axis was set as a soft maximum limit for the initial semi-major axis.

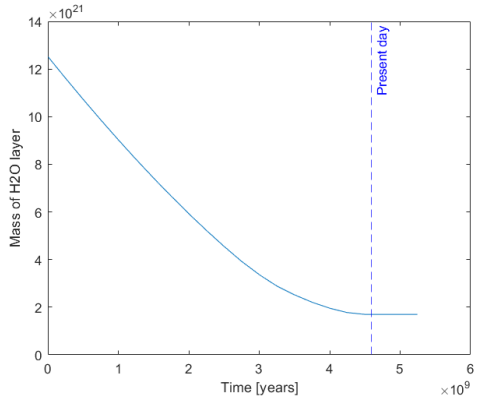

(a) Mass remaining in the H_2O-layer

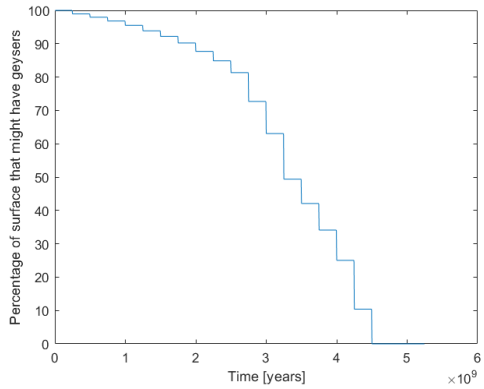

(b) Eruptive area

Figure 3.3: Example of a migration rate that is too rapid. In such a case the satellite reaches a distance from Jupiter where the required surface stress falls below the failure threshold before the H_2O-layer has been completely removed.

semi-major axis corresponds to a certain value for the Jovian quality factor Q_J (see Figure 3.2). As discussed above the obtained values for the two examples lie within the range suggested in the literature (see for instance Lainey et al. [2009]and Fuller et al. [2016]). Care must be taken to check that the minimal solution yields a plausible Jovian quality factor for cases with a different amount of H_2O. It must be noted that certain assumptions were made in the discussion above. First is that any change in eccentricity has been ignored. Furthermore the influence of the Laplace resonance has also been omitted, as this goes beyond the scope of this work. Lastly the value of Q_J is assumed constant, even though this is probably not the case [Fuller et al., 2016]. Nevertheless the value that arises from the chosen solution can be seen as an average value over the course of Io's life. Including a changing value is beyond the scope of this work.

3.5 The Equilibrium Solution

The equilibrium solution is defined as the internal structure whereby the heat flow through each layer (which is given by the temporary solution as described in Chapter 2) is compared to the tidal dissipation as calculated in Chapter 3. Because these can not be compared directly the surface heat flow that follows from the tidal dissipation is calculated first. Now there are two heat flows which can be directly compared to each other and according to the assumed equilibrium conditions it is required that these two are equal to each other. They are again deemed sufficiently close if the difference between them is less than 1%. A sensitivity test on the convergence criterion was performed for which the details can be found in Appendix C.1. This test showed that applying a convergence criterion of less than 1% did not improve the accuracy of the results but did significantly increase the computational time whereas a convergence criterion of more than 1% resulted in less accurate results. Therefore the convergence criterion was set at 1%. If the difference between the stagnant lid heat flow and the surface heat flow from tidal dissipation is larger than the allowed 1% the whole process described in Chapters 2 and 3 is repeated but with a different initial estimate for the ice shell thickness. The new initial estimate of the ice layer thickness is based on an adaptive step size. How large this step size is depends on the magnitude of the difference between the stagnant heat flow and tidal dissipation. Once convergence is reached this process stops and the obtained interior structure is then called the equilibrium solution. Once the interior structure is determined it will be possible to determine the amount of geyser activity and corresponding rate of ice loss. This whole process is described in Chapter 4. Appendix D describes the test that has been done to determine if the equilibrium solution is indeed unique. In this test the equilibrium solution was calculated for several different H_2O-layers ranging from 0.1 to 50 wt% of Io's present day mass. For each of these cases several different initial estimates for the thickness of the ice shell were used. The results show that for each different H_2O-layer the resulting equilibrium ice shell thickness was the same, irrespective of what the initial estimate for the ice shell thickness was. This confirms the uniqueness of the equilibrium solution.

3.6 Conclusion

Tidal heating within moons is caused by a periodic deformation by which energy is dissipated. The source of this deformation are gradients in the gravity field of the host planet. Tidal forces arise from these gradients and are represented by a tidal potential when calculating the tidal dissipation. This work combines the matrix propagator technique by Jara-Orué and Vermeersen [2011] and Sabadini et al. [2016] and the method created by Beuthe [2013] to determine the amount of tidal dissipation within icy Io. The heat flow due to this dissipation is compared to the heat flow through the ice shell as determined in Chapter 2. If equal the equilibrium solution is found and if not equal a new initial estimate for the ice shell thickness is used and the whole process described in Chapters 2 and 3 is repeated until convergence is obtained. Tidal dissipation also has an influence on the migration rate of a satellite. The tidal migration rate depends on the amount of dissipation in Io as in Jupiter and thus must be combined to determine the actual tidal migration rate. By assuming a constant Jovian Quality Factor the initial semi-major axis for each case can be determined. The final choice of Jovian Quality Factor is the value that results in the initial semi-major axis that is closest to, but still larger than, Jupiter's Roche limit because inside the Roche limit Io would be disintegrated due to the magnitude of the tidal forces.

Chapter 4

Geysers

4.1 Introduction

There are several possible ice loss mechanisms that could have contributed to an icy Io's overall ice loss. The chosen ice loss mechanism in this work is geysers. The first main reason for this is that they are the cause of Enceladus' mass loss [Bierson and Steinbrügge, 2021] and have been studied extensively. The second main reason is that an icy Io experiences a lot of tidal heating which is expected to melt part of the H_2O-layer and thus form a liquid reservoir required for geyser activity. The geysers of this work are based on the model of Schmidt et al. [2008] who propose that the geysers on Enceladus have a subsurface liquid reservoir as a source which is connected to the surface by cracks. Therefore the cracks that contribute to the geyser activity must run through Enceladus' ice shell from the surface to the underground reservoir. Vapor molecules and icy grains are then able to accelerate through these cracks and erupt at the surface. In this work the presence of an underground liquid reservoir, an overlying ice shell and the presence of cracks running through the icy shell are considered the conditions for the existence of geysers. As mentioned earlier icy Io's geysers will be modeled on the intensively studied geysers of Enceladus. A closer look will be taken at Enceladus to better understand its cryovolcanic activity followed by an investigation of the applicability of Enceladus' geysers to an icy Io. Once this has been established Enceladus' geyser activity will be parameterized so that it may be upscaled to icy Io. The important parameters describing Enceladus' geyser activity are the production rate, which is the mass flow out of the geysers, the eruption velocity, which is the velocity at which the erupting material exits the cracks and the velocity distribution, which is a mathematical way of expressing the spread in the eruption velocity of all the erupting molecules. Once Enceladus' geyser activity has been parameterized it can be upscaled to icy Io and finally the actual mass loss of icy Io can be determined.

Several different possible ice loss mechanisms are described in Section 4.2. The three conditions for the existence of geysers are discussed in Section 4.3. The applicability of Enceladus' geyser activity and its parameterization can be found in Section 4.4. Section 4.5 gives an overview of the model of icy Io's geysers and a description of the method by which the actual mass loss is determined.

4.2 Ice Loss Mechanisms

Broadly one can start from two scenarios, either Io never contained any ice or at some point it did contain ice but subsequently lost it through some unspecified ice loss mechanism(s). Studies have been done that support both scenarios, such as that of Canup and Ward [2002] for the scenario where Io never contained any ice and that of Bierson and Nimmo [2020] for the scenario where Io once contained ice but subsequently lost it over its lifetime. As the starting point of this work is an icy Io only the latter case will be included. In the scenario where Io did once contain icy the ice loss mechanisms can be divided in two categories. The first category contains the mechanisms which occurred during formation and are discussed in Section 4.2.1. The second category contains the mechanisms which occurred after formation and are discussed in Section 4.2.2.

4.2.1 During Formation

Imperfect Accretion

Moons are formed within protosatellite disks surrounding their host planets. The method of formation is called accretion, whereby planetesimals accumulate material through gravitational attraction. The result of encounters between planetesimals within protosatellite disks depends on the mass and velocity of both planetesimals and their impact angle. Dwyer et al. [2013] find such encounters mostly happen between planetesimals of different size and mass as two larger bodies will probably be trapped within resonances and will not encounter each other. Following the nomenclature used in Dwyer et al. [2013] the more massive of the two planetesimals will be called the target and the smaller one the impactor. When two planetesimals encounter each other their accretion can be perfect or imperfect. With perfect accretion no material is lost during impact and the resulting body's mass is the sum of the mass of the target and the impactor. With imperfect accretion some mass is lost and the mass of the resulting body is less than the sum of the mass of the target and impactor. It must be mentioned that accretion is not a necessary outcome of an encounter between two planetesimals. It is also possible that the two simply graze each other with little change in mass or that the encounter results in a catastrophic event where the target is destroyed of left with less than 10% of its original mass [Dwyer et al., 2013].

The authors considered two ice loss mechanisms that could occur during an imperfect accretion. The first one is physical erosion where fragments are broken off and subsequently lost to the target. The second mechanism is vapor erosion where water (or ice) is vaporized during impact and also lost to the target. Dwyer et al. [2013] caution that they assume no re-accretion and fully differentiated bodies resulting in an overestimation of ice loss during imperfect accretion. On fully differentiated bodies all ice is concentrated on the outside meaning that any lost material is pure ice. If those bodies would not be fully differentiated the outer layer would be a mixture of ice and rock and any lost material will be part ice and part rock. The simulations of Dwyer et al. [2013] show that if all bodies start with an initial ice mass fraction of 55% this fraction would decrease due to imperfect accretion but the ice mass fractions of the present day satellites would not be reached. Adopting an initial ice mass fraction that is radially-dependent also did not result in the present-day ice mass fractions.

Hydrodynamic Escape

Hydrodynamic escape is an ice loss mechanism that is applicable to bodies with high temperatures and low gravity [Bierson and Nimmo, 2020]. In such bodies an influx of energy from radiation and accreting material will warm up their outer layer. If enough energy is added to the outer layer it could melt forming an ocean which in turn would create an atmosphere around the body. Due to a pressure difference between the surface and the background a vertical wind could arise starting at the surface. The velocity would increase with increasing distance from the surface eventually reaching velocities that are high enough to allow for hydrodynamic escape. Bierson and Nimmo [2020] were able to reproduce the density gradient of the present-day Galilean satellites by using a protosatellite disk as proposed by Canup and Ward [2002] within which the density, pressure and temperature decreases with increasing distance from Jupiter. As the vertical winds arise from a pressure difference bodies closer to Jupiter will experience less hydrodynamic escape as the background pressure is much higher than at locations further away from Jupiter for identical satellites. There were two assumptions in the work of Bierson and Nimmo [2020] that will have an impact on their results. The first is that all disk conditions remained static and the second is that satellite migration is not included. These two assumptions have an affect on the conditions at the locations of formation of the satellites and thus also on the rate of hydrodynamic escape. As both disk conditions changed and Io migrated during formation the results of this study might not hold if both of these phenomena are included.

4.2.2 After Formation

High-velocity Impacts

Impacts after satellite formation, such as during the Late Heavy Bombardment (LHB) event, happen at high velocities of up to 30 km/s [Nimmo and Korycansky, 2012]. High-velocity impacts and their role in ice-loss of the Galilean satellites was studied by Nimmo and Korycansky [2012] with a focus on the LHB.

Their simulations assumed that all impactors had a radius between 7.5 and 100 km and that all vapor produced during impacts was lost to the impacted satellite. Under these assumptions Io could have lost up to 40 % of its present-day mass to such high-velocity impacts. While this method would be able to explain Io's loss of ice its results for Saturn's moon Mimas and Uranus' moon Miranda shed some doubt on the validity of this ice loss mechanism. According to the simulations both moons could have lost an amount of mass equal to their present-day mass through high-velocity impacts. Dwyer et al. [2013] note that this would have removed almost all of their ice while present-day ice mass fractions of Mimas and Miranda are estimated ate 82% and 77% respectively [Hussmann et al., 2010]. The authors propose three reasons as to why their simulations provide such contradicting results. The first being that the amount of mass that was delivered to the satellites during the LHB might be severely overestimated. The second being that their assumption of a large amount of smaller impactors may be wrong. If instead the LHB consisted of only a few massive impactors and one of these would have missed the target satellite the resulting mass loss through erosion would be much less. Lastly their scenario assumes that the satellites had been formed before the LHB but if they formed after the LHB it would not have been possible to cause ice loss through this method. In conclusion it might be possible that Io lost a lot of ice through high-velocity impacts but it is not sure if it actually happened.

Tidal Heating

Tidal heating is not an ice loss mechanism in itself but a source of energy that can be used to remove ice [Dwyer et al., 2013]. Because of the Laplace resonance between Io, Europa and Ganymede Io's orbit has remained eccentric. It is possible that the Laplace resonance is primordial with Peale and Lee [2002] estimating that it has been present for $4.5{\cdot}10^9$ years. This would have contributed to the tidal heating rate which, if added up over Io's lifetime, adds up to a lot of tidally generated heat. Canup and Ward [2009] estimate that if all tidally generated heat within Europa would have been used to vaporize and remove ice it is possible, from an energetic standpoint, that a mass of ice equal to its current mass could have been removed. This would of course require a mechanism which is 100% efficient in using the tidally generated heat to remove the ice. According to Dwyer et al. [2013] the amount of ice that could be lost (from an energy point of view) can be approximated by Equation 4.1 where ΔM is the mass that is lost, M and R are the satellite mass and radius respectively, $\dot{H}$ is the tidal heating rate, G is the gravitational constant, t is the duration of the tidal heating and ϵ is an efficiency factor.

$$\frac{\Delta M}{M} \sim \frac{\dot{H} R t}{G M^2} \epsilon \tag{4.1}$$

The two important parameters here are the time of tidal heating and the efficiency factor of the actual ice loss mechanism. The combination of these two factors will give a good indication of what ice loss mechanism could have contributed to the ice loss of a moon. Dwyer et al. [2013] determined that the present-day tidal heating rate of Europa (about 10^{12} W) and an efficiency factor of 1 the time required to remove a significant amount of ice would be about $3{\cdot}10^9$ years. If Europa would have experienced a tidal heating rate more similar to that of Io (about 10^{14} W) a timescale of $1{\cdot}10^6$ years would result in the same amount of mass loss.

Bierson and Steinbrügge [2021] adopted the same energy-driven approach to determine the validity of ice loss through tidal heating for Io as well as Europa. The authors started from the premise of an icy Io with an ice mass fraction of 34%. They considered this ice to be lost if it was vaporized and transported to Jupiter's Hill radius. For an ice mass fraction of 34% which would require about $1{\cdot}10^{30}$ J. Assuming that the current tidal heating rate for Io has been constant over the last 4.5 Gyr the amount of energy available for ice loss is about $3{\cdot}10^{31}$ J. Dividing the required energy by the available energy gives an indication of how efficient the ice loss mechanism should be, which is about 3%. Using these simple assumption the authors then looked in to several ice loss mechanisms to see which could have been efficient enough to remove the ice. They conclude that direct mass loss through geysers or Jeans escape from a geyser-sustained atmosphere would not have been efficient enough to remove all of the ice. In their calculations Bierson and Steinbrügge [2021] assumed that the eruption velocity on Io would be the same as that on Enceladus and they included icy grains in the geysers. As to the vapor molecules that erupt through geysers the authors investigate two different mechanisms namely ion-driven atmospheric sputtering and Jeans escape. Atmospheric sputtering is a process where neutral molecules within an atmosphere are impacted by ions. Such impacts can lead to a chain of collisions whereby it is possible that some particles are ejected from the

atmosphere [Wilson et al., 2002]. Bierson and Steinbrügge [2021] determine that the amount of mass that could be lost through atmospheric sputtering is four orders of magnitude too small to remove an ice layer equal to 34% of Io's weight. Jeans escape is the escape from an atmosphere of molecules that are moving faster than the escape velocity. In order to remove all Io's ice through Jeans escape the authors estimate that an atmosphere with a temperature of 300 K is required which, according to them, is not plausible.

One caveat of the work of Bierson and Steinbrügge [2021] is that they assume a constant tidal heating rate whereas it has been shown by thermal-orbital evolution models such as that of Hussmann and Spohn [2004] that the eccentricity and tidal heating rate vary over Io's lifetime. A second caveat is that the authors only considered an icy Io with a high ice mass fraction of 34% while the initial ice mass fraction of Io might have been much lower. Lower ice mass fractions are entirely possible due to the type-I migration that the Galilean satellites experienced during their formation [Canup and Ward, 2002]. If Io started to accrete outside of the snowline, where temperatures were low enough to allow for the presence of ice [Lunine, 2006], it would explain the presence of ice on Io. During formation type-I migration caused the accreting Galilean satellites to migrate inwards. If Io crossed the snow line relatively early in its formation further accretion of ice would have stopped, resulting in a low ice mass fraction. A different explanation could be that Io accreted more ice but that some of this ice was already removed due to processes which occurred during accretion such as those mentioned above. Both the type-I satellite migration and ice loss mechanisms during formation could account for a low ice mass fraction on Io at the end of its formation. The third caveat of their study is that they only consider the escape rate of erupted icy grains with an eruption velocity of 90 m s^{-1}. What they neglect are the erupted vapor molecules. Estimates for the eruption velocity of vapor molecules on Enceladus range from 350 m s^{-1} [Tian et al., 2007] to 1050 m s^{-1} [Dong et al., 2011] with eruption velocities of up to 2 km s^{-1} out of supersonic jets [Hansen et al., 2011]. These estimates are much closer to the escape velocity and could thus be an important source of mass loss.

The above discussion shows that tidal heating on Io has provided a lot of energy which could be used for the removal of ice. Tidal heating is the driver behind the geysers on Enceladus [Nimmo et al., 2014]. Geysers account for the mass loss of Enceladus, mass which forms Saturn's E-ring [Ingersoll and Ewald, 2011], [Bierson and Steinbrügge, 2021]. Therefore the chosen ice loss mechanism in this work are geysers because (1) geysers are a proven ice loss mechanism that is happening on Enceladus, (2) a lot of tidally generated heat has been available on Io over its lifetime to drive these geysers and (3) this tidally generated heat is able to create a subsurface ocean on an icy Io which could act as a reservoir for the geyser activity.

4.3 Conditions for the Existence of Geysers

4.3.1 Liquid Source

Schmidt et al. [2008] proposed a model of the geysers on Enceladus where an underground liquid reservoir, such as a subsurface ocean, is connected to the surface through thin cracks that run through the ice. This particular model is supported by both observations and models (see for example Hansen et al. [2008], Porco et al. [2014] and Yeoh et al. [2015]). Data from Cassini's UVIS instrument indicates that the source of the eruptions are cracks or fissures along the length of the Tiger Stripes [Hansen et al., 2011]. In this work a similar scenario will be adopted in order to model the ice loss of Io through geysers. In order for such a mechanism to exist three conditions must be met:

1) There must be a subsurface liquid reservoir

2) An icy shell must lie over the reservoir

3) The liquid reservoir must be connected with the surface through narrow cracks which span the entire thickness of the icy shell

Whether the first two conditions are met follows from the equilibrium solution as described in Chapters 2 and 3. The results of the three simulations show that at every point in time there exists a global subsurface ocean underneath an icy shell on an icy Io. In order for the third condition to be met the surface stress must be large enough for crack instigation. Once failure occurs the cracks must then propagate through

the icy shell and finally the crack depth must be larger than the thickness of the ice shell in order to reach the subsurface ocean.

4.3.2 Crack Instigation

Not only the plumes of Enceladus have been studied extensively but also the formation process of the Tiger Stripes has been investigated a lot (see for example Hemingway et al. [2020] and the works mentioned below). Tidal stresses have been proposed as the most likely mechanism (see for example Porco et al. [2014] and Patthoff et al. [2019]) but a detailed investigation of the Tiger Stripes using high-resolution images challenges this scenario [Yin et al., 2016]. The challenge for every proposed mechanism is to explain all the observed characteristics of Enceladus, such as the ongoing plume activity and the dichotomy between the active South Polar Terrain and the inactive north pole. Rhoden et al. [2020] assessed whether tidal stresses from Enceladus' eccentric orbit could produce fractures that matched the orientation of the Tiger Stripes. The points at which the authors calculated the orientations coincide with the observed locations of the Tiger Stripes and are shown on the right in Figure 4.4. Rhoden et al. [2020] find that eccentricity-driven tidal stresses are able to produce fractures with the same orientation as that of the Tiger Stripes. The authors investigated this for multiple interior models of Enceladus. The results that are of interest to the model of an icy Io as proposed in this work are those of the cases with thin icy shells of which the thickness is less than 5 km. For those cases peak stresses between 171 and 412 kPa were achieved. The authors then investigated what failure threshold would result in the observed orientations of the Tiger Stripes. In other words at what magnitude of stress would the ice crack and form fractures? Fractures with orientations nearly identical to those of the Tiger Stripes were formed when applying the same failure threshold to all modeled locations. The best results were obtained by applying a failure threshold of 100 kPa, which is equal to the estimated strength of the ice on Europa [Rhoden et al., 2020]. The authors do note that other stresses, such as the stress from a cooling and expanding ice shell, may also contribute to the failure of the ice but that, according to their work, it is not required. This work will adopt the same failure threshold and consequently will also neglect any other sources of stress. The maximum surface stress of icy Io will be calculated at multiple points and compared to this threshold. If higher than the threshold of 100 kPa that location will be considered "fractured". These so-called fractured locations will then be investigated further regarding crack propagation and crack depth.

4.3.3 Crack Propagation

Once failure of the icy shell is present these cracks must then propagate further through the ice shell. The fracture toughness of a material indicates how well a material resists crack propagation due to stress. Through tidal stresses work is available which, if large enough, is able to overcome the ice's fracture toughness. The corresponding minimum tensile stress σ_{min} for this to occur and result in crack propagation is given by Equation 4.2 [Porco et al., 2014], where g is the gravitational acceleration, $\Delta\rho$ is the density difference between water and ice and K is the fracture toughness of ice, which is 10^5 Pa $m^{1/2}$ [Porco et al., 2014].

$$\sigma_{min} = \frac{6}{4^{2/3}} \left(\frac{K}{\pi}\right)^{2/3} (g\Delta\rho)^{1/3} \tag{4.2}$$

The difference in density between water and ice-I is equal to 63 kg m^{-3} (see Table 2.3). The minimum required stress for crack propagation is 11.34 kPa, 11.45 kPa and 11.54 kPa for the maximum, high-end average and low-end average cases respectively where the difference is due to the different gravitational acceleration of each case. For all three simulated cases this is well below the required failure threshold. It can therefore be concluded that crack propagation will definitively happen in those locations where failure occurs.

4.3.4 Crack Depth

Th cracks must then propagate deep enough as to reach from the surface down to the liquid reservoir in order to meet the third condition for existence. In the case that the liquid reservoir is a subsurface ocean, as is the case with an icy Io, the crack length then must be longer than the thickness of the icy shell. The theoretically maximum depth to which a crack can propagate is the depth at which the stress at the tip of the crack becomes larger than the internal pressure [Manga and Wang, 2007]. The maximum

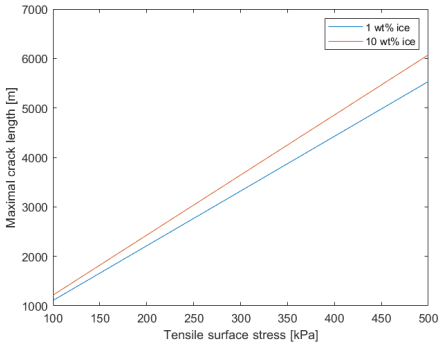

Figure 4.1: Maximum crack depth within a fractured ice shell as a function of the magnitude of surface stress. Two example cases are shown here for the case where the mass of the H_2O-layer is equal to 1% of Io's present-day mass and one where it is equal to 10%.

crack length l_{max} can then be determined with Equation 4.3 [Porco et al., 2014]. The corresponding maximum crack length for different surface stresses can be seen in Figure 4.1 which indicates that the maximum crack depth is at least 1000m for surface stresses larger than the adopted failure threshold of 100 kPa.

$$l_{max} = \frac{\sigma\pi}{2g\Delta\rho} \tag{4.3}$$

By calculating the surface stress and applying the failure threshold of 100 kPa it is possible to determine where the icy shell is fractured. Remember that for the simulated cases the minimum stress required for crack propagation is always less than the failure threshold thus it is not necessary to check for crack propagation. After identifying the fractured locations the maximum crack length at each of them can be determined using Equation 4.3. If this value exceeds the thickness of the icy shell that particular location is then assumed to have an active geyser.

4.4 Parameterizing Enceladus' Cryovolcanism

As mentioned in Section 4.1 the geysers of icy Io will be modeled on those of Enceladus. It is therefore necessary to understand Enceladus' geysers in order to determine their applicability to icy Io. The focus will be laid on Enceladus' South Polar Terrain as that is where the Tiger Stripes and geysers are located [Spencer and Nimmo, 2013]. Enceladus' South Polar Terrain is discussed in Section 4.4.1. The key parameters that will determine the applicability are the similarities between the interior structures of Enceladus and icy Io and the amount of tidally generated surface stress, as that is the main driver behind the existence of cracks and geysers. The comparison can be found in Section 4.4.2. The three parameters that describe the amount of geyser activity are the geyser production rate, eruption velocity and velocity distribution. These three parameters are discussed in Sections 4.4.3, 4.4.4 and 4.4.5 respectively.

4.4.1 Enceladus' South Polar Terrain

Indications of geyser activity have been observed on multiple icy moons. NASA's Voyager-2 mission for example took images of Neptune's moon Triton on which the presence of four plumes was captured [Soderblom et al., 1990] and could be the result of geyser activity [McKinnon and Kirk, 2014]. Roth et al. [2014] propose that observation by the Hubble Space Telescope of surplus hydrogen and oxygen indicate the presence of water vapor plumes on Europa. During their search for water vapor on Europa Paganini et al. [2020] only detected water vapor in Europa's atmosphere on one of the seventeen flybys. This could be due to the fact that geyser activity on Europa is very small or only occurs periodically. A better understanding of geysers on icy moons can be realised by looking at the geysers of Saturn's moon Enceladus. They are an excellent source of information as they have been studied and modeled extensively (see for example Ingersoll and Ewald [2011], Nimmo et al. [2014], Porco et al. [2014] and Yeoh

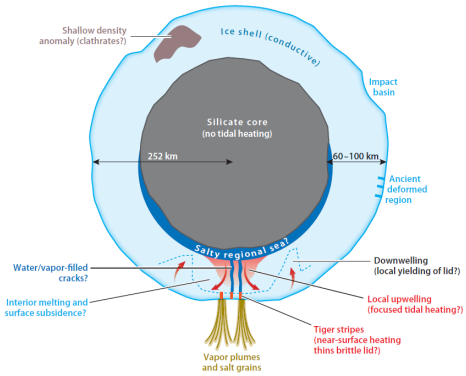

Figure 4.2: A possible interior structure of Enceladus [Spencer and Nimmo, 2013]. Note that a regional subsurface sea is depicted here but at present it is widely accepted that Enceladus has a global subsurface ocean [Thomas et al., 2016].

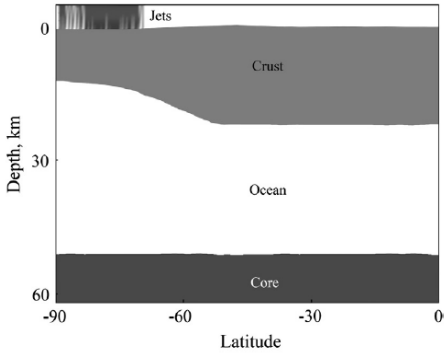

Figure 4.3: A schematic representation of the variable ice shell thickness of Enceladus [Thomas et al., 2016]. The SPT lies between latitudes of about 55° and 90° south (here given as negative values) [Spencer et al., 2009]. The icy shell (termed crust in the figure) is significantly thinner in this SPT than toward the equator resulting in the presence of geyser jets.

et al. [2015]).

Enceladus is a small moon orbiting Saturn with a mean radius of about 252 km [Porco et al., 2014]. The interior structure of Enceladus is uncertain [Rhoden et al., 2020] but if it is fully differentiated it consists of a silicate core with an overlying H_2O layer, which is thought to be partly liquid in the form of a global subsurface ocean [Thomas et al., 2016], [Rhoden et al., 2020]. A possible interior structure can be seen in Figure 4.2. In the above representation the silicate core has a radius of 152 - 192 km and the H_2O layer has a radius of 60 - 100 km [Spencer and Nimmo, 2013]. Other estimates are 150 - 170 km for the for the core and 80 - 100 km for the H_2O layer [Schubert et al., 2007] and 191 - 205 km for the silicate core and 47 - 61 km for the H_2O layer [Nimmo and Porco, 2014]. According to Thomas et al. [2016] the average thickness of the ice shell is thought to be about 21 - 26 km but with relatively large variations. This result was obtained by using data from observed librations of Enceladus. It is thought that the thickness of the ice shell is thinner underneath the South Polar Terrain, possibly 8 - 13 km thinner [Thomas et al., 2016]. A schematic representation of this thinner ice shell beneath the South Polar Terrain is given in Figure 4.3. The difference in ice shell thickness between the south and north pole has been suggested as the reason why the south pole is geologically active and the north pole is not [Rhoden et al., 2020]. Beuthe et al. [2016] used an isostacy model for Enceladus which suggested an ice shell thickness of about 7 ± 4 km underneath the South Polar Terrain. Even though the different models and studies mentioned above estimate different thicknesses for the thickness of Enceladus' ice shell what they do agree on is that the thickness of the ice shell is thinner at the south pole [Rhoden et al., 2020].

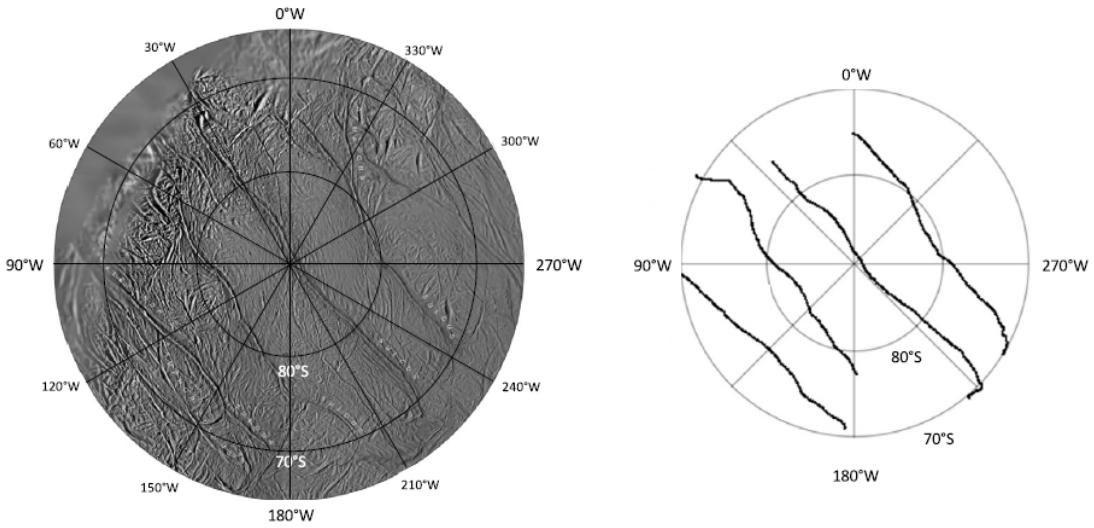

Figure 4.4: **Left** Image of Enceladus' SPT with the Tiger Stripes. **Right** Locations of simulated points on the Tiger Stripes [Rhoden et al., 2020]

The ongoing geyser activity on Enceladus was first detected by the Cassini-Huygens probe during its multiple flybys of Enceladus [Spencer et al., 2006]. The Imaging Science Subsystem (ISS) took several images of the South Polar Terrain (SPT) [Porco et al., 2006]. Analysis of these images led to the conclusion that the SPT is a geologically active area in which multiple narrow jets of icy particles contribute to the presence of a large plume. These jets emanate from fractures, most notably from the four "Tiger Stripes". They are four roughly parallel cracks that are about 130 km in length, 2 km wide and 500 m deep [Spencer et al., 2009]. Cassini's Composite Infrared Spectrometer (CIRS) observed that the SPT is abnormally warm. These abnormal thermal emissions also originate from the Tiger Stripes [Porco et al., 2006]. Figure 4.4 shows the South Polar Terrain of Enceladus. The SPT is a roughly circular area within 55 °S latitude and is ringed by large icy mountains [Spencer et al., 2009]. The four Tiger Stripes can also be seen as roughly parallel lines in Figure 4.4.

Enceladus' plumes are composed of about 90% H_2O [Waite et al., 2006] which is primarily in the form of water vapor and some tiny ice grains [Yeoh et al., 2015]. The source of the water in the plumes is a liquid water reservoir from which water evaporates and is accelerated though nozzle-like cracks Hansen et al. [2008]. Part of the fractures from which geysers erupt are called vents, which eject material at subsonic speeds and the others are called jets which eject material at supersonic speeds of up to Mach 5 - 8 Hansen et al. [2011]. Only a small fraction of the total amount of cracks are able to create such supersonic jets as only about 3.4% of the total molecules in Enceladus' plume originate from these jets [Hansen et al., 2011]. One possible explanation could be the periodic opening and closing of these cracks. According to Hurford et al. [2007] the surface of Enceladus experiences both tensile and compressive normal stresses depending on Enceladus' position along the orbit. While under compression the cracks are held closed and conversely while under tension they are held open. In between tensile and compressive stresses the crack widths on Enceladus may change by up to 0.5 m [Nakajima and Ingersoll, 2016]. During this periodic deformation it is plausible that a few of the many cracks have exactly the right shape to form supersonic nozzles while the many others do not. This could then explain why there are much more vents with lower eruption velocities than high-velocity jets [Hansen et al., 2011].

4.4.2 Applying Enceladus' Cryovolcanism to Io

In order to parameterize Enceladus' geyser activity, apply it to the case of an icy Io and critically evaluate this assumption the characteristics of Enceladus' H_2O-layer must be compared to that of icy Io. As described in Section 4.4.1 Enceladus' H_2O-layer consists of a global subsurface ocean with an icy shell on top, similar to the internal structure of icy Io's H_2O-layer as described in Section 2.3. Enceladus is

thought to have a global subsurface ocean [Thomas et al., 2016] as do the three simulated cases over the duration of their lifetime (see Section 6.2 for more information). The difference between the two internal structures is that the thickness of Enceladus' icy shell at the south pole is much thicker. Whereas the estimates for Enceladus range from 3 to 18 km (see Section 4.4.1 for more details), the thickness of icy Io's ice shell for the three simulated cases is never more than 350 m (again see Section 6.2 for more information). As a thinner ice shell requires less surface stress for cracks to propagate from the surface to the subsurface ocean this could lead to more fracture within Io's ice shell than within Enceladus'. Regarding the interior structure of the H_2O-layer one can then conclude that those of Enceladus and icy Io are similar.

Rhoden et al. [2020] calculated the surface stress for multiple interiors of Enceladus. The model they used, as the model used in this work, requires a uniform thicknesses for each layer. It is therefore not possible to include the latitudinal variations of Enceladus' ice shell thickness. Therefore the authors assumed that adopting a thin ice shell thickness will simulate the conditions of the South Polar Terrain and adopting a thicker ice shell will simulate the conditions at the north pole. As the ice shell thicknesses for the three simulated cases are very thin the focus will thus be on thinner models of Rhoden et al. [2020] with thicknesses of less than 5 km. The interior models of their different cases with a thin ice shell are given in Table 4.1, together with the maximum surface stress that was calculated by Rhoden et al. [2020] and the maximum stress calculated with the model used in this work. Before the results

Table 4.1: Different cases modeled by Rhoden et al. [2020], their maximum surface stress and the calculated values

Total shell thickness [km]	Ductile layer viscosity [Pa s]	Brittle layer thickness [km]	Maximal stress [kPa]	
			From Rhoden et al. [2020]	Calculated values
5	1E13	0.5	187 - 221	5 - 228
3	1E13	0.3	237 - 279	7 - 302
1	1E19	0.1	170 - 200	4 - 186
1	1E15	0.1	329 - 386	4 - 187
1	1E13	0.1	329 - 386	9 - 424
0.5	1E19	0.05	234 - 275	6 - 270
0.5	1E15	0.05	349 - 409	6 - 272
0.5	1E13	0.05	349 - 410	10 - 462

of Table 4.1 are discussed the difference in measuring points must be addressed. Rhoden et al. [2020] measured the surface stress in 2395 points which were all located in the Tiger Stripes whereas the model used in this work calculated the surface stress in 980 points across the whole South Polar Terrain. This is a result of the total amount of points at which the surface stress is calculated. A sensitivity test was done on the effect of the number of points where the surface stress is calculated on the eruptive area and computational time. This test is describe in Appendix C.4 and the results indicate that using 70 points along the longitude and latitude gave the best balance between accuracy and computational time. These 4900 points are distributed across the whole surface and 980 of these were located in the SPT. Some of these points will coincide with points within the Tiger Stripes but most of them will not. The last column of Table 4.1 holds two values, the first one give the lowest maximum surface stress experienced at these points and the second value gives the highest maximum surface stress. The maximum values are in the same range as that given by Rhoden et al. [2020]. The fraction of points which fulfilled each criteria mentioned in Section 4.3 is between 85 and 97%. This indicates that most of the South Polar Terrain has the possibility of being fractured and showing geyser activity according to the simple conditions for existence used here. This is in contrast to the observation that geyser activity is limited to the Tiger Stripes. Possible explanations are that these criteria are too simplistic, that crack propagation may be limited to areas that experience failure first and that the Tiger Stripes correspond to the areas that failed first which relieved some of the surface stress thus inhibiting further failure [Rhoden et al., 2020] or that some other mechanism than surface stress is involved. Further studies have to be performed to shed more

light on the issue. Here the assumption will be made that an area over which most locations are able to have geyser activity according to the criteria defined in Section 4.3 there will be several large faults such as Enceladus' Tiger Stripes. Starting from this assumption it is then possible to parameterize Enceladus' mass production rate and upscale it to an icy Io. It must be noted that the model of icy Io used in this work does not include a density difference between water and ice. The models of Rhoden et al. [2020] do include this difference and for the purpose of recreating those results this density difference was also included here. Beuthe [2018] indicates that differences in density contrast between the ocean and ice do not influence the amount of tidal stress significantly. Thus the conclusions made above can still be used for this work where the density of the H_2O-layer is assumed constant.

4.4.3 Production Rate

Two of Cassini's instruments that have contributed immensely to the estimates of Enceladus' mass eruption rate are the Ultraviolet Imaging Spectograph (UVIS) and the Ion and Neutral Mass Spectrometer (INMS). The UVIS instrument obtained its data thropugh observing stellar occultations in 2005, 2007 [Spencer et al., 2009] and 2010 [Hansen et al., 2011]. The INMS instrument obtained its data through several flybys, or encounters, of Enceladus' plume [Spencer et al., 2009]. The E2 encounter happened in 2005 [Smith et al., 2010], the E3 encounter in March of 2008, the E5 encounter in October 2008 and the E7 encounter in November 2009 [Dong et al., 2011]. These three encounters are specifically mentioned because the data obtained from them has been used regularly in studies estimating the eruption rate and velocities on Enceladus. The results of several of these studies are described below.

Eruption rate estimations of Smith et al. [2010] differ significantly for these encounters. The authors modeled plume formation by ejecting test particles from the surface with initial conditions provided by a Monte Carlo simulation. The authors then searched for source rates and eruption velocities that would best fit the plume density distributions obtained from INMS data. For all encounters the best fit was obtained for plume bulk velocities of 720 m/s. The best fit production rates are about 12 kg/s, 190 kg/s and 750 kg/s for the E2, E3 and E5 encounters respectively. According to the authors, the low value for the E2 encounter could be due to an underestimation as more recent data processing techniques that were applied to the data of the E3 and E5 encounter by Teolis et al. [2010] resulted in larger plume densities. But even if this were accounted for the resulting eruption rate would be on the order of 12-36 kg/s, which is still much lower than other estimates such as those of Smith et al. [2010]. The significant difference between the sources rates of the E3 and E5 encounters indicate that the source rate is variable in time by a factor of 4. Dong et al. [2011] created an analytical physical model of the outflow of one discrete source and then generalized this to a model with multiple sources. The authors compared predictions from their model with INMS data of the E2, E3 and E5 encounters as did Smith et al. [2010]. In addition Dong et al. [2011] also used data from the E7 encounter. Just as Smith et al. [2010] does, Dong et al. [2011] mentions that the results fitting the E2 data might be incorrect. Because Cassini's trajectory did not probe the plume the results might be an underestimation. The best fit results for the E3, E5 and E7 encounters estimates source rates of about 500 kg/s for the E3 and E7 encounters and 1000 kg/s for the E5 encounter. Best-fit bulk eruption velocities are in the range of 550 - 750 m/s.

Hansen et al. [2006] used Cassini's UVIS data from the 2005 occultation of the star γ Orionis by the Enceladus plume to determine what eruption rate would give the observed plume. Under the assumption that the temperature is 145 K the eruption rate would be 150 kg/s. The authors note that data from Cassini's Composite Infrared Spectrometer could suggest that the temperature could be as high as 180 K, which would indicate an eruption rate of 350 kg/s. The same method was used with data coming from a second occultation of γ Orionis in 2007. This time the eruption rate was estimated at 200 kg/s [Hansen et al., 2008]. In 2010 Cassini observed the Sun being occulted by the Enceladus plume [Hansen et al., 2011]. Using UVIS data Hansen et al. [2011] estimated the eruption rate to be $\sim$ 180 kg/s. Combining these results with the results of the occultations in 2005 [Hansen et al., 2006], 2007 [Hansen et al., 2008] and a standard deviation of 30 kg/s [Hansen et al., 2011] provides a best estimate of water vapor flux of 200 kg/s. Of this flux the authors estimate that about 15 - 25 % is ejected by the high-density jets and the rest is ejected more slowly along the length of the fissures.
Using a different approach than [Hansen et al., 2006], Tian et al. [2007] used a Monte Carlo simulation to try and simulate Enceladus' plume as observed by UVIS during the 2005 stellar occultation. In the

simulation the water molecules in the plume were represented by 10,000 test particles. The authors conclude that the simulations that best fit the observed plume had a production rate of 120 - 180 kg/s. Tenishev et al. [2010] used both UVIS data of the E2 encounter and INMS data of the E3 and E5 encounters. The authors used a semi-analytical model to determine parameters of eight distinct sources (determined by Spitale and Porco [2007]) that would best fit the observations mentioned above. An interesting conclusion of their study is that gravity does not need to be included when calculating the density profile of the southern hemisphere. Their results give an upper estimate for the production rate of $8\tilde{0}0$ kg/s with a bulk plume velocity between 520 and 700 m/s. All studies mentioned above focused on the production rate of vapor molecules. In contrast, Ingersoll and Ewald [2011] used data from Cassini's Imaging Science Subsystem (ISS), which measures the brightness of icy grains in the plume. Their results give an estimated icy grain source rate of $51\pm$ 18 kg/s for an exponential distribution and an estimated source rate of 38 ± 13 kg/s for a Lorentzian distribution (see Section 4.4.5 for more information).

A striking trend that can be seen from the results above is that using only UVIS data results in much lower source rates than using only INMS data or a combination of the two (see Table 4.2 for an overview).

Table 4.2: Source rate and eruption velocity estimates

Study	Instrument		Source rate	Vapor eruption
	UVIS	INMS	[kg/s]	velocity [m/s]
Hansen et al. [2006]	X		150 - 300	620
Hansen et al. [2011]	X		200	> 450
Tian et al. [2007]	X		120 - 180	350 - 500
Tenishev et al. [2010]	X	X	800	520 - 700
Smith et al. [2010]		X	190 - 750	720
Dong et al. [2011]		X	450 - 1050	550 - 750

As can be seen in Table 4.2, there is a huge difference in estimated values for the source rates. There are several reasons as to why the estimates can be so different. First of all data from different observations and different instruments (Cassini's UVIS and INMS) is used. The fact that the estimated eruption rate depends on the time of observation suggests that the eruption rate is variable over time which, according to Smith et al. [2010], could be by a factor of 4. A second reason for the differing estimates could be based on the interpretation of the source of observed molecules Smith et al. [2010]. If all observed molecules are assumed to be recent then a high eruption rate is required to provide the observed densities. If, however, some molecules are assumed to be long-lived and part of the background neutral torus they should not be considered as freshly ejected. Smith et al. [2010] argue that this is the case for the E2 encounter and that consequently these molecules should be omitted when estimating the plume density. Therefore the authors argue that their lower estimate for the eruption rate is correct and that other studies overestimate the eruption rate. Furthermore it is striking that the estimates of analytical models such as those of Tenishev et al. [2010] and Dong et al. [2011] are generally much higher than those of computational models, such as those of Tian et al. [2007] and Smith et al. [2010]. As previously stated the maximum estimates are much higher for studies which use the INMS data. These studies all included the E5 encounter which suggests an increase of source rate by a factor of 4 compared to the E3 encounter [Smith et al., 2010]. This increase in estimated source rate could then be due to an actual increase in production rate or due to the fact that INMS data was used. Burger et al. [2007] also used INMS data but only of the E2 encounter. The authors estimated source rates of about 300 kg/s which is higher that that estimated by Hansen et al. [2006], Hansen et al. [2011] and Tian et al. [2007], suggesting the INMS instrument was the reason for increased estimated source rates. However their study was performed before the work of Teolis et al. [2010] which means that the results of Burger et al. [2007] could be an overestimation. This is because water molecules temporarily stuck to the antechamber of the INMS instrument. The works of Smith et al. [2010], Dong et al. [2011] and Tenishev et al. [2010] used INMS data that was treated by a "sticking model" created by Teolis et al. [2010] that accounted for this phenomenon. The result being that the observed amount of water molecules was reduced. It is unclear if Burger et al. [2007] would reach an estimated source rate

closer to that suggested by the work using UVIS data by using treated data. Therefore it is more likely that the increased source estimates are due to the temporary increase in source rate observed during the E5 encounter. Unfortunately it is unclear if such an increase is a common or a rare occurrence and how long it lasted. One can conclude that there are several possible reasons as to the difference between the different estimates but that it is not clear which estimates represent an averaged value. The range of production rates lies between 150 and 1050 kg s−1 and this will be reflected in the estimates used for the three cases (see Section 5.4). The maximum case will use a water vapor production rate of 700 kg s^{-1} which is similar to the maximum estimates of Tenishev et al. [2010] and Smith et al. [2010]. The two average cases will use a production rate of 200 kg s^{-1} for the water vapor molecules which is close to the minimum estimate of Smith et al. [2010] and the average of the values estimated by Hansen et al. [2006] and Hansen et al. [2011]. The production rate of the icy grains depends on the distribution velocity. This is discussed in Section 4.4.5.

The three cases studied by Rhoden et al. [2020] with the thinnest ice shell are given in the last three rows of Table 4.1. The ice shell thicknesses of the three simulated cases in this work on the same order of magnitude (see Section 6.2). In these cases more than 93% of the points or almost the whole area of the South Polar Terrain fits the requirements for the existence of geysers. Thus one can parameterize the mass production rate of the SPT as follows.

$$\dot{m}_{par} = \frac{\dot{m}_E}{A_{SPT}} \tag{4.4}$$

Where $\dot{m}_{par}$ is the parameterized mass production rate in kg s^{-1} m^{-2}, $\dot{m}_E$ is the mass production rate of the SPT and A_{SPT} is the area of the South Polar Terrain. The SPT can be seen as a spherical cap that ranges from the south pole to about 55°S latitude [Spencer et al., 2009]. Thus for a radius of 252 km [Porco et al., 2014] this results in a surface area for the SPT of about 7.2E10 m^2 or about 7.2E4 km^2, which is close to the value given by Porco et al. [2006]. Together with the estimated production rate Equation 4.4 will give the parameterized production rate for Enceladus' SPT.

4.4.4 Eruption Velocity

Note that the eruption velocities mentioned below are considered the bulk velocities of the plume. They represent the average velocity of the water vapor molecules or of the icy grains. The velocities of individual molecules or grains will differ from these bulk velocities according to a certain distribution. These velocity distributions are discussed in Section 4.4.5. Table 4.2 provides a summary of the estimates discussed below.

Smith et al. [2010] used a Monte Carlo simulation to determine the plume velocity. The authors' objective was to simulate the plumes observed by Cassini during its E2, E3 and E5 encounters with Enceladus. The source of their data is Cassini's Ion and Neutral Mass Spectometer (INMS). Their simulations result in an estimated bulk flow velocity of about 720 m/s for all three encounters, which was about 1.8 times the thermal velocity. The thermal velocity of a gas is a measure of the velocity of a particle due to its temperature and is given by $v_{th} = \sqrt{2kT/m}$ with k is Boltzmann's constant, T is the temperature of the particle and m is its mass [Dong et al., 2011]. The thermal velocity follows directly from the temperature of the ejected particles. In their study, Dong et al. [2011] also used data from Cassini's INMS to estimate plume characteristics. The authors tried to simulate the plume as measured in the E3, E5 and E7 encounters. The model, which uses multiple sources of water vapor, estimate flow velocities to be about 550 - 750 m/s while Tenishev et al. [2010] estimated the eruption velocity to be between 520 and 700 m/s, depending on the jet that was simulated. In their study Hansen et al. [2008] reported vertical velocities in the plume to be $\sim$ 1.5 times the thermal velocity. Under the assumption of a temperature of 145 K [Hansen et al., 2006] the thermal velocity is 412 m/s which would give an eruption velocity of $\sim$ 620 m/s. Hansen et al. [2011] estimate that the high-density jets have high Mach numbers in the range of 5 - 8. This indicates eruption velocities upwards of 1 km/s to an upper limit of 2 km/s. As the authors estimate that only about 3.4% of the molecules in the plumes come from the jets it would seem more realistic to adopt a lower value for the averaged eruption velocity of the whole plume. In their work Tian et al. [2007] obtained the best results when the eruption velocities were between 350 and 500 m/s.

All velocities mentioned above are that of the water vapor molecules. The estimated eruption velocity of grains was estimated by Hedman et al. [2009] to be between 80 and 160 m/s, based on Cassini's Visual

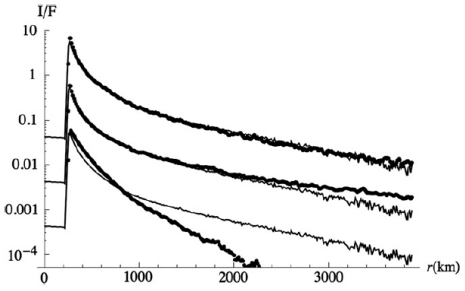

Figure 4.5: Observed and simulate plume brightness with respect to height above the surface [Ingersoll and Ewald, 2011]. The observed brightness is given by thin lines and the calculated brightness by the thick lines. The brightness was calculated using, from top to bottom, an exponential, Lorentzian and Gaussian velocity distribution of the erupted icy grains. For clarity the both the observed and calculated brightness was multiplied by 100, 10 and 1 from top to bottom respectively.

and Infrared Mapping Spectrometer (VIMS) instrument. The estimates of Brilliantov et al. [2008] and Ingersoll and Ewald [2011] are close to the minimum value given by Hedman et al. [2009], with grain velocities of range of 100 m/s and 90 m/s respectively. An overview of the different estimates for the eruption velocity is given in Table 4.2.

The spread of the eruption velocity is much less than that of the production rate. Therefore the values used for the three cases lie much closer to each other. For the maximum case the eruption velocity of the water vapor molecules out of the vents was set at 750 m s^{-1} and at at 450 m s^{-1} for the two average cases. The velocity for those vapor molecules that are erupted from the jets is set at 1 km s^{-1} for all three cases. Lastly the eruption velocity of the grains is set at 100 m s^{-1} for all three cases.

4.4.5 Velocity Distribution

The eruption velocities mentioned in Section 4.4.4 are estimates of the average eruption velocity for the entire plume. Individual molecules will have a different eruption velocities than these average values. Ingersoll and Ewald [2011] tried to obtain a reasonable estimate for the total amount of ice particles in the Enceladus plume. In their work the authors simulated particles being ejected from the Tiger Stripes. Multiple simulations were performed with different velocity distributions for the particles, namely Lorentzian, Gaussian and exponential distributions. The authors then determined the brightness of these simulated plumes and compared it to the brightness of the observes plume of Enceladus. The result of their work can be seen in Figure 4.5. The thin lines are the observed plume brightness with radial distance from the surface of Enceladus. The observed values are plotted three times on order to compare them with each velocity distribution. For clarity they are multiplied by 100, 10 and 1 from top to bottom respectively. The bold lines are the simulated values and are, from top to bottom, the results of the exponential, Lorentzian and Gaussian velocity distribution respectively. It is clear that the exponential distribution fits the observed data for all ranges. The best fit vent production rate for an exponential velocity distribution is 51±18 kg/s which corresponds to an escape rate of 4.6 kg/s or about 10%. Bierson and Steinbrügge [2021] noted that similar mass loss rated to those of [Ingersoll and Ewald, 2011] are obtained by simply integrating the velocity distribution above the escape velocity and considering those particles to be lost. The escape velocity is defined as the velocity required for a particle on the surface of a body to obtain an infinite semi-major axis and is given by $V_e = \sqrt{2GM/R}$ where G is the gravitational constant, M is the mass of the body and R is the surface radius [Wertz, 2001]. A particle at escape velocity is then considered to be lost to the body and will not be able to return. In this work the approach of Bierson and Steinbrügge [2021] together with the method of Ingersoll and Ewald [2011] will be used. The exponential and Lorentzian velocity distributions are given by Equations 4.5 and 4.6 respectively [Ingersoll and Ewald, 2011].

$$p(v) = \frac{1}{v_0} \exp\left(-\frac{v}{v_0}\right) \tag{4.5}$$

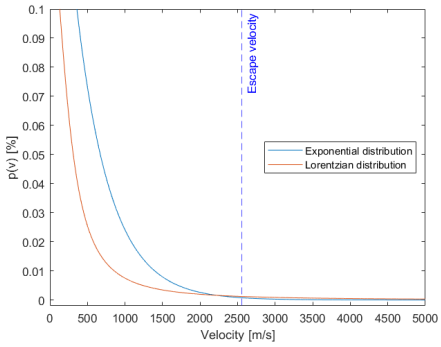

Figure 4.6: The probability density function for an exponential and Lorentzian distribution of erupted water vapor molecules. The chosen parameters are those of the low-end average case. Only a very small fraction of the material erupts at velocities higher than the escape velocity and is able to escape.

$$p(v) = \frac{2v_0}{\pi} \frac{1}{v_0^2 + v^2} \tag{4.6}$$

Where v_0 is the characteristic bulk eruption velocity and v is the actual eruption velocity according to the respective distribution. With the notations in Equations 4.5 and 4.6 the distribution is normalized so that the integral from zero to infinity is equal to 1 [Ingersoll and Ewald, 2011]. An example probability density function for an exponential and Lorentzian distribution can be seen in Figure 4.6. This example shows the velocity distribution of the erupted vapor molecules corresponding to the low-end average case. As such the bulk eruption velocity is 450 m/s and the escape velocity is 2557.4 m/s. It is clear that only a very low fraction of the erupted vapor molecules have a velocity larger than the escape velocity and can therefore escape from icy Io.

To determine the amount of particles with a velocity higher than the escape velocity v_{esc} the probability becomes $p(v_{esc} \leq v < \text{inf})$. Integrating Equations 4.5 and 4.6 gives the following results (see Appendix A.4 for the detailed calculations).

$$p(v_{esc} \leq v < \infty) = \exp\left(-\frac{v_{esc}}{v_0}\right) \tag{4.7}$$

$$p(v_{esc} \leq v < \infty) = 1 - \frac{2}{\pi} \arctan \frac{v_{esc}}{v_0} \tag{4.8}$$

By choosing a characteristic bulk eruption velocity and either the exponential distribution (given by Equation 4.7) or the Lorentzian distribution (given by Equation 4.8) and using the escape velocity it can be determined what percentage of erupted particles are lost. It must be noted that Ingersoll and Ewald [2011] obtained the above results by looking at icy particles and not at vapor molecule. Here the assumption will be made that these results can also be applied to the eruption of vapor molecules. As an example, Table 4.3 gives an idea of how much mass is lost, depending on the velocity distribution. The set-up of this example is as follows. The total mass ejected in to the plume comes from vents with low eruption velocities and jets with high eruption velocities. Hansen et al. [2011] estimates that about 15-25% of the total water vapor flux is ejected from these jets. Here an average ratio of 20 % is used. Because the eruption velocity of the jets is higher than that of the vents material that erupts from these jets will have a higher chance of escaping than material that erupts from the vents. However it is still necessary to include the material that erupts from the vents as the bulk of the material, 80%, comes from those vents and because of the velocity distribution a fraction of the erupted material will still escape, albeit less than the material coming out of the jets. The bulk eruption velocity of the icy grains is set at 100 m/s, which is consistent with the findings of Brilliantov et al. [2008], Hedman et al. [2009] and Ingersoll and Ewald [2011]. In their work the authors did not consider these high-velocity jets but only the lower eruption velocities of the vents. In this work this eruption velocity of 100 m/s is adopted for both the icy grains coming from the vents as those coming from the jets. Even though it is probable that the icy grains erupt

from the jets at a higher velocity through interaction with the fast-moving vapor molecules, adopting a higher eruption velocity has a negligible impact on the total escape rate. For example if the eruption velocity of the icy grains coming out of the jets is increased from 100 m/s to 500 m/s the fraction that is lost only increases by 0.024% (see Appendix A.4 for more details). As it is unknown how much the velocity actually increases and its influence is not significant anyway it will not be included here. The eruption velocity of the vapor molecules coming from the jets is set at 1600 m/s [Hansen et al., 2011] and for the vapor molecules coming from the vents two cases are considered: in the first case the bulk eruption velocity is set at 450 m/s and at 750 m/s for the second case. Lastly the ice-vapor ratio is set at 0.25. For more details about the calculation, see Appendix A.4. The percentage of erupted material that is lost for the different cases described above is given in Table 4.3 The results of Table E.2 confirm the

	Percentage that is lost with an eruption velocity of	
Velocity distribution	450 m/s	750 m/s
Exponential	3.455	5.354
Lorentzian	13.292	17.819

Table 4.3: Mass fraction that is lost for an exponential and Lorentzian distribution

expectation that increasing the eruption velocity of the vent vapor molecules increases the amount of mass that is lost. The choice between an exponential and a Lorentzian distribution has a much bigger impact with an increase by a factor of 3-4 for the Lorentzian distribution compared to the exponential. As both distributions are possible options the exponential distribution will be used for the low-end average case and a Lorentzian distribution for the high-end average and maximum cases.

4.5 Icy Io's Geysers

4.5.1 Overview

A short summary of the way geyser activity is modeled will be given here. The complete geyser activity is provided by two types of cracks which are denoted as vents and jets. Both vapor molecules and icy grains erupt from these two types of cracks. The ice-to-vapor ratio is the same for both vents and jets and will depend on the specific case. The relative eruption rates of the two types is given by the jet-to-vent ratio which can be 0.2 or 0.25. The eruption velocity of the icy grains is the same for both types but that of the vapor molecules differs. The vents eject vapor molecules at a relatively low subsonic velocity whereas the jets eject vapor molecules at supersonic speeds. These eruption velocities are considered characteristic velocities and apply to the bulk ejected plumes. To determine the velocity of individual water molecules a velocity distribution is used. Lastly the total mass flow of all cracks is a function of the parameterized production rate of Enceladus. The ice-to-vapor and jet-to-vent ratios, the different eruption velocities, the velocity distribution and parameterized mass flow of Enceladus fully describe how the geyser activity of icy Io is modeled.

4.5.2 Icy Io's Mass Loss Rate

It is straightforward to upscale Enceladus' mass eruption rate per unit area to icy Io. Once Io's surface stress has been calculated each measurement point can be checked for the presence of geysers according to the criteria summed up in Section 4.3. The fraction of the points that meet these criteria and thus where the presence of geysers is possible ($f_{geysers}$) is then multiplied by the total surface area of icy Io A_{Io}. This area which could possibly have geysers is henceforth known as the eruptive area. The product of the eruptive area and Enceladus' mass eruption rate per unit area $\dot{m}_{par}$ gives the corresponding eruption rate for icy Io, $\dot{m}_{Io} = f_{geysers} \cdot A_{Io} \cdot \dot{m}_{par}$. The results for two example cases can be seen in Table 4.4. Case 1 has an amount of ice corresponding to 1 wt% and for case two this is 10 wt%. In this example the mass eruption rate per unit area for Enceladus is based on a total mass eruption rate of 250 kg s^{-1}, which is an average of the estimates given in Section 4.4.3. The simulated cases will have different estimated

eruption mass rates for Enceladus thus the results below are not representative of the simulated cases. The production rate of Io described above encompasses all ejected particles. Of these ejected particles only

Table 4.4: Mass eruption rate for two example cases of an icy Io

Case	$f_{geysers}$ [%]	Mass eruption rate [kg/s]
1, with 1 wt% ice	83.1	122.82E3
2, with 10 wt% ice	85.55	151.14E3

a fraction will actually escape completely while all other particles will fall back to the surface [Ingersoll and Ewald, 2011]. The material that falls back on to the planet is assumed to be reintegrated in to the H_2O-layer but the process by which this happens is not considered in this work. Once the eruption rate has been calculated and the escape rate is known the total mass escape rate can then be calculated.

4.6 Conclusion

The geysers on Enceladus are all located within the South Polar Terrain. Here the interior structure of Enceladus' H_2O-layer consists of an icy shell and a subsurface ocean underneath. Tidal stresses cause this ice shell to be fractured resulting in the four Tiger Stripes, which are the source of Enceladus' geyser activity. The cracks that form the Tiger Stripes run through the ice shell to the subsurface ocean which thus acts as the liquid reservoir for the geysers. This model of Enceladus' geysers was first proposed by Schmidt et al. [2008] and is adopted for icy Io's geysers. The geyser activity of Enceladus can be applied to Io because it has the same internal structure for its H_2O-layer, the surface stresses are of the same magnitude and the cracks are highly likely to extend through Io's ice shell because it is much thinner than that of Enceladus. The three conditions for the presence of geysers are the presence of an ice shell, the presence of a subsurface ocean underneath the ice shell and the presence of cracks that run through the ice shell connecting the surface with the subsurface ocean. At multiple points on Io's surface a check is done if these three criteria are met at those points. The eruptive area is then the fraction of the points that meet these three criteria. By multiplying the eruptive area by the parameterized production rate of Enceladus' geysers one is able to obtain the production rate of icy Io. The escape rate is the fraction of erupted material that exceeds the escape velocity. The escape rate depends on the production rate (which in turns depends on the jet-to-vent ratio), the eruption velocity and the velocity distribution and the three simulated cases have different values for each of these parameters which can be seen in Table 5.1.

Part II

Simulation, Results and Discussion

Chapter 5

Simulating Io's Ice Loss

5.1 Introduction

This chapter will discuss all aspects of the simulations. It will start of by explaining the general workflow of the code in Section 5.2. A flowchart of the code can be found there and can serve as a guideline for the rest of the chapter. After this some simulation specific design choices are given in Section 5.3. These design choices include the length of the time-step, which calculations were not required for every iteration and the value of several parameters and their influence on accuracy and computational time. The section will end by listing the criteria as to when a simulation ends and what is required to start a new iteration. This is followed by Section 5.4 where an overview is given of the different parameters that were simulated such as the eruption velocity, initial semi-major axis and the initial mass of each case's H_2O-layer. Lastly an overview is given in Section 5.5 of the three cases with a summary of the values of the simulated parameters for each case.

5.2 General Workflow

To determine how much ice an icy Io could have lost through tidal heating a model was created and a piece of code was written. With this code it is possible to simulate an icy Io's interior evolution with a prescribed migration model. This is done by first determining the internal structure and consequently calculating the ice loss rate for that internal structure. The code will repeat this until all ice is gone or the simulation is halted due to some predefined criteria. This section will describe the general workflow of the code and is intended to be used as road map throughout this work together with the schematic overview given in Figure 5.1. The text below will often make reference to certain blocks. Unless stated otherwise these blocks all refer to the flowchart given in Figure 5.1 to improve readability.

The code requires some user-defined inputs which are represented by the block "USER INPUT". These are the parameters of each case that is to be simulated. The required input are the initial amount of water, an initial estimate for the thickness of the icy shell, the production rate of Enceladus, the chosen velocity of the vapor and grains both out of the vents and the jets, the jet-to-vent ratio, the velocity distribution of the erupted material, the initial semi-major axis, the Jovian quality factor Q_J and the time-step of the simulation. The values for all these parameters for all three cases are summarized in Table 5.1.

The initial mass of water and the initial estimate for the thickness of the icy shell are used to determine the internal structure of icy Io. The internal structure function first assumes that the icy shell consists of a stagnant lid with a convective sublayer. The thickness of both of these is determined by assuming the heat flow through each layers is equal and that their sum equals the initial estimate mentioned above. Once a solution has been found the Rayleigh number of the corresponding icy shell structure is calculated in order to determine if convection is actually present in this structure. If so, the current internal structure is kept and if not the structure is changed in to a single conductive layer with a thickness equal to the initial estimate of the ice shell thickness. The thickness of the internal ocean is simply the difference between the thickness of the ice shell and that of the total H_2O-layer. Most of the parameters of the silicate mantle

and core are kept constant throughout the simulation except for the mantle temperature, viscosity and shear modulus as they affect the tidal heating rate. These parameters are determined by equating the heat flow out of the mantle to that through the icy shell. The function that calculates the internal structure is discussed in detail in Chapter 2 and is represented by the blocks "INTERNAL STRUCTURE" and "HEAT FLOW". The resulting complete internal structure (block "INTERNAL PARAMETERES") is then passed on towards the function that calculates the tidal heating (block "TIDAL HEATING").

The model uses the matrix propagator method as described by Jara-Orué and Vermeersen [2011] and Sabadini et al. [2016] to determine the internal radial functions. These radial functions are then used to calculate the internal dissipation according to the method described by Beuthe [2013]. Both of these methods are described in Chapter 3. At this point the heat flow calculated by the internal structure function is compared to the heat flow calculated by the tidal heating function (block "COMPARE"). If these values are sufficiently close to each other the internal structure is passed on to the function that calculates the surface stress (block "GEYSER ACTIVITY"). If not sufficiently close to each other the initial estimate of the thickness of the ice layer is adapted and used as a new input parameter (block "NEW ESTIMATE") depending on the difference between the two heat flows. The processes described above are then repeated until convergence. As of the second iteration the initial estimate is set to the actual thickness of the ice layer calculated during the previous run. As there is always a unique solution it does not matter what initial value is chosen but choosing one that is close to the previous value reduces the calculation time considerably. The details of this comparison can be found in Section 3.5.

The function that calculates the surface stress (block "GEYSER ACTIVITY") requires the longest computational time. To determine which points could experience geyser activity three criteria must be met. The surface stress must be large enough to allow for crack instigation, crack propagation and result in a maximum crack depth larger than the thickness of the icy shell [Porco et al., 2014]. Once the area that meets those criteria is known the parameterized eruption rate of Enceladus can be upscaled to icy Io and the resulting ice loss can be calculated (block "MASS LOSS"). The process by which the surface stress, geyser activity and corresponding mass loss is calculated can be found in Chapter 4.

At this point a check is done to see if the simulation has come to and end (block "END CHECK"). There are three possibilities (see Section 5.3.4 for more details): either all water has been removed from icy Io, or the surface stress has become too low to allow for geyser activity which means no more water will be lost, or the thickness of the ice shell required for an equilibrium solution is larger than the remaining thickness of the water layer. If any of these conditions are met the simulations end, otherwise the simulation starts the next iteration. In that case three input parameters mentioned above need to be adapted (block "UPDATED PARAMETERS"). First the mass of water left on icy Io is decreased by the amount that is lost over the last time-step. Second the tidal migration of icy Io is calculated resulting in a new value for the semi-major axis. Third the thickness of the ice shell is set as the new initial estimate for the next iteration, as mentioned above. The start of a new iteration is discussed in Section 5.3.5.

5.3 Simulation-specific Design Choices

This section will describe some simulation specific design-choices. First the time-step will be discussed followed by some selective calculations. After this the effect of some parameters on the accuracy and computational time is discussed. Lastly the simulation's end criteria and which parameters get updated between iterations are given.

5.3.1 Time-step

A major design choice for the simulation is the time time-step of each iteration. A smaller time-step will lead to increased computational times but will also offer increased accuracy. To determine the optimal time-step a sensitivity test was performed that investigated the influence of the time-step on the final semi-major axis and remaining mass of the H_2O-layer. The results of this test and a detailed discussion can be found in Appendix B.1. The main conclusion of this test was that a time-step of $4.59 \cdot 10^4$ years gave the best balance between accuracy and computational time. The final values for the semi-major axis

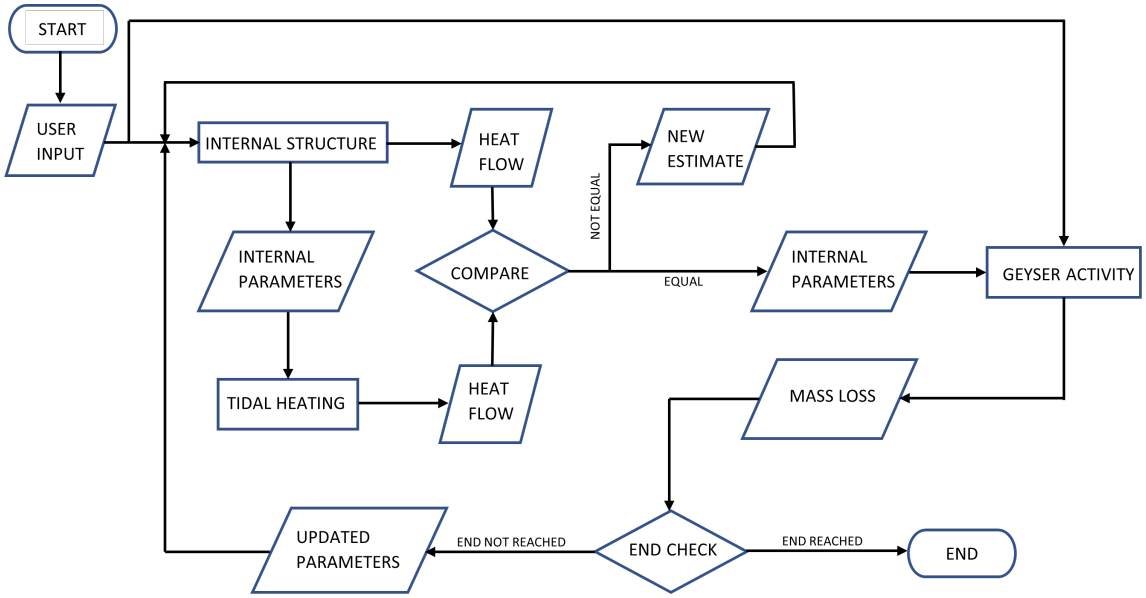

Figure 5.1: Flowchart for the code that performs the simulations. Rectangles indicate functions, parallelograms indicate input or output data and diamonds indicate decisions. Output of the decisions is written on the arrows leaving the diamonds.

and mass of the remaining H_2O-layer would not change significantly by decreasing the time-step even further whereas the computational time, which was already more than 4 hours, would become exorbitant.

5.3.2 Selected Calculations

The most lengthy calculation by far is that of the surface stress which takes up 75% of the computational time of a single calculation (see Appendix C.4 for more details). Therefore the performance of the code can be enhanced greatly by only calculating the surface stress every few iterations and using previous values for the intermediate iterations. A test was performed on the effect of calculating the surface stress every few calculations. The test is described in detail in Appendix B.2. The conclusion of this test is that calculating the surface stress once every 50 iterations will reduce the computational time by a factor of 4 while still giving accurate values for the final semi-major axis and remaining mass of the H_2O-layer. Decreasing the frequency by which the surface stress is calculated even more will reduce the accuracy of the result too much while not offering much gain in computational time. Therefore the frequency of calculation is set at once every 50 calculations.

5.3.3 Parameters Affecting Accuracy and Computational Time

Surface Stress Locations

The surface stress is only calculated at a certain number of points because, as mentioned above, this takes up a significant fraction of the computational time for one iteration. A sensitivity test was done on the required computational time and eruptive area based on the number of longitude and latitude points. The results of this test can be found in Appendix C.4. The main conclusion is that having more than 70 longitude and latitude points (resulting in a total of 4900 points) does not change the eruptive area and only increases the required computational time. Therefore the value of 70 points was chosen.

Initial Estimate for the Thickness of the Ice Shell

To determine the thickness of the sublayers within the icy shell (if present) Newton's root finding algorithm was used. How this was done is described in Section 2.3.4 and Appendix A.1. As mentioned there this root finding algorithm requires an initial guess. Appendix C.2 discusses two tests that were performed. The first describes the influence of two parameters: the initial guess and the change in initial estimate in

case no convergence is found. The test showed that the resulting ice shell thickness was not affected by the either of these parameters within the range that was tested. Newton's root finding algorithm works by calculating successive values of the root until the difference between two successive values is considered sufficiently small. This difference is called the convergence criterion and the influence of this criterion on the ice shell thickness is described by the second test of Appendix C.2. It showed that a convergence criterion of 1% was the best balance between accuracy and computational time.

Initial Estimate for the Mantle Temperature

The properties of the silicate mantle are determined so that the heat flow out of the mantle is equal to the heat flow through the icy shell. Section 2.4.2 describes how this is done. In summary it is an iterative process that starts with an initial estimate of the mantle temperature. Appendix C.3 describes the test that was done on the influence of this initial guess. The result is that for an initial estimate within the range that was tested its value does not influence the end result. The initial estimate was set equal to the average solidus temperature of the mantle. The heat flow out of the mantle and the heat flow through the icy shell were deemed sufficiently close if their difference was less than 1%. A more strict convergence criterion did not affect the obtained mantle temperature but in some cases this did not allow the algorithm to reach a convergence.

Convergence Criterion for the Equilibrium Solution

An equilibrium solution is reached when the heat flow through the icy shell is equal to the surface heat flow due to the tidal dissipation. Setting the convergence criterion to 1% resulted in the best balance between accuracy and computational time. The test is described in Section 3.5 and in Appendix C.1.

5.3.4 End Criteria

The simulation ends when one of the following three criteria is met:

- The H_2O-layer has been completely removed
- The eruptive area is equal to zero
- The ice shell thickness required for the equilibrium solution is larger than the total thickness of the H_2O-layer

The first criterion is checked by comparing the mass that is lost to the remaining mass of the H_2O-layer. If, over the course of the last time-step, more mass would be lost than that was left in the H_2O-layer the simulation is halted as the objective has been fulfilled. The second criterion happens when the surface stresses no longer reach the required failure threshold for crack instigation. In that case the eruptive area becomes zero and all geyser activity ceases. An example of this can be seen in Figure 3.3. The last criterion indicates that it is no longer possible to obtain an equilibrium solution. As discussed in Chapters 2 and 3 the equilibrium solution is obtained when heat flow through the icy shell is equal to the heat flow resulting from tidal dissipation (see Section 3.5 for more details). At a certain point the thickness of the ice shell that follows from the heat flow through it becomes larger than the thickness of the remaining H_2O-layer. An example can be seen in Figure 5.2 which shows the required thickness of the icy shell and the thickness of the remaining H_2O-layer for the high-end average case at the very end of the simulation. It shows that the simulation runs until these two parameters are almost equal and that if one more iteration were to be performed the required ice shell thickness would become larger than the thickness of the remaining H_2O-layer. This would be physically impossible meaning that the assumption of an equilibrium state is no longer applicable. It is possible that during the next time-step the last remaining part of the ocean would be ejected leaving behind a fully frozen H_2-O layer. If none of these end criteria are met a new iteration starts. This process is described in Section 5.3.5.

5.3.5 Starting a New Iteration

When a new iteration starts three parameters are updated: the initial estimate of the thickness of the ice shell, the mass of the H_2O-layer and the semi-major axis. The initial estimate of the thickness of the

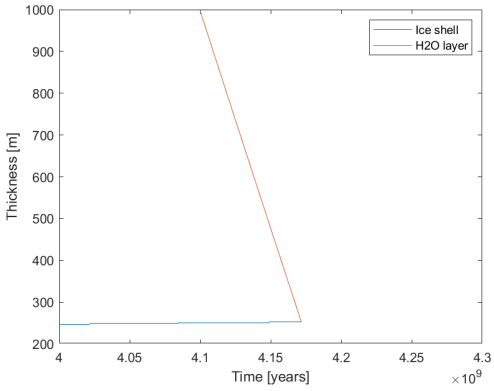

Figure 5.2: Caption

ice shell is set equal to the equilibrium value of the previous iteration. By doing this the computational time is reduced as the estimation will be very close to new equilibrium value requiring less iterations of Newton's root finding algorithm to determine the new equilibrium values. To determine the new mass of the H_2O-layer the amount of H_2O that is lost is simply subtracted from the previous iterations mass of the H_2O-layer. Due to tidal migration the semi-major axis changes every iteration. The change in semi-major axis is discussed in detail in Section 3.4. After updating the values of these three parameters a new iteration can be started.

5.4 Simulation Variables

The variables that will be simulated are all related to geysers. The geysers of Enceladus have been extensively studied (see Section 4.4 for more information) but a lot is still unknown. This gives rise to much uncertainty in the important aspects that are required to determine ice loss through geysers such as the production rate and eruption velocity. On the other hand this gives an excellent opportunity to investigate different cases and the possible range of mass loss through geysers. First two physical parameters are discussed: the production rate and the eruption velocity. After that three design options of the ice loss mechanism are presented: the velocity distribution, the jet-to-vent ration and the ice-to-vapor ratio.

Production Rate of Enceladus

The different estimated source rates of Enceladus have been discussed in Section 4.4.3. They cover a wide range of values, from 120 kg/s to 1050 kg/s (note that these values indicate the source rate of water vapor only). As discussed in Section 4.4.3 the maximum values given by Tenishev et al. [2010]. Smith et al. [2010] and Dong et al. [2011] could be in part due to a possibly temporary increase in production rate during the E5 encounter. Conversely it could also be that encounters E2 and E3, which suggest lower source rates, experienced a temporary decrease in production compared to the long-time average. To account for this uncertainty the production rate for the maximum case will be 700 kg/s which is lower than the maximum reported value. Consequently the the production rate for the average cases will be higher than than the lowest values reported and is set at 200 kg/s. Note that these are both source rates for water vapor only. The production rate of icy grains is discussed below. Even though the source rate is variable (see for exampleHurford et al. [2007], Smith et al. [2010] and Hedman et al. [2013]) it will be kept constant during the simulation. Adding a variation in time is beyond the scope of this work but could be an interesting follow-up.

Eruption Velocity

In contrast to the production rate there are different eruption velocities that must be used simultaneously. This is because there are two different sources and two different particles being erupted. The two sources are the vents and the jets, with slower eruption velocities for the vents and higher ones for the jets. From

both sources water vapor and icy grains are ejected. The eruption velocity of the icy grains is kept at 100 m/s for both sources and for all three cases (see Section 4.4.4 for more information). Increasing the eruption velocity of the icy grains in the jets does not significantly influence the escape rate, see Appendix A.4 for more information. The eruption velocity of the water vapor will depend on the source. For the jets this is set at 1600 m/s [Hansen et al., 2011] and also kept constant for all three cases. The water vapor eruption velocity will change for the different cases. The maximum case will use a velocity of 750 m/s while the average cases will use a velocity of 450 m/s.

Velocity Distribution

The choice of velocity distribution is a straightforward one. A Lorentzian distribution ensures a larger escape rate than an exponential one [Ingersoll and Ewald, 2011]. As can be seen in Table 4.3 the effect can be quite large. The maximum and the high-end average case will incorporate a Lorentzian distribution and the low-end average case an exponential one.

Jet-to-vent Ratio

As with the velocity distribution the choice of jet-to-vent ratio is also straightforward. According to Hansen et al. [2011] about 3.4% of the observed molecules in the plume are ejected from the jets and their Mach number lies between 5 and 8. The estimated fraction of water vapor flux that is ejected from these jets is then between 15 and 25 %. The jet-to-vent ratio is set at 25% for the maximum case and at 20% for the average cases.

Ice-to-vapor Ratio

The ice-to-vapor ratio of the plume is very difficult to constrain as the estimates range from 0.1 to 0.7 [Nakajima and Ingersoll, 2016]. A better option is to fix the production rate of icy grains creating different ice-to-vapor ratios depending on the chosen water vapor production rate. An icy grain production rate of 51 $\pm$ 18 kg/s gives the best fit for an exponential distribution while the best fit for a Lorentzian distribution is 38 $\pm$ 13 kg/s [Ingersoll and Ewald, 2011]. The ice-to-vapor ratio for the maximum case is then 38/700 or 0.054, that of the high-end average case is 38/200 or 0.19 and that of the low-end average case is 51/200 or 0.255.

Initial Semi-major Axis, Jovian Quality Factor and Mass of the H_2O-layer

The values for the initial semi-major axis, Jovian quality factor and mass of the H_2O-layer are all linked together. As described in Section 3.4.4 a trial-and-error process is required to determine the appropriate values. To determine the initial mass of the H_2O-layer some smaller simulations were done with a time-step of $5{\cdot}10^6$ years. These indicated that an initial amount of 11 wt% would be removed completely removed for the maximum case. For the high- and low-end average cases the initial amounts are 2.5 and 0.6 wt% were chosen. The corresponding values for the initial semi-major axis and Jovian Quality Factor can be found in Table 5.1.

5.5 The Three Cases

This chapter has described the workflow of the simulation, the different design choices regarding the simulation and the different simulated variables. The three simulated cases represent a maximum case for which parameter values were chosen so that as much ice as possible would be removed and two average cases for which the parameter values were chosen such that they represent average values which are mentioned in literature. The difference between the two average cases is the velocity distribution of the erupted material: a Lorentzian distribution for the high-end average case and an exponential distribution for the low-end average case. The values for all the simulated parameters can be found in Table 5.1. Note that all values except the initial mass of the H_2O-layer were chosen to represent the three cases. Only after the parameters for each case were chosen was the initial mass of the H_2O-layer set with the goal of determining what the highest amount of ice was that each case could remove.

Table 5.1: Summary of the different values for all the simulated parameters for each of the three cases.

Parameter	Maximum case	High-end average case	Low-end average case
Initial H_2O-layer mass	11 wt%	2.5 wt%	0.6 wt%
Water vapor production rate	700 kg/s	200 kg/s	200 kg/s
Icy grain production rate	38 kg/s	38 kg/s	51 kg/s
Water vapor eruption velocity	750 m/s	450 m/s	450 m/s
Icy grain eruption velocity	100 m/s	100 m/s	100 m/s
Jet-to-vent ratio	0.25	0.20	0.20
Ice-to-vapor ratio	0.054	0.019	0.255
Jovian quality factor	2.8765E4	3.5579E4	3.7693E4
Initial semi-major axis	1.0806E8	8.2740E7	9.9452 E7
Velocity distribution	Lorentzian	Lorentzian	exponential

Chapter 6

Results and Discussion

6.1 Introduction

This chapter will start of by reporting the results of each simulation. The focus will lie on the end of each simulation, the amount of mass that was lost, the evolution of the interior structure of the H_2O-layer, the magnitude of tidal dissipation, the amount of geyser activity and the tidal migration of each case. A summary of the results can be found in Table 6.1. An in-depth discussion about these results can be found in Section 6.3 together with observed trends and a comparison with other literature. There one can also find a critical look at the approach of this study, its limitations and the applicability of the obtained results.

6.2 Results

6.2.1 End of the Simulations

Simulations were stopped when at least one of the three end criteria were met (see Section 5.3.4 for more details). In summary a simulation would end if the H_2O-layer was completely removed, if the eruptive area was reduced to zero or if the equilibrium solution required an ice shell thickness that was larger than the thickness of the remaining H_2O-layer. The simulation of all three cases was halted due to the third end criteria. At that point is was no longer possible to obtain an equilibrium solution and the simulations were halted. This was due to the fact that there was too little mass remaining in the H_2O-layer.

6.2.2 Mass Loss

The remaining mass within the H_2O-layer is shown in Figure 6.1. It is clear that all three cases were able to remove most of the H_2O-layer by the end of the simulation. For the maximum case about 0.14% of the initial mass remained, for the high-end average case 0.47% remained and for the low-end average case about 1.84% remained at the end of the simulation.

6.2.3 The Interior Structure of the H_2O-layer

Figure 6.2 shows the evolution of the internal structure of the H_2O-layer. For all three cases the thickness of the H_2O-layer decreased with time (see Figure 6.2a). The initial thickness is 210.47 km for the maximum case, 52.07 for the high-end average case and 12.77 km for the low-end average case. Figure 6.2b shows that the thickness of the ocean decreased in parallel with the decrease in thickness of the H_2O-layer. In contrast the thickness of the ice shell increased with time for each case. Figure 6.2c show the change in ice shell thickness for the whole simulation and Figure 6.2d gives a more detailed look in to the evolution of the ice shell for the first $8{\cdot}10^7$ years. Initially the thickness of the ice shells was very thin (9, 6.8 and 11.1 m for the maximum, high-end average and low-end average cases respectively) but increased with time. The rate of increase in thickness is highest for the first $1{\cdot}10^7$ years but is somewhat diminished afterwards. At the end of the simulations the thickness of the icy shell for the maximum, high-end average and low-end average cases are 326.96, 252.88 and 236.08 m respectively.

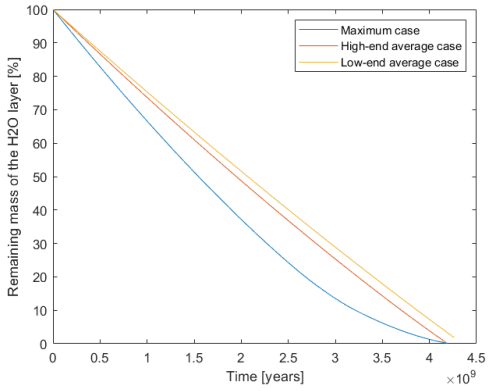

Figure 6.1: Evolution of the remaining mass of the H_2O-layer during the simulation for each case. It is clear that for all three cases almost all of the H_2O-layer had been removed by the end of the simulation. The reason why the simulations were stopped before all of the mass was removes is that it was no longer possible to obtain an equilibrium solution as required by the model.

6.2.4 Tidal Dissipation

In each case icy Io initially experiences a high tidal dissipation on the order of 2 - $3.5 \cdot 10^{15}$ W but after about $1 \cdot 10^8$ years the magnitude has already dropped by one order of magnitude. By the end of the simulation the magnitude of tidal dissipation was between 6.75 and $9.26 \cdot 10^{13}$ W. Figure 6.3a shows the tidal dissipation for each case while Figure 6.3b gives a more detailed version.

6.2.5 Eruptive Area and Surface Stress

For all three cases the eruptive area was initially 100% indicating that the whole surface had cracked and geysers were globally present (see Figure 6.4a). As time went on the eruptive area diminished steadily for the high- and low-end average cases while for the maximum case the rate by which the eruptive area decreased was accelerated at around $2.5 \cdot 10^9$ years and decelerated again at around $3.1 \cdot 10^9$ years. Figure 6.4b shows the maximum surface stress across the whole moon for each case. By the end of the simulation the maximum surface stress for the maximum case was only just larger than the failure threshold of 100 kPa required for crack instigation. This indicates that the amount of geysers had diminished greatly. This is substantiated by the eruptive area at the end of the simulation which was only about 15.84%. In contrast the maximum surface stress remained much higher for the average cases and consequently the eruptive areas remained much higher as well. By the end of the simulation the eruptive areas of the high- and low-end average cases were 74.94 and 82.98% respectively.

6.2.6 Tidal Migration

The tidal migration for each case can be seen in Figure 6.5. For each case the tidal migration rate was quite large for about $0.5 \cdot 10^9$ years after which it decreased somewhat and remained relatively constant from there on. By the end of the simulation the semi-major axis of the low-end average case was 99.96% of the present-day value. In contrast that of the high-end average and maximum cases had overshot the present-day value by about 2.79 and 13.88% respectively.

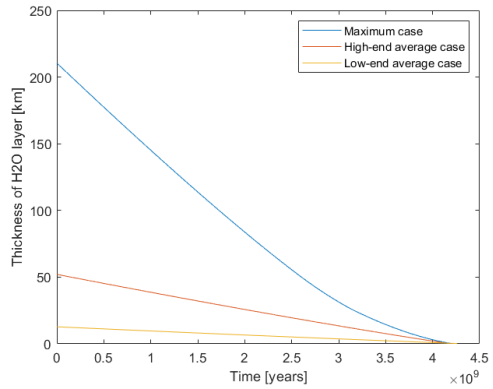

(a) Evolution of the thickness of the H_2O-layer

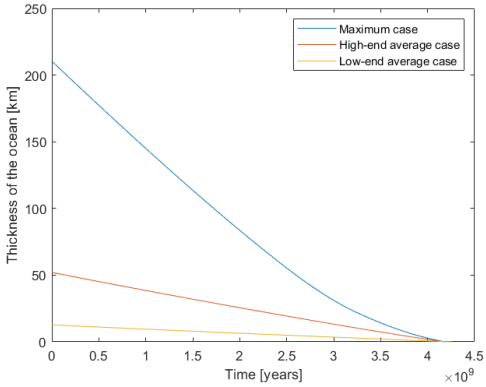

(b) Evolution of the thickness of the subsurface ocean.

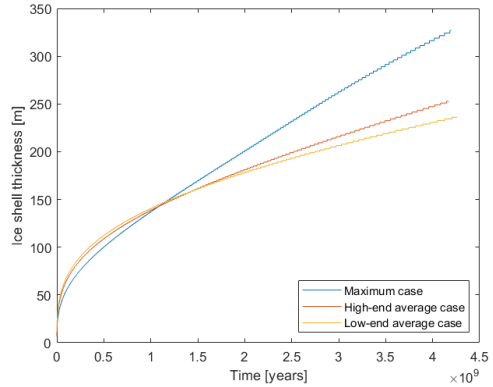

(c) Evolution of the thickness of the ice shells.

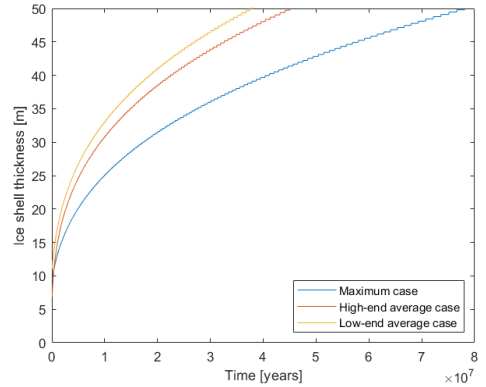

(d) Initial evolution of the ice shells.

Figure 6.2: Evolution of the internal structure of the H_2O-layers for each case. The evolution of each sublayer is given separately with b) showing that of the subsurface ocean, c) that of the ice shell and d) a more detailed representation of the evolution of the ice shells at the start of the simulations.

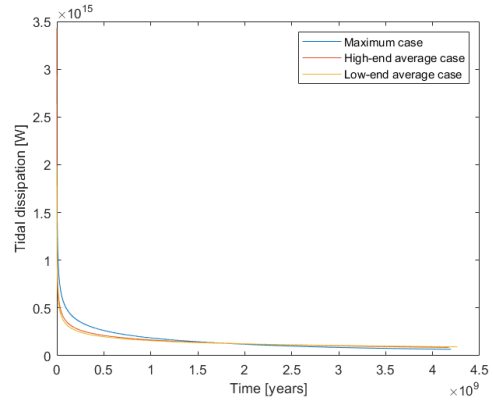

(a) Tidal dissipation for the three cases.

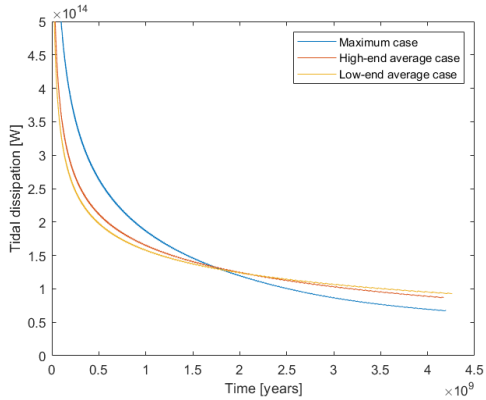

(b) Detailed tidal dissipation for the three cases.

Figure 6.3: The tidal dissipation for all three cases is shown in a) and a more detailed look is given in b).

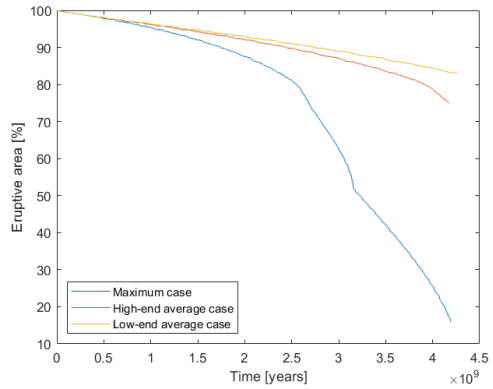

(a) Eruptive area.

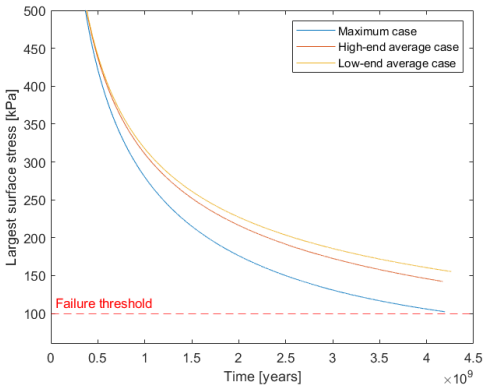

(b) Maximum surface stress.

Figure 6.4: The evolution of the geyser activity for the three cases is shown here. Figure a) shows the change in eruptive area given as a percentage of the total surface area and b) shows the evolution of the maximum surface stress across the whole moon. By the end of the simulation the maximum surface stress is only slightly larger than the failure threshold required for crack instigation.

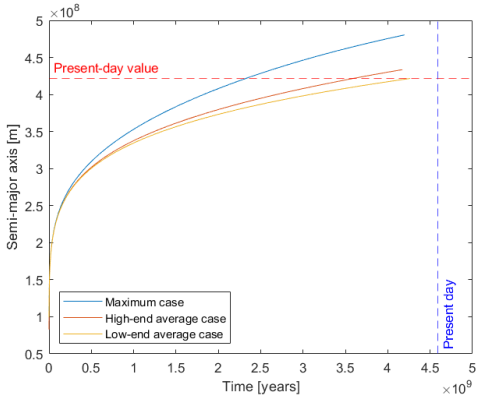

Figure 6.5: Evolution of the semi-major axes for each case. The starting locations were chosen to be as close to the Roche limit as possible. Initially the migration rate was similar for all three cases but that of the maximum case quickly increased above that of the two average cases. By the end of the simulation the maximum and high-end average cases had overshot the present-day value.

Table 6.1: Results for each simulated case.

Parameter	Maximum case	High-end average case	Low-end average case
Interior structure			
Initial thickness of H_2O-layer [km]	210.47	52.07	12.77
Final thickness of H_2O-layer [m]	327.51	252.95	236.21
Initial thickness of Icy Shell [m]	9	6.8	11.1
Final thickness of Icy Shell [m]	326.96	252.88	236.08
Initial thickness of Ocean [km]	210.46	52.06	12.76
Final thickness of Ocean [m]	1.08	0.59	0.26
Tidal Dissipation			
Initial magnitude [W]	$2.89 \cdot 10^{15}$	$3.43 \cdot 10^{15}$	$1.99 \cdot 10^{15}$
Final magnitude [W]	$6.75 \cdot 10^{13}$	$8.70 \cdot 10^{13}$	$9.26 \cdot 10^{13}$
Ice loss mechanism			
Remaining mass of H_2O-layer [%]	0.14	0.47	1.84
Initial eruptive area [%]	100	100	100
Final eruptive area [%]	15.84	74.94	82.98
Initial maximum surface stress [kPa]	10065.40	213326.23	12193.11
Final maximum surface stress [kPa]	102.27	142.27	155.39
Ratio of escaped to erupted material	0.21	0.13	0.03
Tidal migration			
Initial semi-major axis [m]	$1.08 \cdot 10^{8}$	$8.27 \cdot 10^{7}$	$9.95 \cdot 10^{7}$
Final semi-major axis [m]	$4.80 \cdot 10^{8}$	$4.34 \cdot 10^{8}$	$4.22 \cdot 10^{8}$

6.3 Discussion

6.3.1 Interpreting the Results

Figure 6.5 shows the evolution of the semi-major axis for all three cases. Both the initial position of the three cases and their tidal migration rate for the first $0.5{\cdot}10^9$ years is very similar after which the migration rate of the maximum case becomes larger than that of the other two cases. By the end of the simulation the semi-major axis had overshot the present-day value in all three cases and the overshoot was progressively worse as the initial mass of icy Io was larger. This shows that adopting a constant Jovian quality factor based on icy Io's initial mass as discussed in Section 3.4 is not a good assumption if the initial mass of icy Io is much larger than the present-day mass. If the difference between the initial mass and Io's present day mass is small enough, such as for the low-end average case, this assumption is valid if the initial semi-major axis is close to the Roche limit. One could use a different value for the Jovian quality factor that does not cause an overshoot.

The thicknesses of the ice shells are very similar for the first $1.1{\cdot}10^9$ years (see Figure 6.2) after which the difference between the maximum case and the two average cases became progressively larger. The rate of change of the thicknesses started to change earlier at around $0.5{\cdot}10^8$ years which is similar to the time at which the differences in semi-major axis became apparent too (see Figure 6.5). Therefore two periods will be distinguished here, a period of similarity up to about $0.5{\cdot}10^8$ years and a period of dissimilarity starting at $0.5{\cdot}10^8$ years. In the period of similarity the semi-major axes, thickness of the icy shells and rate of change of the thickness of the icy shells were similar for all three cases. The only difference between the three cases was the total thickness of the H_2O-layer (see Figure 6.2). During the period of dissimilarity the difference in semi-major axis between the maximum case and the two average cases became noticeable and kept increasing as time went on. The slopes of the three graphs in Figure 6.5 indicate that the migration rate was larger for the maximum case meaning that it migrated away from Jupiter at a faster rate than the two average cases. The rate of change of the thickness of the icy shells also started to differ between the maximum and the two average cases. The icy shell of the maximum case thickened more rapidly than those of the average cases. As the the only change between the two periods was the tidal migration rate it can be said that the main driver behind the thickness of the icy shell is the semi-major axis and the corresponding magnitude of tidal heat dissipation.

In this work the silicate mantle is reduced to one layer while in reality an asthenosphere is present as well [Steinke et al., 2020]. Here a parameterized viscosity and shear modulus were adopted in order to include the effect of this partially molten asthenosphere. The values for the mantle viscosity and shear modulus at the end of the simulation are compared to those obtained in literature to estimate how realistic the simulation is. Depending on the simulated case, the end values of the viscosity lie between $8{\cdot}10^{12}$ and $2{\cdot}10^{13}$ Pa·s. The values obtained here are close to the values of Steinke et al. [2020]. Their model 2 has viscosities of $8{\cdot}10^{14}$ Pa·s for the deep mantle and $3.5{\cdot}10^{12}$ Pa·s for the asthenosphere. Their model 2 incorporates tidal heating in both the deep mantle and the asthenosphere which more closely represents the model used in this work, where tidal heating also happens in the complete mantle and the viscosity and shear modulus are both parameterized to mimic the partial melting of the asthenosphere. The fact that the values lie between those of the asthenosphere and deep mantle obtained by Steinke et al. [2020] is to be expected. The same observations as for the mantle viscosity can be made for the shear modulus. At the end of the simulations the value for the shear modulus lies between about $1{\cdot}10^8$ Pa and $2{\cdot}10^8$ Pa which again is in line with those of Steinke et al. [2020]. Their model 2 has a shear modulus of $9{\cdot}10^7$ Pa for the asthenosphere and $2{\cdot}10^9$ Pa for the deep mantle. This indicates that assuming a simplified one-layer silicate mantle can, for the cases described in this work, give similar results as using a two-layer silicate mantle by adopting a parameterized viscosity and shear modulus for the whole one-layer mantle and that doing so was thus an acceptable assumption.

The rate of change of the production rate and escape rate for the maximum case underwent two significant changes at about $2.6{\cdot}10^9$ years and $3.15{\cdot}10^9$ years. This same observation can be made for the eruptive area. Figure 6.6a shows this observation for the eruptive area and the escape rate. Theoretically the reduced eruptive area could be due to two reasons: the first being that the surface stress at that time falls below the threshold in a significant number of places and the second being that the max crack

length falls below the thickness of the ice shell layer for a significant number of places. However as Figure 4.1 shows for the cases simulated in this work the maximum crack length was always much larger than the ice shell thickness at surface stress levels above the threshold value. Therefore the drop in eruptive area and the corresponding drop in production and escape rate is solely due to the surface stress falling below the threshold for multiple locations over the surface of icy Io. The high-end average case show the same trend but with only one significant change at a much later time of about $4{\cdot}10^9$ years. This can be seen in Figure 6.6b. A striking similarity is the fact that this happens when the eruptive area reaches 80% for both cases. This could possibly be due to the fact that at those moment the two cases have a similar semi-major axis: $4.3226{\cdot}10^8$ m for the maximum case and $4.3014{\cdot}10^8$ m for the high-end average case, which is a difference of only 0.5% indicating that in both cases icy Io is at the same distance from Jupiter when the eruptive area reaches 80 %. The amount of eruptive area depends on the surface stress which in turn is a result of the tidal deformation within the moon. The amount of tidal forces depends on the distance from Jupiter and on the interior of the moon. As their distance from Jupiter is similar the difference in deformation and thus surface stress will depend on the difference in interior structure. Even though there is a difference in internal structure it is too small to have a big impact on the surface stress and thus the semi-major axis is again the main driver behind the eruptive area. The low-end average case does not show this drop in eruptive area, production rate and escape rate, possibly because the eruptive area is still about 83% by the end of the simulation. Unfortunately the low-end average case did not reach the same semi-major axis during its simulation so it can not confirm the conclusions obtained from the maximum and high-end average case.

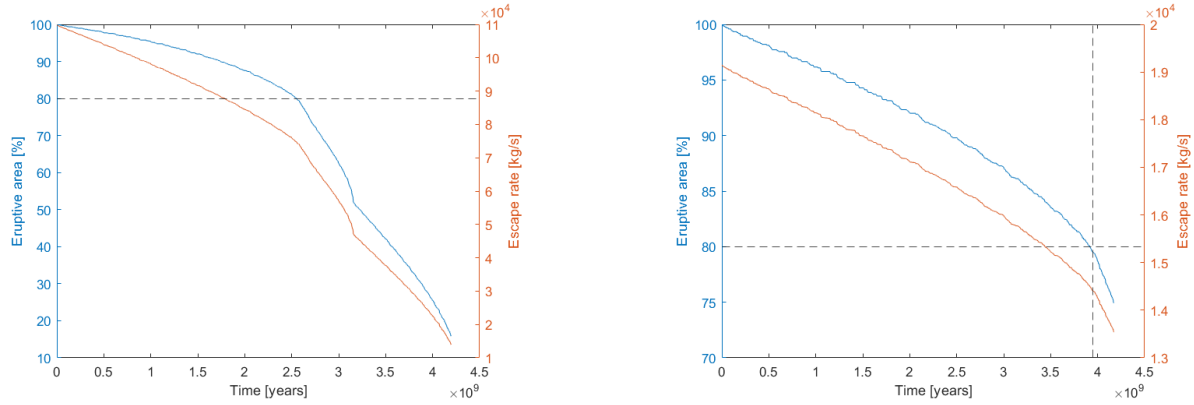

(a) Maximum case

(b) High-end average case

Figure 6.6: Evolution of the eruptive area and escape rate for the maximum case (a) and the high-end average case (b). Both cases experience a significantly larger decrease in geyser activity once the eruptive area fell below 80%.

Figure 6.4b indicates that by 4.20E9 years the levels of surface stress across icy Io were so low for the maximum case that geyser activity would soon be halted, irrelevant of the amount of water that was left. This is representative of a case where the migration rate happens too fast, as is discussed in Section 3.4.4. The maximum surface stress for the average cases remains well above the threshold of 100 kPa for the duration of the simulation. Even though the eruptive areas have decreased since the start of the simulation geyser activity is still present over the majority of the surface.

The fraction of erupted material that escapes is equal to 0.21, 0.13 and 0.03 for the maximum case, high-end average case and the low-end average case respectively (see Table 6.1). The main difference between the maximum and high-end cases are the jet-to-vent ratio, the parameterized production rate of Enceladus and the eruption velocity of the vapor molecules leaving the vents. The only difference between the high-end and low-end average cases is the velocity distribution (Lorentzian for the high-end case and exponential for the low-end case). This shows that the effect of the velocity distribution has a larger impact on the escape rate than the combined effects of the jet-to-vent ratio, parameterized production rate and eruption velocity of the vapor molecules out of the vents. The escape fractions given here indicate

that they are constant for each case. In reality they change very slightly because the escape velocities only change slightly between the start and end of the simulations. as a result the the change in escape fraction is less than 0.2% for each case which is negligible.

6.3.2 Critical Reflection on the Approach and Assumptions

The applicability of the results obtained in this work hinge on two major assumptions. The first assumption is that of an equilibrium solution and the second assumption is the parameterization of Enceladus' eruption rate is applicable to an icy Io. The validity of these assumptions and other associated assumptions are discussed below.

Equilibrium State

The first major assumption of this work is that icy Io is considered to be in an equilibrium state. This implies that any changes will occur very slowly. The results given in Section 6.2 regarding the semi-major axis, ice shell thickness, tidal dissipation and mantle temperature indicate that this may not be the case at the beginning of the simulation. The following section will discuss the maximum case but the broad implications also hold for the other two cases. The parameters that undergo a significant change at the start of the simulation are listed in Table 6.2. The biggest changes occur in the first $5{\cdot}10^8$ years after which the rates of change remain relatively constant. The average rates of change for these two periods are calculated and can also be seen in Table 6.2. The values for the second (and longest) period of the

Table 6.2: Average rates of change for the maximum case divided in two periods. A period of increased rates of change for about $5{\cdot}10^8$ years and a period of decreased rates of change afterwards.

Parameter	Average rate of change	
	0 - $5{\cdot}10^8$ years	$5{\cdot}10^8$ - $4.2{\cdot}10^9$ years
Semi-major axis	40.3 cm/year	4.6 cm/year
Ice shell thickness	1.82 $\cdot 10^{-7}$ m/year	6.13 $\cdot 10^{-8}$ m/year
Tidal dissipation	-5.24 $5{\cdot}10^6$ W/year	-5.34 $5{\cdot}10^4$ W/year
Mantle temperature	-1.89$\cdot 10^{-7}$ K	-2 $\cdot 10^{-8}$ K/year

simulation show that the rate of change of these parameters is quite low. Hussmann and Spohn [2004] modeled the thermal-orbital evolution of Io and Europa and concluded that they probably underwent a non-equilibrium phase with large variations in mantle temperature, eccentricity and heat production before entering a quasi-equilibrium phase where these parameters did not change much. During this quasi-equilibrium phase the rate of change of the mantle temperature was about 1.25 $\cdot 10^{-8}$ K/year which is similar to the value obtained for the second part of the simulation. This indicates that for the majority of its lifetime an icy Io as modeled in this work will be in a quasi-equilibrium state. It must be noted that the surface heat flow obtained by the model of Hussmann and Spohn [2004] is not equal to the present-day observed heat flow on Io. The authors suggest that either Io is not in equilibrium or that their value for the Jovian quality factor is too high. According to Hussmann and Spohn [2004] a value on the order of $5{\cdot}10^4$, quite similar to the values used in this work, would result in the correct surface heat flow.

Lastly Hussmann and Spohn [2004] also included the effect of a changing eccentricity which was not included in this work. Because the eccentricity is a driving factor behind the amount of tidal dissipation within a moon the assumption of a constant eccentricity has a big impact on the results. It may well be that if the eccentricity was allowed to vary an icy Io would also have entered an oscillatory phase as described by Fischer and Spohn [1990] andHussmann and Spohn [2004]. Such a phase is characterized by fluctuating values of the eccentricity, tidal dissipation, internal temperature and ice shell thickness (if present). Both Fischer and Spohn [1990] and Hussmann and Spohn [2004] estimate that Io will reach such an oscillatory phase within 1 - 1.6 $\cdot 10^9$ years from now. They also both indicate that the onset of such an oscillatory phase depends on the mantle temperature with the critical value lying between 1600 and 1700 K. Figure 6.7 shows the average mantle temperature for each case. It is clear that the mantle temperatures

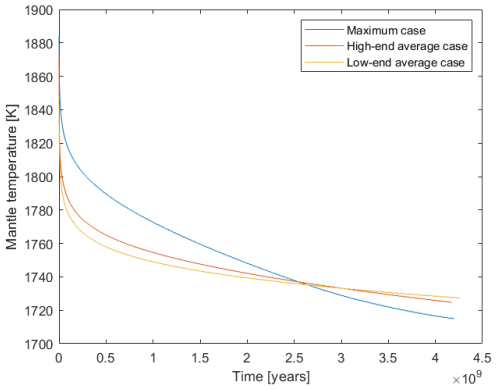

Figure 6.7: The evolution of the average mantle temperatures for each case. Initially quite high the temperatures decrease with time, initially quite rapidly but later at a smaller rate. By the end of the simulation they are close to the range for the onset of an oscillatory phase, which is between 1600 and 1700 K [Hussmann and Spohn, 2004], indication that such an oscillatory phase is probable in the future of these three icy Ios.

remain above the critical range mentioned above but that they are decreasing with time indicating that such an oscillatory phase might happen in the future as the models of Fischer and Spohn [1990] and Hussmann and Spohn [2004] predict. It must be noted that if one couples the thermal-orbital evolutions of Io and Europa, as Hussmann and Spohn [2004] did, that Europa experiences a short oscillatory phase between 2 and $3.2 \cdot 10^9$ years after formation and as a result Io experienced a small bump in eccentricity, mantle temperature and tidal dissipation rate which will have an effect in the mass loss rate of icy Io. Because this bump is small it is not expected to have a significant impact on the total mass loss.

The conclusion here is that the assumption of a constant eccentricity is acceptable as the resulting state of (quasi-) equilibrium is expected to hold even if a varying eccentricity is included for the time since formation. The results of Fischer and Spohn [1990] and Hussmann and Spohn [2004] indicate that in the future a varying eccentricity will lead to an oscillatory phase and the it can no longer be assumed that Io will be in an equilibrium state.

Parameterization of Enceladus' Eruption Rate

Estimating the amount of ice that an icy Io could have lost requires the adoption of one or more ice loss mechanisms. Even though there are many possibilities in this work the choice was made to use geysers. The magnitude of tidal heating that occurred in the icy Ios was able to keep part of the icy shell liquid. This subsurface ocean can then act as the reservoir for geyser activity. In this work the assumption is made that Enceladus, or at least its South Polar Terrain, is a typical example of geyser activity on icy moons and that the ice loss mechanism on icy Io is an upscaled copy of that on Enceladus. To test this assumption one can evaluate the differences between Enceladus and icy Io and estimate how these might affect the validity of the assumptions made.

A key feature of Enceladus' South Polar Terrain are the four Tiger Stripes. This works assumes that such features would also be observed on an icy Io. This is based on the work by Rhoden et al. [2020] who found that the Tiger Stripes are tensile fractures due to eccentricity tidal stresses. In the simulations that were performed the icy shell of Io was much thinner than that of Enceladus over icy Io's complete lifetime for all three cases. The presence of tensile fractures within Io's icy shell can therefore not be excluded as Rhoden et al. [2020] found that even the thinnest ice shells in their models, which were 500 m thick, resulted in tensile fractures which had the same orientations as Enceladus' Tiger Stripes. These results seem to suggest that similar fractures would result on the surface of any icy moon with a thin icy shell that experiences eccentricity driven tidal stresses which result in sufficiently large surface stress to allow for crack instigation and propagation, as with the cases simulated in this work. Figures 6.2c and 6.2d show the thicknesses of the ice shells for the whole simulation and at the start of the simulations

respectively. From these figures it is clear that they are much thinner than Enceladus' ice shell and that the crack depth required to reach the subsurface ocean is thus much less.

Note that the cracks will be partly filled with water due to isostacy. Even though this will shorten the effective length of the cracks the ratio of the crack lengths between the simulated models and Enceladus will remain the same. The effect of shorter crack lengths was investigated by Nakajima and Ingersoll [2016] who modeled the flow of vapor through different cracks. They found that for straight cracks an increase in crack length brought on a decrease in mass flow due to back pressure. The authors consider evaporation at the liquid-vapor interface within the cracks as the source of the vapor. This back pressure arises from friction with the crack wall and determines the evaporation rate. These results indicate that the production rate of the vents in this model could be larger and that the parameterized production rate of Enceladus is thus an underestimation for an icy Io based on the length of the cracks. This is not always the case however if crack width is also taken in to account. The results of Nakajima and Ingersoll [2016] show that an increased crack width also increases the mass flow rate through the cracks. Thus even though the crack lengths are shorter that positive effect could be negated if they were much less wide than those of Enceladus which may be the case. According to Porco et al. [2014] there is a critical crack width w_{crit} in order for propagation timescale to be less than the freezing timescale and is given by the following equation.

$$w_{crit} \sim \left(\frac{l^{3/2} \rho^{1/2} \kappa}{\sigma^{1/2}} \right)^{2/5} \tag{6.1}$$

Here the density ρ and the thermal diffusivity for ice κ are equal for both icy Io and Enceladus. While the surface stresses are on the same order of magnitude the crack length of Enceladus is at least one order of magnitude larger. This means that the critical crack width is larger for Enceladus and that the minimum possible crack widths of Enceladus are larger than those of icy Io. Even though this does not say anything about the actual or maximum crack length it does suggest that at least a fraction of Enceladus' cracks are wider and thus have an increased mass flow as compared to icy Io. The conclusion here is that neither crack length or width is able to indicate whether the parameterized eruption rate of Enceladus is applicable to icy Io but that using the parameterized production rate of Enceladus might give an overestimation of icy Io's eruption rate. A last note is that one of the boundary conditions that Nakajima and Ingersoll [2016] used at the surface of the moon is that the flow velocity equals the sound of speed. As such their results are not applicable to the supersonic flow out of the jets. Thus it remains unclear if the very thin ice shells at the start of the simulations would be able to accelerate the vapor molecules to supersonic speeds.

Figure 6.8 shows the ice-to-liquid ratio of the H_2O-layer for the three cases. It shows that at the end of the simulations the H_2O-layer is almost completely frozen. It is unclear what effect this has on cryovolcanic activity but the magnitude of this effect on the simulations is estimated to be low because of the following reasons. The first being that this happens at the very end of of the simulation when the H_2O-layer is almost completely removed anyway and the second being that the duration is very limited. For the low-end average case this ratio is above 0.8 for the last 2.2E7 years, which is the last 0.5% of the simulation. Figure 6.8 shows that this duration is even shorter for the other two cases.

A final consideration to take in to account is the cyclic behavior of geysers on icy moons. It has been shown that the production rate of Enceladus is variable Hedman et al. [2013]. It is thought that cracks alternatively become wider and narrower as Enceladus moves along. For half the orbit the crack is under tension and will be wider while it will be narrower or might even close during the other half of the orbit as it will be under compression [Hurford et al., 2007]. Wider cracks are associated with a higher eruption rate but equal eruption velocities [Nakajima and Ingersoll, 2016]. The exact effect of this periodic behavior is not yet understood but it is sure to have an effect on the escape rate. In this work the cyclic behavior is not included and it is assumed that the eruption rate is constant. If this constant eruption rate is similar to the actual eruption rate whilst the cracks are at their widest then it will lead to an overestimation. If however it is similar to the eruption rate whilst the cracks are at their narrowest it will lead to an underestimation. As discussed in Section 4.4.3 the estimated eruption rates of Enceladus vary from 120 to 1050 kg/s. These estimates are based on several observations at different times. Unfortunately it is not known what the state of the cracks were at the times of observation and if they were at their widest, narrowest or somewhere in between. Consequently it is difficult to predict which state is represented by

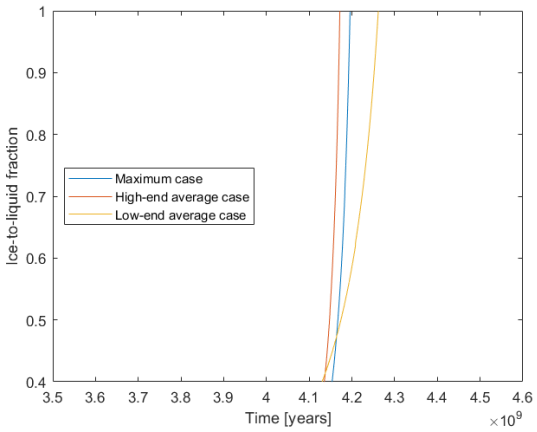

Figure 6.8: Ice-to-liquid ratios of the H_2O-layer

the used parameterized eruption rates. What can be said is that it is possible that the highest estimates concur with cracks at their widest and that the lowest estimates concur with cracks at their narrowest. Therefore the high eruption rate of the maximum case, 738 kg/s, is likely to be an overestimation and the average eruption rate of the average cases, 238-251 kg/s, is likely to be closer to a time-averaged eruption rate.

Chapter 7

Conclusions and Recommendations

7.1 Introduction

Of the four Galilean satellites Io, Europa, Ganymede and Callisto, Io is the only one without any ice. This work has assumed that Io did at some point contain ice but that it was lost through some sort of ice loss mechanism. There are multiple possible mechanisms that could have contributed to Io's ice loss however this work only considers ice loss through geysers which are driven by tidal heating. No ice loss through any other possible ice loss mechanisms has been included.
The source of tidal heating is the tidal forces which arise from Io's interaction with Jupiter's gravitational field. Tidal forces cause periodic deformation within Io which causes energy to be dissipated as heat, hence the term tidal heating. If tidal heating within an icy Io is sufficiently large it is able to melt part of its H_2O-layer resulting in a subsurface ocean over which lies an icy shell. Following the model proposed by Schmidt et al. [2008] this subsurface ocean acts as the reservoir for the geysers. The key assumption regarding icy Io's geyser activity is that it can be modeled after that the geysers of Enceladus.
The deformation caused by tidal forces also results in surface stress which, if large enough, is able to fracture the icy shell after which cracks are able to propagate from the surface down to the subsurface ocean. Here a failure threshold of 100kPa was applied and all other sources of surface stress that could contribute have been neglected. It is through these cracks that water vapor molecules and icy grains are able to accelerate as they rise and are ultimately erupted at the surface. If their eruption velocity is higher than the escape velocity of Io they are considered lost. The velocity distribution of the erupted particles depends on the applied distribution. The two possibilities used in this work are an exponential and a Lorentzian distribution. It is by this method that the ice loss of an icy Io is modeled in this work.

The main contribution of this work is by combining different pieces of work on a range of topics to create a detailed model of icy Io's ice loss. Existing literature does not give a detailed or thorough answer to the possibility of ice loss on Io through tidal heating. Previous work on this topic such as that of Bierson and Steinbrügge [2021] focuses on the energy required to remove a certain amount of ice from Io. From the required energy and the available energy through tidal heating a required efficiency of the ice loss mechanism can be obtained. The authors then compared the required efficiency to the efficiency of several possible ice loss mechanisms to determine which could be applicable. This work improves on previous work by creating a detailed model of an icy Io and its ice loss through tidal heating. One example of this is by allowing the initial mass of icy Io's H_2O-layer to vary by selecting three different cases with different initial masses of the H_2O-layer. Another example is that the model in this work incorporates the thermal evolution of Io over its lifetime. By doing this the effect of icy Io's migration rate and corresponding change in tidal dissipation and the effect of a diminishing H_2O-layer because of the ice loss are included. A third example of what this work adds to the existing knowledge is the incorporation of a detailed ice loss mechanism. By adopting the geyser activity of Enceladus, which has been proven to cause ice loss on Enceladus, a specific ice loss mechanism has been used in stead of considering several possible ice loss mechanisms based on their efficiency only.

The model that has been built in this work was then used to simulate the thermal evolution of three distinct cases. These simulations were done in order to answer the main research question:

How much ice could an icy Io have lost through tidal heating?

7.2 Conclusions

In order to answer the research question the thermal evolution of three difference cases was simulated. All parameters of the maximum case were set as to obtain a maximum amount of mass loss. For the high-end and low-end average cases these parameters were set at more average values with the difference between them being the velocity distribution of the particles that are erupted by the geysers. The high-end average case used a Lorentzian distribution and the low-end average case used an exponential distribution. The case-specific values for all the parameters can be found in Table 5.1. The three simulations cases started off with H_2O-layers that were about 13, 52 and 210 km thick for the low-end average, the high-end average and maximum cases respectively. As a comparison the H_2O-layers of Europa and Enceladus are estimated at 140 km[Hussmann and Spohn, 2004] and between 60 and 100 km [Spencer and Nimmo, 2013] respectively.

The combination of Jupiter's gravitational field and a prolonged eccentric orbit through the Laplace resonance kept tidal heating high during Io's lifetime. For a fully differentiated icy Io, as is assumed in this work, this resulted in the presence of a subsurface ocean underneath a thin ice-I shell for all three cases for the duration of the simulations. This internal structure is similar to that of Europa. For an interior structure such as that of Ganymede, where there is an additional high-pressure ice shell underneath the subsurface ocean, an H_2O-layer of at least 600 km is required. A key assumption of this work was that icy Io remained in an equilibrium state. This meant that the heat flow through each (sub)layer of the icy shell was equal to the heat flow coming out of the silicate mantle. Several iterative processes were required to find an internal structure that fulfilled the assumption of an equilibrium state. The resulting equilibrium structure contained very thin ice shells which were thinner than 350 m for their complete lifetimes. Tidal heating occurred in both the silicate mantle and the icy shell but as the icy shell was so thin almost all of the tidal dissipation happened in the silicate mantle.

The case example of mass loss through geysers on icy moons is Enceladus and form the base of the model used in this work. Three requirements have to be fulfilled in order for there to be geyser activity. The first is the presence of a subsurface ocean and the second is that an icy shell lies above this ocean. All three cases met these two requirements for the duration of the simulation. The third requirement is that cracks exist which connect the surface with the subsurface ocean. Crack instigation happens where the surface stress is higher than the assumed failure threshold of 100 kPa. The minimum required stress for crack propagation for all three cases lies below this failure threshold. Lastly the maximum crack depth also depends on the amount of stress. For a surface stress of 100 kPa the crack depth is slightly more than 1000 m. As the maximum ice shell thickness for every case lies below 350 m the cracks will always be able to reach the subsurface ocean which acts as the liquid reservoir for the geysers. Thus one can conclude that if the surface stress is high enough for crack instigation then the cracks will propagate far enough to reach the subsurface ocean for every case. The major assumption here is then that the geyser activity of Enceladus is a typical example and should be common across the universe. Several aspects of icy Io's H_2O-layer are supportive of this claim. The first of which is that the surface stresses on icy Io are comparable in magnitude to those of Enceladus, indicating that the icy shell could be heavily fractured. Eccentricity driven tidal stresses are able to fracture the thin icy shells and cause crack propagation from the surface to the subsurface ocean for all three cases. For each case initially 100% of the surface area was so-called eruptive area resulting in global geyser activity. The second aspect in favor of this assumption is that icy Io's icy shells are much thinner than that of Enceladus, increasing the frequency of cracks reaching from the surface to the ocean beneath. Under the assumption of an equilibrium state the thicknesses of the ice shells are at least a factor of 10 smaller than those of Enceladus.

The important parameters describing Enceladus' geyser activity are the production rate, jet-to-vent ratios, characteristic bulk velocities and eruption velocity distributions. The production rate is defined as the mass flow leaving the geysers and has the largest range of estimates from literature. As mentioned above the cracks of Enceladus open and close along the orbit resulting in a changing eruption rate. In this work however production rates have been considered constant. It is uncertain if this causes an

over- or underestimation of the actual production rate as the chosen production rate is based on that of Enceladus. All estimates regarding the production rate of Enceladus have come from measurements taken by and observation made by Cassini during several flybys or stellar occultations. By definition these are are only representative of the instantaneous eruption rate of Enceladus. As more data from other measurements and observations is obtained it will be possible to reduce the spread in estimates and calculate more accurate average production rates. Even a more accurate average production rate might not be representative of the production rate in the past. As discussed above the main driver of the amount of geyser activity is the semi-major axis as this is also a major contributing factor to the magnitude of tidal dissipation. As satellites experience orbital migration throughout their lifetimes the magnitude of tidal dissipation will have changed correspondingly. As Enceladus has migrated outwards since its formation the production rate of its geysers will probably have been larger in the past. In this work the erupted material can either come from vents or jets. Vents are here defined as the cracks from which the material erupts at lower velocities while the jets are the cracks from which the material erupts at supersonic velocities. The jet-to-vent ratio is a parameter that describes how much mass flow comes from the vents and how much from the jets. Estimates from literature range from 0.15 to 0.25 [Hansen et al., 2011] thus for the maximum case a jet-to-vent ratio of 0.25 was chosen and for the average cases a value of 0.20 was chosen. The characteristic velocity of the erupted material is the average of bulk velocity of the erupted material. The spread of the eruption velocity for each erupted particle individually is best represented by a Lorentzian or exponential distribution. The effect of the velocity distribution that was applied to the erupted material had a bigger effect than that of the production rate, jet-to-vent ratio and characteristic eruption velocity combined.

The initial mass of each case's H_2O-layer was chosen so that the maximum possible amount of ice would be removed. In the end more than 98% of the H_2O-layer was removed for all three cases. The simulations were halted not because no more mass was lost but because an equilibrium solution could no longer be found. More specifically the equilibrium solution required a certain ice layer thickness which, at those times during the simulations, had become larger than the thickness of the remaining H_2O-layer. This was one of the three end criteria for the simulations. The other two criteria were that either all H_2O had been removed or that the surface stress no longer reached the failure threshold effectively halting all geyser activity and mass loss. The maximum case in particular was able to remove a substantial amount of water. It was able to remove a H_2O-layer of about 210 km thick which is thicker than than that of present-day Europa. But it must be taken in to consideration that all parameters were set to obtain the highest escape rates. The high- and low-end average cases might offer a more truthful result as their parameters weren't set to push for maximum escape rates. In comparison the high-end average case was able to remove a layer of 52 km which is slightly below the minimum estimates for the thickness of Enceladus' H_2O-layer and the low-end average case was able to remove a layer of about 12 km thick.

The results of this work are most applicable to Io-like moons. Their orbit must be eccentric in order to experience the required tidal dissipation so that their H_2O-layer is at least partly liquid. Furthermore such geyser activity requires a long time to have a significant impact on the ice loss of a moon. This requires that the orbit remains eccentric for a long time, such as the case for satellites which are in a resonance with other nearby satellites. If a satellite would experience one or multiple other ice loss mechanisms however this requirement is relaxed somewhat. While it has been shown that Io and Europa can enjoy long equilibrium periods [Hussmann and Spohn, 2004] it is highly improbable that they have been in equilibrium for their whole lifetimes. For the three simulated cases the equilibrium assumption therefore might not hold for the initial stages of icy Io's lifetime. The rapid change in heat dissipation, migration rate and mantle temperature, viscosity and shear modulus for the first $5{\cdot}10^8$ years of each simulation seem to confirm this. Whether the rate of change of a parameter is considered rapid or slow is based on the work Hussmann and Spohn [2004]. There the authors distinguish periods of (quasi-)equilibrium and non-equilibrium for Io's thermal-orbital evolution. By looking at the rate of change of several parameters such as the mantle temperature and tidal dissipation within these two periods a rough range can be determined for when the rate of change is considered rapid or not. Afterward the rapid non-equilibrium start of the simulations the aforementioned parameters show a much smaller rate of change indicating that the simulated icy Io's have entered a (quasi-)equilibrium state. In order to determine the amount of ice loss Io could have experienced due to tidally driven geysers care must be taken to apply the methodology and results of this work to periods of (quasi-)equilibrium only as this assumption forms one of the bases

of this work.
This work assumes three conditions for the existence of geysers: (1) there must be a subsurface liquid reservoir, (2) an icy shell must lie over this reservoir and (3) there must be cracks within the icy shell that connect the surface and the liquid reservoir. These requirements are quite simple and rest on some other assumptions, such as a failure threshold of 100 kPa for the icy shell, which must be further investigated to determine how acceptable they are. However, the geysers activity of Enceladus on its South Polar Terrain does meet all three of these requirements. Because of this, and the fact that Enceladus is losing ice through its geysers, the same conditions were applied to icy Io in order to determine its amount of geyser activity. Thus copying and upscaling Enceladus' geyser activity is a good first approximation to that of icy Io.

If Io once did contain ice then it is quite probable that geysers driven by tidal heating contributed to its ice loss. This is based on the methodology used in this work and the thermal evolution simulations of the three cases. The methodologies used to create the model of icy Io's interior have been verified against other literature. The modeling of ice loss through geysers is bases on the geyser activity of Enceladus, which has been shown to cause ice loss. This work uses three criteria for the existence of geysers on icy Io. They are relatively simple and further work needs to be done to refine these criteria. When applied to Enceladus' SPT they confirm the existence of geysers and therefore can be applied as a first estimate for the existence of geysers on icy Io. The three different cases all indicate at least some ice loss. The parameters for the maximum case were set to obtain the maximal amount of ice loss and as such this case might not be very probable. The situation is different for the two average cases, for which the relevant parameters were chosen to represent average values found in literature. Therefore they represent a much more probable model.

7.3 Recommendations

By creating a detailed model of an icy Io and its geysers and simulating the thermal-orbital evolution of the three cases a satisfying answer to the research question was obtained. There are however several ways to improve the model and the simulations by which a better answer to the research question can be obtained. These will be grouped according to the research sub-questions stated in Chapter 1. To start off though some recommendations regarding the simulations itself will be proposed.

During the simulations the surface stress was not calculated every iteration but once every 50. This was done to save on computational time as doing this took up about 75% of the computational time of one iteration. On top of this the number of points at which the surface stress is calculated was limited, again to save on computational time. The first recommendation is then to increase the number of points at which the surface stress is calculated and to do this every iteration. Both of these will significantly increase the computational time but offer far more accurate results concerning the eruption rate of icy Io. A second recommendation is to perform simulations with a shorter time-step. This will again improve the accuracy but increase the computational time.

Geyser activity on icy Io is dependent on the magnitude of tidal dissipation through two consequences of this tidal dissipation: the presence of a subsurface ocean through partial melting of the icy shell and the creation of cracks in the icy shell through tidal stresses within this shell. In this work several simplifications were made that had an effect on the magnitude of tidal dissipation. One of these is the assumption that the H_2O-layer is pure water while in reality it would be somewhat saline. The effect of an increased salinity is a lower melting temperature. Therefore a subsurface ocean might be present at lower magnitudes of tidal dissipation. Another simplification is the omission of an asthenosphere within the mantle. This was somewhat compensated by adopting a parameterized viscosity and shear modulus but adding the asthenosphere as a separate layer would increase the accuracy of the interior model. The third recommendation is to improve the interior model of icy Io by considering the salinity of the H_2O-layer and/or adding an asthenosphere as a separate layer. The fourth recommendation is to extend this model to account for the phases were icy Io is not in an equilibrium phase. In such phases the main assumption of this work, the equilibrium condition, is not applicable and different method of establishing the internal structure should be applied. This would increase the accuracy of the ice loss during these periods of non-equilibrium.

In this work only the thermal evolution of icy Io with its orbital migration rate was considered. This model could be improved by performing a complete thermal-orbital evolution. Two recommendations are proposed in order to do this. The fifth recommendation is to allow for a change in eccentricity. The influence of a change eccentricity on the thermal-orbital evolution of Io has been omitted in this work. The magnitude of the tidal dissipation is dependent on the eccentricity to the second degree thus allowing the eccentricity to vary will increase the accuracy of the results. A sixth recommendation is to combine a thermal-orbital evolution model of icy Io with a model of the thermal-orbital evolution of Europa and the orbital evolution of Ganymede. An example of such a coupled thermal-orbital evolution is done by Hussmann and Spohn [2004]. The main reason for this can be seen in their Figure 5 where the evolution of several parameters of Io and Europa such as the tidal dissipation, mantle temperature and eccentricity is given. In their simulation Europa entered an oscillatory phase between 2 and $3.2 \cdot 10^9$ years which had an effect on the mantle temperature, tidal dissipation and eccentricity of Io. By including the influence of Europa on icy Io's thermal and orbital evolution a more accurate answer to the research question can be given.

The eighth recommendation is to look in to the cyclic behaviour of geysers. As noted by Hurford et al. [2007] the eruption rate of Enceladus' geyser follows a cyclic behaviour which is due to the different normal stresses experienced at different positions along the orbit. When under tensile stress the cracks are wider and when under compressive stress they are narrower or even completely closed. In this work the eruption rate is kept constant but by adding such a cyclic behaviour a more accurate eruption rate can be used. The ninth recommendation is to look more closely in to the velocity distribution of the erupted material. In this work only two distributions were considered, namely an exponential and a Lorentzian one. The fraction of erupted material that was lost is a factor of 3-4 times higher with a Lorentzian distribution than with an exponential one. This was by far the biggest impact of changing the geyser parameters and by investigating these two velocity distributions more thoroughly one of them could be eliminated. This would help in narrowing the range of the amount of ice that could be lost. Another possibility is to look in to other types of velocity distributions. The last recommendation concerns the parameters of the geysers. Only some parameters varied between each case and then only between two different values. By allowing more parameters to change and to include a wider range of values between which they can vary will give more insight in to the magnitude of ice loss and on which geyser parameters this depends most heavily. This could be done by using a Monte Carlo simulation.

Appendix A

Detailed Calculations

A.1 Calculating the Icy Shell Sub-layers

This section will describe the method to finding the thicknesses of the different ice sub-layers when in equilibrium. In equilibrium the heat flow through the stagnant lid is equal to that through the convective sub-layer.

$$Q_{stag} = Q_{conv} \tag{A.1}$$

The heat flow through the stagnant lid is given by:

$$Q_{stag} = \frac{k_{stag} \cdot (T_{top} - T_s)}{D_{stag}} \cdot 4\pi R^2 \tag{A.2}$$

The heat flow through the convective sub-layer is given by:

$$Q_{conv} = \frac{k_{conv} \cdot (T_m - T_{top})}{D_{conv}} \cdot \left(\frac{Ra}{Ra_c}\right)^{\beta} \cdot 4\pi \left(R - D_{stag}\right)^2 \tag{A.3}$$

With:

$$Ra = \frac{\alpha \rho g \left(T_m - T_{top}\right) D_{conv}^3}{\kappa \eta \left(T_{int}\right)} \tag{A.4}$$

Note that $D_{stag} = D_{ice} - D_{conv}$ and that the factor 4π is present in both Equations A.2 and A.3. Using this and substituting Equations A.2, A.3 and A.4 in to Equation A.1 gives the following:

$$\frac{k_{stag} \cdot (T_{top} - T_s)}{D_{ice} - D_{conv}} R^2 = \frac{k_{conv} \cdot (T_m - T_{top})}{D_{conv}} \cdot \left(\frac{\alpha \rho g \left(T_m - T_{top}\right)}{\kappa \eta \left(T_{int}\right) Ra_c}\right)^{\beta} \cdot \left(D_{conv}^3\right)^{\beta} \left(R - D_{ice} + D_{conv}\right)^2 \tag{A.5}$$

The unknown parameter in this equation is the thickness of the convective sub-layer, D_{conv}. To simplify Equation A.5 the following variables are introduced:

$$a = k_{stag} \cdot (T_{top} - T_s) R^2 \tag{A.6}$$

$$b = k_{conv} \cdot (T_m - T_{top}) \left(\frac{\alpha \rho g \left(T_m - T_{top}\right)}{\kappa \eta \left(T_{int}\right) Ra_c}\right)^{\beta} \tag{A.7}$$

$$c = R - D_{ice} \tag{A.8}$$

Thus Equation A.5 can be simplified to:

$$\frac{a}{D_{ice} - D_{conv}} = b \frac{D_{conv}^{3\beta}}{D_{conv}} \left(c + D_{conv}\right)^2 \tag{A.9}$$

The value for β is usually taken to be 0.3. To further simplify the calculations the following parameters are introduced: $D_{ice} = d$ and $D_{conv} = x$, giving the following:

$$b x^{-0.1} \left(c + x\right)^2 - \frac{a}{d - x} = 0 \tag{A.10}$$

Equation A.10 then contains the parameters a through d and the unknown x. To find the roots for this equation the Newton root finding algorithm is used.

This algorithm uses a function and its derivative to progressively get closer to the root starting from an initial guess. This is done as follows:

$$x_{n+1} = x_n - \frac{f(x_n)}{f'(x_n)} \tag{A.11}$$

Starting from an initial guess x_0 successive calculations of x_n will get closer to the root of the function. Expanding Equation A.10 gives the following:

$$f(x) = bc^2x^{-0.1} + 2bcx^{0.9} + bx^{1.9} - a\,(d-x)^{-1} \tag{A.12}$$

$$f'(x) = -0.1bc^2x^{-1.1} + 1.8bcx^{-0.1} + 1.9bx^{0.9} - a\,(d-x)^{-2} \tag{A.13}$$

Equations A.12 and A.13 can then be used with Equation A.11 to determine the equilibrium values for the thicknesses of the icy sub-layers.

A.2 Calculating the Internal Pressure

The pressure at any point $P(r)$ within a moon can be calculated using equation A.14 [De Pater and Lissauer, 2015].

$$P(r) = \int_r^{R_P} g(r')\rho(r')\,dr' \tag{A.14}$$

In the above equation R_P is the planetary surface, $g(r')$ is the gravitational acceleration and $\rho(r')$ is the density at point r'. The gravitational acceleration is given by equation A.15.

$$g(r) = \frac{M(r)G}{r^2} \tag{A.15}$$

Here G is the gravitational constant and $M(r)$ is the mass of the internal sphere at radial distance r, which is given by equation A.16.

$$M(r) = \int_0^r 4\pi r'^2\rho(r')\,dr' \tag{A.16}$$

In equation A.16 $\rho(r')$ is the density of the internal sphere at radial distance r.

A.3 Calculating the tidal dissipation using weight functions

Average dissipated power per unit volume:

$$P_0 = \frac{\omega\,(nR)^4}{2r^2}\left(Im\,(\tilde{\mu})\,H_\mu + Im\left(\tilde{K}\right)H_K\right)\Psi_0 \tag{A.17}$$

The term with H_K can be ignored, leading to:

$$P_0 = \frac{\omega\,(nR)^4}{2r^2} Im\,(\tilde{\mu})\,H_\mu\Psi_0 \tag{A.18}$$

With:

$$\Psi_0 = \frac{21}{5}e^2 \tag{A.19}$$

$$H_\mu = f_A + f_B + f_C \tag{A.20}$$

f_J are the weight functions and dependent on the radial functions y_1, y_2, y_3, y_1', $\tilde{\mu}$ and r. It must be noted that different authors use different notations of these radial functions. Equations A.21 to A.25 use

the notation from Beuthe [2013]. The model in this work uses the notation from Sabadini et al. [2016]. To adapt the equations from Beuthe [2013] to be used in the code, the following changes must be made:

$$f_A = \frac{4}{3}\left|ry_1' - y_1 + 3y_2\right|^2 \tag{A.21}$$

$$f_B = 6\left|\frac{ry_4}{\tilde{\mu}}\right|^2 \tag{A.22}$$

$$f_C = 24\left|y_2\right|^2 \tag{A.23}$$

$$ry_1' = \frac{1}{\tilde{K} + \frac{4}{3}\tilde{\mu}}\left(ry_3 - \left(\tilde{K} - \frac{2}{3}\tilde{\mu}\right)(2y_1 - 6y_2)\right)^2 \tag{A.24}$$

Or if an incompressible medium,

$$ry_1' = -2y_1 + 6y_2 \tag{A.25}$$

With Equation A.25 Equation A.21 becomes:

$$f_A = \frac{4}{3}\left|-3y_1 + 9y_2\right|^2 \tag{A.26}$$

The complex shear modulus is defined as:

$$\tilde{\mu} = \frac{\tilde{E}}{2(1+\tilde{v})} \tag{A.27}$$

With $\tilde{E}$ and $\tilde{v}$ the complex Young's modulus and complex Poisson's ratio respectively.

Tidal dissipation in a layer can be calculated as:

$$\dot{E} = 4\pi \int_{r_1}^{r_2} P_0 r^2 dr \tag{A.28}$$

Substituting P_0 and Ψ_0 and with $n = \omega$ this becomes:

$$\dot{E} = \frac{42}{5}\pi n^5 R^4 e^2 \int_{r_1}^{r_2} Im\left(\tilde{\mu}\right) H_\mu dr \tag{A.29}$$

A.3.1 Evaluating the integral

In Equation 3.17 the imaginary part of the complex shear modulus, $Im(\tilde{\mu})$ is a constant and can thus be put outside of the integral. This leaves the following integral where the three integrals on the right hand side can be evaluated separately. The complete integral given by Equation A.30 is evaluated using Simpson's rule.

$$\int_{r_1}^{r_2} H_\mu dr = \int_{r_1}^{r_2} \left(f_A + f_B + f_C\right) dr = \int_{r_1}^{r_2} f_A dr + \int_{r_1}^{r_2} f_B dr + \int_{r_1}^{r_2} f_C dr \tag{A.30}$$

A.4 Velocity distribution of the erupted material

In this section the integration of the exponential and Lorentzian velocity distributions will be discussed in detail. For more information please refer to Section 4.4.5. Verification of these calculations can be found in Appendix E.2. At the end of this section an example calculation can be found.

Exponential Distribution

The method to determine the exponential velocity distribution as discussed in Section 4.4.5 is explained in detail below.

$$p(v) = \frac{1}{v_0} \exp\left(-\frac{v}{v_0}\right) \tag{A.31}$$

Where v is the eruption velocity of a particle according to the exponential distribution and v_0 is the characteristic bulk eruption velocity. To determine the fraction of the erupted molecules that have a velocity greater than the escape velocity v_{esc} one can simply integrate Equation A.31 above the escape velocity [Bierson and Steinbrügge, 2021]. This is shown in Equation A.32.

$$p(v_{esc} \leq v < \infty) = \int_{v_{esc}}^{\text{inf}} \frac{1}{v_0} \exp\left(-\frac{v}{v_0}\right) dv \tag{A.32}$$

Integration Equation A.32 gives the probability of a particle having a velocity larger than the escape velocity according to an exponential distribution.

$$p(v_{esc} \leq v < \infty) = \exp\left(-\frac{v_{esc}}{v_0}\right) \tag{A.33}$$

Lorentzian Distribution

The method to determine the Lorentzian velocity distribution as discussed in Section 4.4.5 is explained in detail below.

$$p(v) = \frac{2v_0}{\pi} \frac{1}{v_0^2 + v^2} \tag{A.34}$$

Where v is the eruption velocity of a particle according to the Lorentzian distribution and v_0 is the characteristic bulk eruption velocity. To determine the fraction of the erupted molecules that have a velocity greater than the escape velocity v_{esc} one can simply integrate Equation A.34 above the escape velocity [Bierson and Steinbrügge, 2021]. This is shown in Equation A.35.

$$p(v_{esc} \leq v < \infty) = \int_{v_{esc}}^{\infty} \frac{2v_0}{\pi} \frac{1}{v_0^2 + v^2} dv \tag{A.35}$$

Integration Equation A.35 gives the probability of a particle having a velocity larger than the escape velocity according to a Lorentzian distribution.

$$p(v_{esc} \leq v < \infty) = 1 - \frac{2}{\pi} \arctan\left(\frac{v_{esc}}{v_0}\right) \tag{A.36}$$

Fraction of Mass Lost per Velocity Distribution

This section will give more details about the fraction of lost mass example of Section 4.4.5. As mentioned there the plume is fed by vents and jets where 20% of the erupted material comes from the jets and 80% from the vents. Furthermore the ice/vapor ratio is set at 0.25. The resulting distribution can be seen in Table A.1. The results are given as percentage of the total erupted mass. The total fraction of mass that

Source	Vapor molecules	Icy grains
Vents	64	16
Jets	16	4

Table A.1: Fraction of the plume composition

is lost is the sum of the mass that is lost from the vents and from the jets, as given in Equation A.37.

$$f_{lost} = f_{lost,vent} + f_{lost,jet} \tag{A.37}$$

To then calculate the actual fraction of erupted mass that is lost a one must further distinguish between the vapor molecules and the icy grains. The erupted fractions of vapor molecules and icy grains as given in Table A.1 are $f_{vent,vapor}$ and $f_{vent,grain}$ for the vents and $f_{jet,vapor}$ and $f_{jet,grain}$ for the jets. Combining this with Equations 4.7 and 4.8 are the total mass fraction that is lost can be calculated with A.38.

$$f_{lost} = f_{vent,vapor} \cdot \exp\left(-\frac{v_{esc}}{v_{vent,vapor}}\right) + f_{vent,grain} \cdot \exp\left(-\frac{v_{esc}}{v_{vent,grain}}\right) + f_{jet,vapor} \cdot \exp\left(-\frac{v_{esc}}{v_{jet,vapor}}\right) + f_{jet,grain} \cdot \exp\left(-\frac{v_{esc}}{v_{jet,grain}}\right) \quad \text{(A.38)}$$

To calculate the first example case of Section 4.4.5 the following parameters, which correspond to those of the low-end average case, are used in Equation A.38. The escape velocity v_{esc} is equal to 2557.4 m/s, the eruption velocity of the vapor molecules in the vent $v_{vent,vapor}$ is 450 m/s, the eruption velocity of the vapor molecules in the jet $v_{jet,vapor}$ is 1600 m/s and the eruption velocities of the icy grains in the vent $v_{vent,grain}$ and in the jet $v_{jet,grain}$ are both 100 m/s. All these values correspond to the low-end average case. The resulting fraction of the erupted mass that is lost is given by Equation A.39.

$$f_{lost} = 0.64 \cdot \exp\left(-\frac{2557.4}{450}\right) + 0.16 \cdot \exp\left(-\frac{2557.4}{100}\right) + 0.16 \cdot \exp\left(-\frac{2557.4}{1600}\right) + 0.04 \cdot \exp\left(-\frac{2557.4}{100}\right) = 0.03453 \quad \text{(A.39)}$$

The mass fraction that is lost can be calculated similarly for the other example cases. If the eruption velocity of the icy grains coming out of the jets is increased to 500 m/s the resulting fraction of mass that is lost is equal to 0.03477. The fraction of escaped material is then increased by 0.024% which indicates that raising the escape velocity of the icy grains erupting from the jets does not have a significant impact on the fraction of escaped material.

Appendix B

Simulation Design Choices

B.1 Simulation Time-step

Here the influence of the step size on the accuracy of the results and the duration of the simulation will be investigated. The case here is that of 1 wt% ice, an exponential distribution and a vapor eruption velocity out of the vents of 450 m/s. The surface stress will be calculated every 50 iterations (see Section 5.3.2 for more information). The results can be found in Table B.1. Decreasing the step-size from $4.59{\cdot}10^6$ to $4.59{\cdot}10^5$ years does not significantly change the value of the final semi-major axis. In comparison there is still a significant change in the final mass of the H_2O-layer when changing the step-size between those values. Therefore the chosen step-size was set at $4.59{\cdot}10^4$ years. This was not tested as the duration would be too long which was confirmed when doing the actual simulations as they took more than 4 hours to run.

Table B.1: Influence of step-size

Number of steps	Step size [years]	Difference in final semi-major axis	Difference in final mass of H_2O layer	Duration [s]
10	4.59 E8	/	/	20
100	4.59 E7	1.71%	14.82%	145
1000	4.59 E6	0.11%	13.94%	755
10000	4.59 E5	0.01%	1.33%	2572

B.2 Selective Calculations

The most lengthy calculation by far is that of the surface stress as it took 75% of the required computational time for one iteration (see Appendix app:sensitivitysurfacestress for the test). Therefore the performance of the code can be enhanced greatly by only calculating the surface stress every few iterations and using previous values for the intermediate iterations. First one must be sure that it is acceptable to use this strategy. Therefore the influence of doing this on the results and on the performance is investigated. The results can be found in Table B.2. Note that the step-size was set at $4.56{\cdot}10^6$ years. The difference of the final semi-major axis and mass of the remaining H_2O-layer is with respect to the case where the surface stress is calculated in every iteration and given as a percentage. Table B.2 indicates that the performance of the code is increased significantly by only calculating the surface stress every few calculations. By calculating the surface stress every 50 iterations the computational time is divided by 4 while the difference in final semi-major axis and remaining mass of the H_2O-layer is not significant. Further decreasing the frequency of calculation has a diminishing return on the duration of the simulation while the accuracy is reduced even further. Because of this and the unknown effect of reducing the frequency of calculation

if the step-size is decreased even more the rate of calculation of the surface stress will be set at 1 in 50 iterations.

Table B.2: Influence of selective calculations

Frequency of calculating the surface stress	Final semi-major axis [m]	Difference in final mass of the H_2O layer [%]	Duration [s]
Every iteration	/	/	3042
1 in 5 iterations	$< 5{\cdot}10^{-4}$	0.13	1161
1 in 10 iterations	$< 1{\cdot}10^{-3}$	0.32	934
1 in 50 iterations	$< 7{\cdot}10^{-3}$	1.68	755
1 in 100 iterations	0.013	3.31	721
1 in 250 iterations	0.031	8.46	693

Appendix C

Sensitivity Tests

C.1 Convergence of Heat Flows

The equilibrium conditions requires the heat flow through the icy shell (as described in Chapter 2) to be equal to the surface heat flow due to tidal dissipation (as described in Chapter 3). They are deemed sufficiently close to each other if their difference is less than a certain convergence criterion. A sensitivity test was performed to determine the influence of this convergence criterion and the results of that test are shown in Table C.1. Again two cases were considered, one with a mass of the H_2O-layer of 10 wt% and one with 50 wt%. Both cases use a convergence criterion of 1% and have an initial estimate for the total thickness of the ice layer of 400m. The results show that a convergence criterion of 1% or less does not significantly alter the obtained ice shell thickness or heat flow through the stagnant lid. Using a convergence criterion of 10% yields similar results but with a slightly larger difference. Using a convergence criterion of 0.1% or less increased the computational time by a factor of 50 for some cases. Therefore using 1% as the convergence criterion was the best option considering accuracy and computational efficiency.

Table C.1: Sensitivity test on the convergence criterion between Q_{stag} and the tidal dissipation

Difference between	Equilibrium thickness		Stagnant heat flow	
consecutive calculations	for 10 wt% [m]	for 50 wt% [m]	for 10 wt% [W]	for 50 wt% [W]
$< 10\%$	200.00	198.00	1.34 E14	2.18 E14
$< 1\%$	198.00	194.06	1.36 E14	2.23 E14
$< 0.1\%$	198.23	193.65	1.35 E14	2.23 E14
$< 0.01\%$	198.19	193.61	1.35 E14	2.23 E14

C.2 Sensitivity Tests for the Root Finding Algorithm

The sensitivity of the initial estimate and the change in estimate of the ice shell thickness (denoted as $\Delta estimate$) in the case that no convergence is obtained is shown in Table C.2 for two cases, one with a mass of the H_2O-layer of 10 wt% and one with 50 wt%. Both cases use a convergence criterion of 1% and have an initial estimate for the total thickness of the ice layer of 400m. The results show that the influence of the initial estimate and the change in initial estimate do not influence the end result. Note that the results were rounded off to the nearest integer.

Table C.3 shows the sensitivity of the convergence criterion of the root finding algorithm. This algorithm repeatedly calculates the value of the root. A solution is found if the difference between the calculated values of two successive roots is deemed small enough, which is determined by the convergence criterion. The value of the convergence criterion has no impact on the final results. To save on computational time the criterion is set at 1%. Note that the results were rounded off to the nearest integer.

Table C.2: Sensitivity test on the initial estimate and the change in initial estimate

Initial estimate [m]	Δestimate [m]	Equilibrium thickness for 10 wt% [m]	Equilibrium thickness for 50 wt% [m]
1	1	198	194
	10	198	194
	100	198	194
10	1	198	194
	10	198	194
	100	198	194
100	1	198	194
	10	198	194
	100	198	194
1000	1	198	194
	10	198	194
	100	198	194

Table C.3: Sensitivity test on the convergence criterion

Difference between consecutive calculations	Equilibrium thickness for 10 wt% [m]	Equilibrium thickness for 50 wt% [m]
$< 10\%$	198	194
$< 1\%$	198	194
$< 0.1\%$	198	194
$< 0.01\%$	198	194

C.3 Sensitivity Tests for the Mantle Temperature

Table C.4 show the sensitivity of the mantle temperature to the initial estimate for the mantle temperature. Two cases were tested: one with a H_2O-layer with 10 wt% and one with 50 wt%. Both cases had an initial estimate for the icy shell thickness of 400 m. The results show no sensitivity to the initial mantle temperature estimate. The difference in mantle temperatures of the 10 wt% case can be attributed to the convergence criterion of 1% that was used in these tests. Note that the results have been rounded off to the nearest integer.

Table C.5 shows the results of the sensitivity test for the convergence criterion. Here convergence is reached when the heat flow out of the mantle is close enough to the heat flow in to the stagnant lid. The same two cases were considered as above with an initial estimate of the mantle temperature equal to the average solidus temperature of the mantle. The results show no increase in accuracy between a convergence criterion of 1% and of 0.01%. No convergence was found for a criterion of 0.01% and 50 wt% because the requirements were too strict. Because of this and to save on computational time the criterion was set at 1%.

C.4 Sensitivity Test for the Surface Stress

Table C.6 shows the sensitivity of the computational time on the locations at which the surface stress is calculated. For this test the values of the parameters of the maximum case were used with the present-day

Table C.4: Sensitivity test on the initial mantle temperature

Initial estimate for the temperature [K]	Mantle temperature for 10 wt% [K]	Mantle temperature for 50 wt% [K]
1500	1766	1842
1600	1766	1842
1700	1766	1842
1800	1767	1842
1900	1767	1842
2000	1767	1842
2100	1767	1842
2200	1767	1842

Table C.5: Sensitivity test for the convergence criterion

Difference between mantle and stagnant heat flow	Mantle temperature for 10 wt% [K]	Mantle temperature for 50 wt% [K]
$< 1\%$	1766	1842
$< 0.1\%$	1766	1842
$< 0.01\%$	1766	/

value of the semi-major axis. It clearly shows that increasing the number of latitude and longitude points beyond 7 does not increase the accuracy of the eruptive area but only requires more computational time. Therefore the value of 70 is used resulting in 4900 points where the surface stress is calculated.

Table C.6: Sensitivity of eruptive area and computational time on the number of points where the surface stress is calculated.

Number of points	Eruptive area [%]	Duration to calculate surface stress [s]	Total duration [s]
50	85.9	1	2.6
60	85.8	2.3	3.3
70	86.0	3	4
80	86.0	3.8	5
90	86.0	4.9	6
100	86.0	5.9	7

Appendix D

Unique Solution

Table D.1 shows the results of the test that was performed to check if the obtained equilibrium solution was unique. The total thickness of the icy shell was calculated for different H_2O-layers and for different initial estimates of the thickness. Note that some tests had an initial estimate that was higher than the thickness of the H_2O-layer. These cases are marked with /. The tests with 0.1, 1, 10, 25 and 50 wt% were performed early on with the present-day semi-major axis. Later on when the three simulated cases were chosen these tests were done again for the three cases but this time for the semi-major-axis at which they would start their simulation as those tests would be more realistic. How these initial semi-major axes are calculated can be found in Section 3.4.4 and their values are given in Table 5.1. For every case tested there was one unique solution. Note that the values presented here were rounded of to the nearest integer. Therefore the results may differ slightly as a convergence criterion was used to determine the solution giving a small range of possible values.

Table D.1: This table shows that the initial estimate for the thickness of the ice shell had no effect on the equilibrium ice shell thickness, the solution is unique. The test was done for different initial ice estimates and for different masses for the H_2O-layer.

	Ice shell thickness for an initial estimate D_{ice} of			
Initial wt%	50	500	5000	50000
0.1	237	235	/	/
1	232	232	232	/
10	199	198	198	198
25	182	183	183	182
50	194	194	194	194
0.65	11	11	11	/
2.5	7	7	7	7
11	9	9	9	9

Appendix E

Verification

E.1 Onset of convection

To validate the calculation of the Rayleigh number and the onset of convection the ice layer thickness of the icy shell at which convection would commence for different melting-point viscosities of ice was calculated. The results are similar to those of Hussmann et al. [2002] at lower values of the melting-point viscosity and differ slightly for larger values (see Table E.1) . This could be because of a different critical value. In this work a value of 1000 is used whereas Hussmann et al. [2002] indicate that it is on the order of 10^3 so it is not clear if they also use a value of 1000 or if it is slightly larger such as 1500 for example. If they used a slightly larger value that could explain why the thickness at which convection starts is slightly larger for them.

Table E.1: Comparison for the onset of convection

Melting-point viscosity [Pa·s]	Thickness at which convection occurs [km]	
	Hussmann et al. [2002]	This work
5E12	≈ 20	≈ 20
1E13	≈ 25	≈ 25
1E14	≈ 58	≈ 60
5E14	≈ 105	≈ 95

E.2 Escape Rate

The results from Equations A.33 and A.36 will be compared to results from Bierson and Steinbrügge [2021], where an escape velocity of 2000 m/s and eruption velocities of 90, 250 and 1000 m/s were used. The resulting fraction of erupted molecules that are lost can be found in Table E.2. It is clear that the obtained results are in agreement with those from Bierson and Steinbrügge [2021], indicating that Equations A.33 and A.36 are correct and can therefore be used when calculating the fraction of mass that is lost. The slight differences are due to the used definition of escape velocity or in other words the velocity at which the erupted particle is considered to have escaped. This work uses the standard definition that a particle at escape velocity will have an infinite semi-major axis [Wertz, 2001]. Bierson and Steinbrügge [2021] argues a particle only needs to reach Jupiter's Hill sphere (which is the sphere wherein Jupiter's gravitational pull is dominant) to be considered lost. Thus the required escape velocity will be lower which can be seen in Table E.2 through the slightly larger escape fractions obtained by Bierson and Steinbrügge [2021].

Eruption velocity	Exponential distribution		Lorentzian distribution	
v_0 [m/s]	This work	Bierson and Steinbrügge [2021]	This work	Bierson and Steinbrügge [2021]
90	2.23E-8%	< E-7%	2.86%	2%
250	0.03%	0.03%	7.91%	8%
1000	13.53%	14%	29.52%	30%

Table E.2: Fraction of erupted molecules that are lost, literature is Bierson and Steinbrügge [2021]

E.3 Tidal Dissipation

Two tests were done to verify that the calculated tidal dissipation is correct. The first test was done to compare with the results obtained by Hussmann et al. [2002] and the second test was done to compare with the results obtained by Beuthe [2013]. Both are described below.

Comparison with Hussmann et al. [2002]

Results obtained by using the method described in Section 3.3.1 have been compared to results obtained by using the complete propagator method and results obtained by Hussmann et al. [2002]. Figure E.1 shows the tidal dissipation of Europa for several different ice shell thicknesses. Figures E.2a and E.2b show the calculated tidal dissipation of the same Europa by using the weight functions and the matrix propagator method respectively.

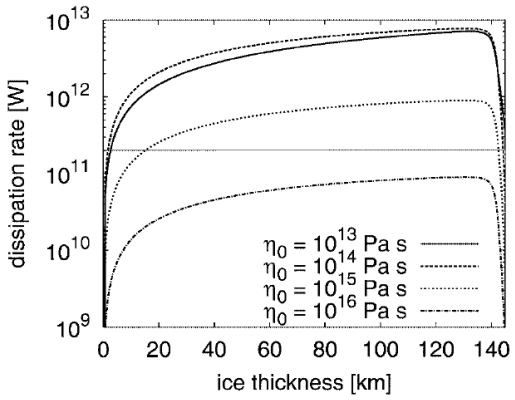

Figure E.1: Tidal dissipation within Europa [Hussmann et al., 2002]

The results obtained by either method are equal to each other but differ from those obtained by Hussmann et al. [2002]. One difference is the change in tidal dissipation when the H_2O-layer is completely frozen. While the calculated results show a very sharp drop in dissipation rate those of Hussmann et al. [2002] show a more gradual decrease. The second difference is the magnitude of the dissipation rates. For a melting-point viscosity of 10^{13}Pa·s Hussmann et al. [2002] obtains a higher tidal dissipation rate than the calculated value with a difference of about $4{\cdot}10^{1}$W for an ice shell of 140 km. For a melting-point viscosity of 10^{14}Pa·s and 10^{15}Pa·s Hussmann et al. [2002] obtains lower dissipation than the calculated results with the difference being about $5{\cdot}10^{12}$ W and $5{\cdot}10^{11}$ W respectively. For a melting-point viscosity of 10^{16}Pa·s the magnitude of dissipation the results were similar. It is unclear what the cause of these differences are. One reason could be in the way the authors model the ocean which could lead to a difference in how the icy shell is decoupled from the mantle. Unfortunately how this is done is not described by Hussmann et al. [2002].

Comparison with Beuthe [2013]

Beuthe [2013] calculated the tidal dissipation and values for the Love number of Io. With his model Beuthe [2013] obtained an absolute value of the tidal potential Love number of 0.24 and the model used

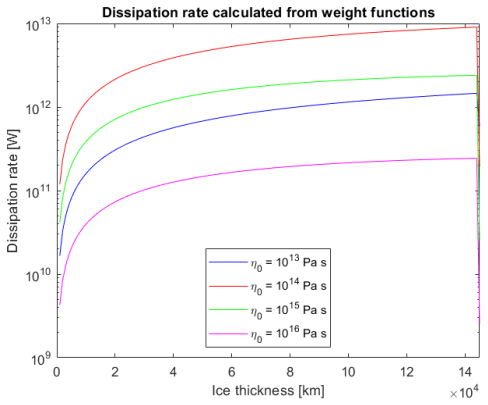

(a) Tidal dissipation of Europa using weight functions

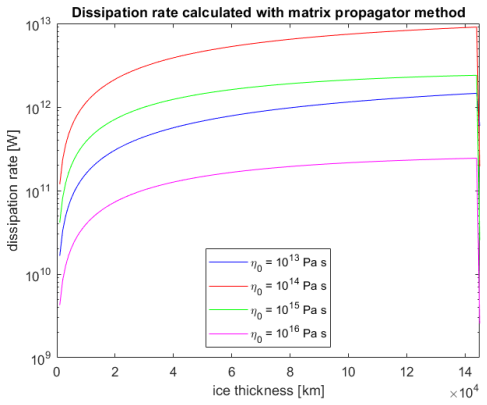

(b) Tidal dissipation of Europa using propagator matrix method

Figure E.2: Dissipation rate of Europa for different ice shell thicknesses. Figure E.2a shows the results by using the weight functions and Figure E.2b shows the results by using the complete matrix propagation method. Note that these two methods give the same result but that is different to the result of Hussmann et al. [2002] given in Figure E.1. A discussion about these differences can be found in the text.

for this work obtained the exact same value. As for the tidal dissipation Beuthe [2013] obtained a value of $9\pm2\cdot10^{13}$ W and the model for this work determined a value of $9.3\cdot10^{13}$ W. The difference between the dissipation could be due to the fact that Beuthe [2013] included a separate asthenosphere in the interior structure of Io whereas this model does not. Instead it uses a parameterized mantle viscosity and shear modulus to mimic the effect of the partially molten asthenosphere. As the obtained value lies within the range given by Beuthe [2013] one can conclude that the model is able to calculate the tidal dissipation within Io with sufficient accuracy.

Comparison with Steinke et al. [2020]

Steinke et al. [2020] calculated the tidal dissipation within Io for two different model. The difference between these models lies in the location of the tidal dissipation. In their model A dissipation was limited to the asthenosphere only and in their model B 60% of the heat was dissipated in the mantle and 40% in the asthenosphere. The total tidal dissipation for both of these models can be seen in Table E.3. The model created in this thesis also calculated the tidal dissipation for both model A and B of Steinke et al. [2020]. The results of these calculation can also be seen in Table E.3. The difference between the two results is about 3.8 and 2.5% for models A and B respectively. The difference could be due to the fact that Steinke et al. [2020] used the matrix propagation method by Jara-Orué and Vermeersen [2011] and Sabadini et al. [2016] while the model in this work uses a combination of that matrix propagation method and the method by Beuthe [2013]. As the difference is small enough it can again be concluded that the model created in this work is able to determine the tidal dissipation within Io with sufficient accuracy.

Table E.3: Total heat dissipation of models A and B for Io by Steinke et al. [2020]. Comparison between their results and the results calculated by the model created in this work.

	Results from Steinke et al. [2020]		Results from this work	
	Model A	Model B	Model A	Model B
Total tidal dissipation [W]	$9.02\cdot10^{13}$W	$9.07\cdot10^{13}$W	$9.36\cdot10^{13}$W	$9.30\cdot10^{13}$W

Bibliography

Amy C Barr and Robert T Pappalardo. Onset of convection in the icy galilean satellites: Influence of rheology. *Journal of Geophysical Research: Planets*, 110(E12), 2005.

Mikael Beuthe. Spatial patterns of tidal heating. *Icarus*, 223(1):308–329, 2013.

Mikael Beuthe. Enceladus's crust as a non-uniform thin shell: I tidal deformations. *Icarus*, 302:145–174, 2018.

Mikael Beuthe, Attilio Rivoldini, and Antony Trinh. Enceladus's and dione's floating ice shells supported by minimum stress isostasy. *Geophysical Research Letters*, 43(19):10–088, 2016.

Carver J Bierson and Francis Nimmo. Explaining the galilean satellites' density gradient by hydrodynamic escape. *The Astrophysical Journal Letters*, 897(2):L43, 2020.

Carver J Bierson and Gregor Steinbrügge. Tidal heating did not dry out io and europa. *The Planetary Science Journal*, 2(3):89, 2021.

Michael T Bland, Adam P Showman, and Gabriel Tobie. The orbital–thermal evolution and global expansion of ganymede. *Icarus*, 200(1):207–221, 2009.

Nikolai V Brilliantov, Jürgen Schmidt, and Frank Spahn. Geysers of enceladus: Quantitative analysis of qualitative models. *Planetary and Space Science*, 56(12):1596–1606, 2008.

MH Burger, EC Sittler Jr, RE Johnson, HT Smith, OJ Tucker, and VI Shematovich. Understanding the escape of water from enceladus. *Journal of Geophysical Research: Space Physics*, 112(A6), 2007.

Robin M Canup and William R Ward. Formation of the galilean satellites: Conditions of accretion. *The Astronomical Journal*, 124(6):3404, 2002.

Robin M Canup and William R Ward. Origin of europa and the galilean satellites. *Europa*, pages 59–83, 2009.

Katherine de Kleer, Alfred S McEwen, Ryan S Park, Carver J Bierson, Ashley G Davies, Daniella N DellaGustina, Anton I Ermakov, Jim Fuller, Christopher W Hamilton, Camilla DK Harris, et al. Tidal heating: Lessons from io and the jovian system-final report. 2019.

Imke De Pater and Jack J Lissauer. *Planetary sciences*. Cambridge University Press, 2015.

Y Dong, TW Hill, BD Teolis, BA Magee, and JH Waite. The water vapor plumes of enceladus. *Journal of Geophysical Research: Space Physics*, 116(A10), 2011.

CA Dwyer, F Nimmo, M Ogihara, and S Ida. The influence of imperfect accretion and radial mixing on ice: rock ratios in the galilean satellites. *Icarus*, 225(1):390–402, 2013.

H-J Fischer and T Spohn. Thermal-orbital histories of viscoelastic models of io (j1). *Icarus*, 83(1):39–65, 1990.

Jim Fuller, Jing Luan, and Eliot Quataert. Resonance locking as the source of rapid tidal migration in the jupiter and saturn moon systems. *Monthly Notices of the Royal Astronomical Society*, 458(4):3867–3879, 2016.

SV Gavrilov and VN Zharkov. Love numbers of the giant planets. *Icarus*, 32(4):443–449, 1977.

O Grasset and EM Parmentier. Thermal convection in a volumetrically heated, infinite prandtl number fluid with strongly temperature-dependent viscosity: Implications for planetary thermal evolution. *Journal of Geophysical Research: Solid Earth*, 103(B8):18171–18181, 1998.

Candice J Hansen, L Esposito, AIF Stewart, J Colwell, A Hendrix, W Pryor, D Shemansky, and R West. Enceladus' water vapor plume. *Science*, 311(5766):1422–1425, 2006.

CJ Hansen, LW Esposito, AIF Stewart, B Meinke, B Wallis, JE Colwell, AR Hendrix, K Larsen, W Pryor, and F Tian. Water vapour jets inside the plume of gas leaving enceladus. *Nature*, 456(7221):477–479, 2008.

CJ Hansen, Donald E Shemansky, Larry W Esposito, AIF Stewart, BR Lewis, JE Colwell, AR Hendrix, Robert A West, JH Waite Jr, B Teolis, et al. The composition and structure of the enceladus plume. *Geophysical Research Letters*, 38(11), 2011.

MM Hedman, PD Nicholson, MR Showalter, RH Brown, BJ Buratti, and RN Clark. Spectral observations of the enceladus plume with cassini-vims. *The Astrophysical Journal*, 693(2):1749, 2009.

MM Hedman, CM Gosmeyer, PD Nicholson, C Sotin, Robert H Brown, RN Clark, KH Baines, BJ Buratti, and MR Showalter. An observed correlation between plume activity and tidal stresses on enceladus. *Nature*, 500(7461):182–184, 2013.

Douglas J Hemingway, Maxwell L Rudolph, and Michael Manga. Cascading parallel fractures on enceladus. *Nature Astronomy*, 4(3):234–239, 2020.

TA Hurford, P Helfenstein, GV Hoppa, R Greenberg, and BG Bills. Eruptions arising from tidally controlled periodic openings of rifts on enceladus. *Nature*, 447(7142):292–294, 2007.

Hauke Hussmann and Tilman Spohn. Thermal-orbital evolution of io and europa. *Icarus*, 171(2):391–410, 2004.

Hauke Hussmann, Tilman Spohn, and Karin Wieczerkowski. Thermal equilibrium states of europa's ice shell: Implications for internal ocean thickness and surface heat flow. *Icarus*, 156(1):143–151, 2002.

Hauke Hussmann, Gaël Choblet, Valéry Lainey, Dennis L Matson, Christophe Sotin, Gabriel Tobie, and Tim Van Hoolst. Implications of rotation, orbital states, energy sources, and heat transport for internal processes in icy satellites. *Space science reviews*, 153(1):317–348, 2010.

Andrew P Ingersoll and Shawn P Ewald. Total particulate mass in enceladus plumes and mass of saturn's e ring inferred from cassini iss images. *Icarus*, 216(2):492–506, 2011.

Hermes M Jara-Orué and Bert LA Vermeersen. Effects of low-viscous layers and a non-zero obliquity on surface stresses induced by diurnal tides and non-synchronous rotation: The case of europa. *Icarus*, 215 (1):417–438, 2011.

Randolph L Kirk and David J Stevenson. Thermal evolution of a differentiated ganymede and implications for surface features. *Icarus*, 69(1):91–134, 1987.

Valéry Lainey, Jean-Eudes Arlot, Özgür Karatekin, and Tim Van Hoolst. Strong tidal dissipation in io and jupiter from astrometric observations. *Nature*, 459(7249):957–959, 2009.

Jonathan I Lunine. Origin of water ice in the solar system. *Meteorites and the early solar system II*, pages 309–319, 2006.

M Manga and C-Y Wang. Pressurized oceans and the eruption of liquid water on europa and enceladus. *Geophysical Research Letters*, 34(7), 2007.

William B McKinnon and Randolph L Kirk. Triton. In *Encyclopedia of the Solar System*, pages 861–881. Elsevier, 2014.

WB Moore. Tidal heating and convection in io. *Journal of Geophysical Research: Planets*, 108(E8), 2003.

Ignacio Mosqueira and Paul R Estrada. Formation of the regular satellites of giant planets in an extended gaseous nebula i: subnebula model and accretion of satellites. *Icarus*, 163(1):198–231, 2003.

Carl D Murray and Stanley F Dermott. *Solar system dynamics*. Cambridge university press, 1999.

Miki Nakajima and Andrew P Ingersoll. Controlled boiling on enceladus. 1. model of the vapor-driven jets. *Icarus*, 272:309–318, 2016.

F Nimmo and DG Korycansky. Impact-driven ice loss in outer solar system satellites: Consequences for the late heavy bombardment. *Icarus*, 219(1):508–510, 2012.

Francis Nimmo and Carolyn Porco. Enceladus. In *Encyclopedia of the Solar System*, pages 851–859. Elsevier, 2014.

Francis Nimmo, Carolyn Porco, and Colin Mitchell. Tidally modulated eruptions on enceladus: Cassini iss observations and models. *The Astronomical Journal*, 148(3):46, 2014.

Gordon I Ogilvie and DNC Lin. Tidal dissipation in rotating giant planets. *The Astrophysical Journal*, 610(1):477, 2004.

Lucas Paganini, Geronimo L Villanueva, Lorenz Roth, AM Mandell, TA Hurford, Kurt D Retherford, and Michael J Mumma. A measurement of water vapour amid a largely quiescent environment on europa. *Nature astronomy*, 4(3):266–272, 2020.

D Alex Patthoff, Simon A Kattenhorn, and CM Cooper. Implications of nonsynchronous rotation on the deformational history and ice shell properties in the south polar terrain of enceladus. *Icarus*, 321: 445–457, 2019.

SJ Peale and RM Canup. The origin of the natural satellites. *Treatise on Geophysics: Second Edition*, 10: 559–604, 2015.

SJ Peale and Man Hoi Lee. A primordial origin of the laplace relation among the galilean satellites. *Science*, 298(5593):593–597, 2002.

WR Peltier. The impulse response of a maxwell earth. *Reviews of Geophysics*, 12(4):649–669, 1974.

Carolyn Porco, Daiana DiNino, and Francis Nimmo. How the geysers, tidal stresses, and thermal emission across the south polar terrain of enceladus are related. *The Astronomical Journal*, 148(3):45, 2014.

Carolyn C Porco, Paul Helfenstein, PC Thomas, AP Ingersoll, J Wisdom, Robert West, Gerhard Neukum, Tilmann Denk, Roland Wagner, Thomas Roatsch, et al. Cassini observes the active south pole of enceladus. *science*, 311(5766):1393–1401, 2006.

Alyssa Rose Rhoden, Terry A Hurford, Joseph Spitale, Wade Henning, Eric M Huff, Michael T Bland, and Stan Sajous. The formation of enceladus' tiger stripe fractures from eccentricity tides. *Earth and Planetary Science Letters*, 544:116389, 2020.

Thomas Ronnet, Olivier Mousis, and Pierre Vernazza. Pebble accretion at the origin of water in europa. *The Astrophysical Journal*, 845(2):92, 2017.

Lorenz Roth, Joachim Saur, Kurt D Retherford, Darrell F Strobel, Paul D Feldman, Melissa A McGrath, and Francis Nimmo. Transient water vapor at europa's south pole. *science*, 343(6167):171–174, 2014.

Marc Rovira-Navarro, Wouter Van der Wal, Teresa Steinke, and Dominic Dirkx. Tidally heated exomoons around gas giants. *The Planetary Science Journal*, 2(3):119, 2021.

Roberto Sabadini, Bert Vermeersen, and Gabriele Cambiotti. *Global dynamics of the Earth*. Springer, 2016.

Jürgen Schmidt, Nikolai Brilliantov, Frank Spahn, and Sascha Kempf. Slow dust in enceladus' plume from condensation and wall collisions in tiger stripe fractures. *Nature*, 451(7179):685–688, 2008.

G Schubert, JD Anderson, T Spohn, and WB McKinnon. Interior composition, structure and dynamics of the galilean satellites. *Jupiter: The planet, satellites and magnetosphere*, 1:281–306, 2004.

Gerald Schubert, John D Anderson, Bryan J Travis, and Jennifer Palguta. Enceladus: Present internal structure and differentiation by early and long-term radiogenic heating. *Icarus*, 188(2):345–355, 2007.

M Segatz, T Spohn, MN Ross, and G Schubert. Tidal dissipation, surface heat flow, and figure of viscoelastic models of io. *Icarus*, 75(2):187–206, 1988.

Daigo Shoji and Kei Kurita. Thermal-orbital coupled tidal heating and habitability of martian-sized extrasolar planets around m stars. *The Astrophysical Journal*, 789(1):3, 2014.

HT Smith, RE Johnson, ME Perry, DG Mitchell, RL McNutt, and DT Young. Enceladus plume variability and the neutral gas densities in saturn's magnetosphere. *Journal of Geophysical Research: Space Physics*, 115(A10), 2010.

Laurence A Soderblom, SW Kieffer, TL Becker, Robert H Brown, AF Cook, CJ Hansen, TV Johnson, Randolph L Kirk, and EM Shoemaker. Triton's geyser-like plumes: Discovery and basic characterization. *Science*, 250(4979):410–415, 1990.

F Sohl, T Spohn, D Breuer, and K Nagel. Implications from galileo observations on the interior structure and chemistry of the galilean satellites. *Icarus*, 157(1):104–119, 2002.

John R Spencer and Francis Nimmo. Enceladus: An active ice world in the saturn system. *Annual Review of Earth and Planetary Sciences*, 41:693–717, 2013.

John R Spencer, Amy C Barr, Larry W Esposito, Paul Helfenstein, Andrew P Ingersoll, Ralf Jaumann, Christopher P McKay, Francis Nimmo, and J Hunter Waite. Enceladus: An active cryovolcanic satellite. In *Saturn from Cassini-Huygens*, pages 683–724. Springer, 2009.

JR Spencer, JC Pearl, M Segura, FM Flasar, A Mamoutkine, P Romani, BJ Buratti, AR Hendrix, LJ Spilker, and RMC Lopes. Cassini encounters enceladus: Background and the discovery of a south polar hot spot. *science*, 311(5766):1401–1405, 2006.

Joseph N Spitale and Carolyn C Porco. Association of the jets of enceladus with the warmest regions on its south-polar fractures. *Nature*, 449(7163):695–697, 2007.

Tilman Spohn and Gerald Schubert. Oceans in the icy galilean satellites of jupiter? *Icarus*, 161(2): 456–467, 2003.

T Steinke, H Hu, D Höning, W Van der Wal, and B Vermeersen. Tidally induced lateral variations of io's interior. *Icarus*, 335:113299, 2020.

Eiichi Takahashi. Speculations on the archean mantle: missing link between komatiite and depleted garnet peridotite. *Journal of Geophysical Research: Solid Earth*, 95(B10):15941–15954, 1990.

H Takeuchi and M Saito. Seismic surface waves. *Methods in computational physics*, 11:217–295, 1972.

V Tenishev, MR Combi, BD Teolis, and JH Waite. An approach to numerical simulation of the gas distribution in the atmosphere of enceladus. *Journal of Geophysical Research: Space Physics*, 115(A9), 2010.

BD Teolis, ME Perry, BA Magee, J Westlake, and JH Waite. Detection and measurement of ice grains and gas distribution in the enceladus plume by cassini's ion neutral mass spectrometer. *Journal of Geophysical Research: Space Physics*, 115(A9), 2010.

PC Thomas, R Tajeddine, MS Tiscareno, JA Burns, J Joseph, TJ Loredo, P Helfenstein, and C Porco. Enceladus's measured physical libration requires a global subsurface ocean. *Icarus*, 264:37–47, 2016.

Feng Tian, AIF Stewart, Owen B Toon, Kristopher W Larsen, and Larry W Esposito. Monte carlo simulations of the water vapor plumes on enceladus. *Icarus*, 188(1):154–161, 2007.

G Tobie, A Mocquet, and C Sotin. Tidal dissipation within large icy satellites: Applications to europa and titan. *Icarus*, 177(2):534–549, 2005.

Gabriel Tobie, Gaël Choblet, and Christophe Sotin. Tidally heated convection: Constraints on europa's ice shell thickness. *Journal of Geophysical Research: Planets*, 108(E11), 2003.

J Hunter Waite, Michael R Combi, Wing-Huen Ip, Thomas E Cravens, Ralph L McNutt, Wayne Kasprzak, Roger Yelle, Janet Luhmann, Hasso Niemann, David Gell, et al. Cassini ion and neutral mass spectrometer: Enceladus plume composition and structure. *science*, 311(5766):1419–1422, 2006.

J.R. Wertz. *Mission Geometry; Orbit and Constellation Design and Management*. Springer Dordrecht, 2001.

Jody K Wilson, Michael Mendillo, Jeffrey Baumgardner, Nicholas M Schneider, John T Trauger, and Brian Flynn. The dual sources of io's sodium clouds. *Icarus*, 157(2):476–489, 2002.

Yanqin Wu. Origin of tidal dissipation in jupiter. ii. the value of q. *The Astrophysical Journal*, 635(1):688, 2005.

Seng Keat Yeoh, Todd A Chapman, David B Goldstein, Philip L Varghese, and Laurence M Trafton. On understanding the physics of the enceladus south polar plume via numerical simulation. *Icarus*, 253: 205–222, 2015.

An Yin, Andrew V Zuza, and Robert T Pappalardo. Mechanics of evenly spaced strike-slip faults and its implications for the formation of tiger-stripe fractures on saturn's moon enceladus. *Icarus*, 266:204–216, 2016.

Charles F Yoder and Stanton J Peale. The tides of io. *Icarus*, 47(1):1–35, 1981.